EFFECT OF ELECTRODEPOSITED Cu-Ni LAYER ON INTERFACIAL REACTION AND MECHANICAL PROPERTIES OF LASER WELDED-BRAZED Mg/Ti JOINTS

AUWAL SHAMSU TUKUR

FACULTY OF ENGINEERING
UNIVERSITY OF MALAYA
KUALA LUMPUR

2019

EFFECT OF ELECTRODEPOSITED Cu-Ni LAYER ON INTERFACIAL REACTION AND MECHANICAL PROPERTIES OF LASER WELDED-BRAZED Mg/Ti JOINTS

AUWAL SHAMSU TUKUR

THESIS SUBMITTED IN FULFILMENT OF THE REQUIREMENTS FOR THE DEGREE OF DOCTOR OF PHILOSOPHY

FACULTY OF ENGINEERING
UNIVERSITY OF MALAYA
KUALA LUMPUR

2019

UNIVERSITY OF MALAYA

ORIGINAL LITERARY WORK DECLARATION

Name of Candidate: **Auwal Shamsu Tukur**

Matric No: **KHA160069**

Name of Degree: **Doctor of Philosophy**

Title of Project Paper/Research Report/Dissertation/Thesis ("this Work"):

Effect of Electrodeposited Cu-Ni layer on Interfacial Reaction and Mechanical Properties of Laser Welded-Brazed Mg/Ti Joints.

Field of Study: **Manufacturing Processes**

I do solemnly and sincerely declare that:

(1) I am the sole author/writer of this Work;

(2) This Work is original;

(3) Any use of any work in which copyright exists was done by way of fair dealing and for permitted purposes and any excerpt or extract from, or reference to or reproduction of any copyright work has been disclosed expressly and sufficiently and the title of the Work and its authorship have been acknowledged in this Work;

(4) I do not have any actual knowledge nor do I ought reasonably to know that the making of this work constitutes an infringement of any copyright work;

(5) I hereby assign all and every rights in the copyright to this Work to the University of Malaya ("UM"), who henceforth shall be owner of the copyright in this Work and that any reproduction or use in any form or by any means whatsoever is prohibited without the written consent of UM having been first had and obtained;

(6) I am fully aware that if in the course of making this Work I have infringed any copyright whether intentionally or otherwise, I may be subject to legal action or any other action as may be determined by UM.

Candidate's Signature   Date:

Subscribed and solemnly declared before,

Witness's Signature   Date:

Name:

Designation:

EFFECT OF ELECTRODEPOSITED Cu-Ni LAYER ON INTERFACIAL REACTION AND MECHANICAL PROPERTIES OF LASER WELDED-BRAZED Mg/Ti JOINTS

ABSTRACT

The ability to join Mg alloys to Ti effectively has received great interest in the manufacturing sector, especially in automotive and aerospace industries where light-weight components are crucial in order to exploit the advantages of both materials, reduce fuel consumption, greenhouse gases and improve performance of energy converting system. However, the significant differences in their physical and metallurgical properties make joining them together very difficult. Hence, selecting an appropriate welding technique and interlayer elements to produce and control interfacial layers became the focus of Mg/Ti joining. Based on the existing literature, controlling the heat input of welding parameter and the content of the interlayer elements were effective ways to regulate the interfacial reaction. In this work, 1.5 mm thick AZ31 Mg alloy was joined to 1 mm thick Ti-6Al-4V Ti alloy by laser welding-brazing process, using electrodeposited Cu-Ni layer under different welding schedules. Optical microscopy and scan electron microscopy (SEM) equipped with energy dispersive spectroscopy (EDS) were used to study the cross sectional microstructure morphologies and fracture surfaces. The reaction products formed was verified by X-ray diffraction (XRD) analysis. A test load of 100 g and 10 s dwell time were used to measure the Vickers hardness of the joints across the joint interface. In addition, room temperature tensile-shear test was performed on the 10 mm wide specimens machined from the joints with a cross head speed of 1 mm/min. Firstly, a fiber laser welding-brazing procedure has been developed for joining AZ31/Ti-6Al-4V via electrodeposited Cu-Ni interlayer. The effect of the interlayer arrangements (AZ31/Ni-Cu/Ti-6Al-4V and AZ31/Cu-Ni/Ti-6Al-4V) on appearance, interfacial reaction and mechanical properties were investigated at different heat input. The results

showed that the feasibility of the process significantly depend on the pre-existing Cu-Ni layer on the Ti surface that facilitates wetting of AZ92 brazing alloy. Depending on the interlayer arrangements chosen, different reactions layers formed inside the joint region. Nevertheless, at optimum heat input Ti_2Ni mingled with Ti_3Al interfacial reaction products was produced along the fusion zone (FZ)-Ti brazed interface in both interlayer arrangements, which grew evidently with increase in heat input. The average joint efficiency of 71% compared to AZ31B alloy was achieved. Under suitable heat input, the joints failed at the fusion zone of the AZ31B base metal, whereas, incomplete brazing or large volume of intermetallics at the brazed interface resulted in interfacial failure at lower/higher heat input. Secondly, the effect of the Cu and Ni contents on microstructure development and joint fracture load was analyzed. The results showed that the joining mechanism between the Mg alloy and the Ti was facilitated by the formation of a Ti_2Ni and Ti_3Al mixed interfacial reaction layer formed along the fusion zone-Ti brazed interface. However, the actual interfacial products were influenced by the welding method and interlayer elements content. At optimum Cu and Ni contents, the thickness of this mixed interfacial reaction layer was less than the critical thickness of 10 μm. The maximum tensile-shear fracture load attained 2020 N, which was about 100% higher than that of the uncoated joint. Finally, the relationships between interface characteristics, joint formation mechanism and mechanical properties of Mg/Ti joint with and without Cu, Ni and Cu-Ni coatings have been investigated and the Cu-Ni coated joint presented superior mechanical performance.

Keywords: Mg alloy, Ti alloy, intermetallic compounds (IMCs), microstructure, laser welding-brazing.

KESAN LAPISAN Cu-Ni ELEKTRODEPOSIT TERHADAP REAKSI INTERFACIAL DAN SIFAT MEKANIK SAMBUNGAN Mg/Ti MENGGUNAKAN KIMPALAN-PEMATRIAN LASER

ABSTRAK

Keupayaan untuk menyambung aloi Mg kepada Ti secara berkesan telah menarik minat yang besar dalam sektor pembuatan, terutamanya dalam industri automotif dan aeroangkasa di mana komponen berat ringan adalah penting untuk mengeksploitasi kelebihan kedua-dua bahan, mengurangkan penggunaan bahan api, gas rumah hijau dan meningkatkan prestasi sistem penukaran tenaga. Walau bagaimanapun, perbezaan ketara dalam sifat fizikal dan metalurgi mereka menjadikan penyambungan mereka sangat sukar. Oleh itu, memilih teknik kimpalan yang sesuai dan unsur-unsur interlayer untuk menghasilkan dan mengawal lapisan interfacial menjadi fokus penyambunganMg / Ti. Berdasarkan kajian yang sedia ada, mengawal input haba pada parameter kimpalan dan kandungan elemen interlayer adalah cara yang berkesan untuk mengawal tindak balas antara muka. Dalam kerja ini, aloi AZ31B Mg berketebalan 1.5 mm telah disambungkan kepada aloi Ti-6Al-4V Ti dengan ketebalan 1 mm melalui proses kimpalan laser, menggunakan lapisan Cu-Ni elektrodeposited di bawah jadual kimpalan yang berlainan. Mikroskopi optikal dan mikroskopi imbasan (SEM) yang dilengkapi dengan spektroskopi penyebaran tenaga (EDS) digunakan untuk mengkaji struktur morfologi keratan rentas dan permukaan retakan. Produk reaksi yang terbentuk disahkan oleh analisis difraksi sinar-X (XRD). Beban ujian 100 g dan masa tinggal 10 s digunakan untuk mengukur kekerasan Vickers sambungan merentasi antara muka bersama. Di samping itu, ujian suhu tegangan ricih bilik dilakukan pada spesimen dengan kelebaran 10 mm yang dimesin dari sendi dengan kelajuan kepala silang 1 mm / min. Pertama, prosedur gentian kimpalan laser serat telah dibangunkan untuk menyertai AZ31B hingga lembaran Ti-6Al-4V bersalut Cu-Ni menggunakan dawai pengisi aloi AZ92D Mg. Kesan susunan interaksi

(AZ31B / Ni-Cu / Ti-6Al-4V dan AZ31B / Cu-Ni / Ti-6Al-4V) pada penampilan, tindak balas antara muka dan sifat mekanik disiasat pada input haba yang berbeza. Keputusan menunjukkan bahawa kebolehsanaan proses itu bergantung kepada lapisan Cu-Ni yang sedia ada pada permukaan Ti yang memudahkan pembasahan aloi pengisi AZ92. Bergantung pada pengaturan interlayer yang dipilih, lapisan tindakbalas berlainan telah terbentuk di dalam kawasan sambungan. Walau bagaimanapun, pada input haba optimum Ti_2Ni bercampur dengan produk tindak balas interfacial Ti_3Al dihasilkan di sepanjang zon cantuman (FZ) -Ti antara muka pematrian dalam kedua-dua aturan interlayer, yang semakin meningkat dengan peningkatan input haba. Nilai purata kecekapan sambungan 71% berbanding aloi AZ31B dicapai. Di bawah input haba yang sesuai, sendi-sendi tersebut gagal di zon sambungan logam asas AZ31B, sedangkan pateri tidak lengkap atau jumlah intermetallik yang tidak lengkap pada antara muka pematrian mengakibatkan kegagalan interfacial pada input haba yang lebih rendah / lebih tinggi. Kedua, kesan daripada pengaruh kandungan Cu dan Ni terhadap pembangunan mikrostruktur dan beban patah sambungan dianalisis. Keputusan menunjukkan bahawa mekanisme penyambungan antara aloi Mg dan Ti dipermudahkan oleh pembentukan lapisan tindak balas interfacial campuran Ti_2Ni dan Ti_3Al yang terbentuk di sepanjang zon gabungan pematrian Ti antara muka. Walau bagaimanapun, produk antara dua muka dipengaruhi oleh kaedah kimpalan dan kandungan elemen interlayer. Pada kandungan Cu dan Ni optimum, ketebalan lapisan tindak balas interfacial campuran ini adalah kurang daripada ketebalan kritikal 10 μm. Beban retak maksimum ricih-ricih mencapai 2020 N, iaitu kira-kira 100% lebih tinggi daripada sambungan yang tidak bersalut. Akhirnya, hubungan antara ciri-ciri antara muka, mekanisme pembentukan sambungan dan sifat-sifat mekanik lekapan Mg / Ti yang dikimpal oleh laser dengan dan tanpa lapisan Cu, Ni dan Cu-Ni telah disiasat dan sambungan bersalut Cu-Ni menunjukkan prestasi mekanikal yang unggul.

Kata kunci: Aloi Mg, Aloi Ti, kompaun intermetallik (IMCs), mikrostruktur, laser kimpalan-pateri

ACKNOWLEDGEMENTS

Auwal Shamsu Tukur

TABLE OF CONTENTS

LIST OF FIGURES

LIST OF TABLES

LIST OF SYMBOLS AND ABBREVIATIONS

˚C : Degrees Celsius

μm : Micrometer

ASM : American Society of Metals

ASTM : American Society of Testing and Materials

AWS : American Welding Society

BM : Base Metal

cm : Centimeter

EDS : Energy Dispersive Spectroscopy

FEM : Finite Element Method

FESEM : Field Emission Scanning Electron Microscope

FZ : Fusion Zone

g : Gram

HAZ : Heat Affected Zone

HV : Vickers' Hardness Number

IMC : Intermetallic Compound

Kg : Kilogram

kN : Kilo Newton

LWB : Laser Welding Brazing

m : Meter

min : Minute

mm : Millimeter

mm : Millimeter

MPa : Megapascal

N : Newton

Pa	:	Pascal
s	:	Second
SAED	:	Selected Area Electron Diffraction
SEM	:	Scanning Electron Microscope
TEM	:	Transmission Electron Microscopy
TS	:	Tensile Shear
XRD	:	X-Ray Diffraction

CHAPTER 1: INTRODUCTION

1.1   Background

Magnesium (Mg) has been described as a green engineering material and one of the most promising material in the 21st century (Liu, 2010). It has unique properties such as high specific strength, good recyclability and formability (Cao *et al.*, 2006; Kulekci, 2008). Because of these properties, Mg alloys are being used to replace not only heavy alloys such as steels, but also light alloys, including aluminum alloys for a wide range of applications (Blawert *et al.*, 2004; Kumar *et al.*, 2015b; Manladan *et al.*, 2016). In recent years, the weight reduction for fuel economy in transport industry has spurred the growth of Mg consumption at an annual rate of 15% (Luo, 2002). However, despite their excellent mechanical properties, Mg alloys remain susceptible to corrosion (Yue *et al.*, 2010). In contrast, titanium (Ti) and its alloys have been used extensively in aerospace, medical, chemical, petrochemical and aviation industries for their high creep resistance, excellent corrosion resistance, biocompatibility and high strength to weight ratio (Brunette *et al.*, 2012; Fujii *et al.*, 2003). Nevertheless, Ti is more expensive than most commonly used metals because of its costly manufacturing process (Lütjering & Williams, 2007).

Hybrid structures built using light-weight materials such as Mg/Ti are expected to play an important role in the high-technology based industries such as aerospace and automotive where light-weight components are essential in order to enhance the efficiency of energy converting systems; minimize fuel consumption and emission of greenhouse gases (Baqer *et al.*, 2018; Manabe, 1999; Schubert *et al.*, 2001). The typical practical application of the Mg/Ti hybrid structures could be found in seat track of wide bodied aircrafts and wind of airplane, where the Ti crust welded to Mg honeycomb. Therefore, it is crucial to develop new methods to produce reliable Mg/Ti joints. In particular, AZ31B and Ti-6Al-4V are commonly used Mg and Ti alloys, respectively

(Mordike & Ebert, 2001; Williams & Belov, 1982). The development of efficient welding techniques for AZ31B and Ti-6Al-4V would be required to expand their applications particularly in the transportation industry.

However, joining Mg directly to Ti by traditional welding techniques is challenging owing to the huge discrepancies in their physical properties (e.g. melting point, coefficient of thermal expansion, thermal conductivity) and metallurgical characteristics (near zero solubility) of Mg and Ti (Aonuma & Nakata, 2009). Therefore, an alternative welding method that overcome the difficulties is very much desired.

As an advanced joining technology, laser welding-brazing (LWB) has gained considerable attention in the past 40 years for industrial production due to its high flexibility, adaptability, excellent joining qualities coupled with low thermal impact compared with other welding processes (Otto & Schmidt, 2010). Therefore, LWB technique is suitable for joining dissimilar materials having large difference in melting point such as Mg/Ti and Mg/steel (Li *et al.*, 2013; Tan *et al.*, 2016a). In LWB, the high power laser melts the filler and the Mg base metal concurrently, while the Ti remains un-melted. In addition, a thin interlayer which could interact with or have significant solubility in both materials is used to achieve Mg/Ti interfacial reaction. LWB method have been used with limited success when applied to join Mg/Ti using AZ91 Mg based filler in earlier work (Tan *et al.*, 2016a), the Al from the brazing alloy performed an indispensable role in the joint formation. However, the content of the Al was not easy to control because of the limited Al content added in the Mg filler. Therefore, addition of suitable interlayer material is still required. Copper and nickel can react with Mg and Ti in accordance with their binary diagrams, hence metallurgical bonding between AZ31B and Ti-6Al-4V alloys may be achieved, which may contribute to the enhancement of the joint performance. In addition, copper and nickel have complete liquid and solid solubility

(isomorphous system), which could led to homogeneous microstructure with excellent corrosion resistance (Yue *et al.*, 2010).

Based on these considerations, the application of LWB technique to lap join the AZ31/Ti-6Al-4V by means of electrodeposited Cu-Ni was explored in the current study. The interfacial reaction, element distribution and mechanical properties were examined to clarify the role of the Cu-Ni layer on Mg/Ti metallurgical bonding. Furthermore, numerical analysis of the temperature field was performed to help in the analyses of the reaction products evolution during LWB process. The Mg/Ti joining mechanism was also discussed.

1.2 Problem statement

Joining Mg/Ti by conventional fusion welding processes is extremely challenging because of the huge discrepancies in their physical and metallurgical properties. The melting point of titanium (1678°C) above the boiling point of magnesium (1091°C), thus at typical fusion welding temperature, severe vaporization of the Mg is inevitable. In addition, Ti has 0.12 at.% maximum solid-solubility in Mg, while that of Mg in Ti is nill (Villars *et al.*, 1995). Thus, interfacial reaction between the immiscible couple could be realized by using intermediate element which has substantial solubility in both metals such as Cu and Ni. In contrast to direct joining of Mg/Ti which is mainly a mechanical bonding, with insertion of the interlayer, intermetallic compounds (IMCs) evolved at the interface. However, the quality of the joint and interfacial bonding achieved depended significantly on the IMCs formed (Gao *et al.*, 2012; Tan *et al.*, 2016b). Thus, choosing the suitable interlayer for joining Mg alloys to Ti largely depends on the interlayer composition that gives excellent wetting and bonding without generating thick layers of hard and brittle IMCs at the joint interface. IMCs are solid-phases consisting metallic and non-metallic elements, whose crystal structure varies from other constituents. The

formation of thick IMCs resulted in the degradation of the joint performance. Therefore, when choosing the joining process that will be employed to bond this immiscible couple, minimization of the thickness of IMCs that might form along the interface and minimization of intermixing between the Mg and Ti in the liquid-state are the main factors that must be considered.

The benefits of using laser welding-brazing technique for joining dissimilar materials having large difference in melting point such as Mg/Ti are receiving attention because of the combined attributes of brazing and laser beam welding (Nasiri *et al.*, 2011). With a more laser beam energy control, high cooling rates and joining speeds can be achieved with minimal heating of the base metals. In addition, LWB can minimize excessive formation of the IMCs. If IMCs can be limited below the critical thickness of 10 μm, acceptable mechanical properties may be obtained (Kreimeyer *et al.*, 2005). Therefore, using LWB for joining Mg/Ti is recommended. However, limited work has been reported on Mg/Ti joints by using LWB technique, despite its paramount industrial importance.

1.3   Research objectives

The aim of this research is to explore the application of laser welding-brazing technique to join the Mg/Ti alloys and elucidate the interfacial reaction, mechanical properties and joining mechanism. The main objectives of this research are as follows:

1. To investigate the effect of electrodeposited Cu and Ni layer arrangements (Mg/Ni-Cu/Ti and Mg/Cu-Ni/Ti) on appearance, interfacial reaction and mechanical properties of Mg/Ti joints at different heat input.

2. To examine the effect of the Cu and Ni contents on Mg/Ti joints microstructure development and mechanical properties.

3. To develop the Mg/Cu-Ni/Ti joints bonding mechanisms and identify the key factors liable for the formation of metallurgical bond between the Mg and Ti.

1.4   Scope of the research

In the current work, the effect of the electrodeposited Cu-Ni layer on laser welding-brazing of AZ31/Ti-6Al-4V is investigated. Studies have shown that optimization of the heat input and the content of the interlayer elements were effective ways to regulate the interfacial reaction and changes in microstructure across the joint region. Therefore, the heat input in the current study was optimized by precise control of the laser power output, whereas, other welding parameters such as welding speed and defocus distance were kept constant. In addition, the effect of the interlayer contents on the bonding mechanisms and process was also studied and defined. This work effort is complemented by extensive microstructural characterization (optical and SEM microscopy) of material at and close to the dissimilar weld interface. In addition, numerical simulation of the welding temperature field distribution at different regions of the joint was performed by finite element (FEM) MSC Marc software to help in the analysis of the reaction products evolution during LWB process. The joint quality is estimated through hardness and tensile-shear testing in accordance with American Society of Testing and Materials (ASTM) E384 standard.

1.5   Thesis structure

This thesis consists of five chapters, in Chapter 2, the literature review describes the laser beam welding fundamentals, the general properties and weldability of Mg and Ti alloys and the potentials of various joining techniques used to join these immiscible couples. In addition, it deliberate on some fundamentals on the numerical simulation of laser welding method.

Chapter 3 explained the materials adopted in this study and the experimental procedure. The samples preparation, the electro-plating technique to form coatings, the

characterization of the microstructure, mechanical testing techniques and the numerical analyses of the temperature field are described.

In Chapter 4, the results obtained are presented and discussed, in terms of weld cross-sections, interface characteristics, composition analysis, thermal cycles, hardness distribution across the joints and tensile-shear fracture load. In addition, the join mechanisms are also discussed.

Lastly, Chapter 5 lists the conclusions of the present work and suggestions for future research.

CHAPTER 2: LITERATURE REVIEW

2.1   Introduction

Recently, the use of Mg/Ti hybrid structures in aerospace, aircraft, marine and automotive industries is rapidly increasing because of their inherent properties. This chapter presents the laser beam welding fundamentals and general overview on the properties and weldability of Mg and Ti alloys. The joining techniques for Mg/Ti dissimilar alloys are also discussed, highlighting the strength and weakness of each method. In addition, it provides the reader with some fundamentals on the numerical analysis of laser welding method.

2.2   Laser beam welding fundamentals

2.2.1   Laser beam welding overview

American Welding Society (AWS) defined welding as localized coalescence of materials (metals or non-metals) formed by either heating of the materials with or without the use of pressure, or by the use of pressure only, with or without the application of filler material (Mackerle, 2002). Over the years, numerous joining techniques have been developed in order to achieve high efficiency, joint quality, cost effectiveness, environmental friendly features, ensure safety and reliability of the joined parts (Kumar *et al.*, 2015a).

Among the joining processes, laser beam welding (LBW) gained popularity as the most commonly used non-conventional and advanced joining techniques for welding both similar and dissimilar metals such as magnesium, titanium, steels, aluminum and its alloys in industries because of its flexibility, adoptability, excellent joining qualities coupled with low thermal impact compared with other welding processes (Gao *et al.*, 2013). The theoretical and experimental investigation of laser welding started in 1962. Nevertheless, the application of the technique was reported in 1971 using CO_2 heat

source, beyond which the application of the technology in the high-technology based manufacturing sectors has increased dramatically (Baeslack & Banas, 1981).

During laser beam welding, the materials to be welded absorbed the high power density heat source. LBW can be accomplished with or without filler metal, under different environments like vacuum, air, or controlled atmospheres in the presence of shielding-gas. Besides simple linear welds, advanced laser welding facilities are capable of performing complex non-linear and angular welds (Kochan, 2001). Nevertheless, LBW has some disadvantages, including, the capital costs of laser welding is significantly higher than the traditional fusion processes although it can be compensated with high and excellent joint quality. Additionally, accurate beam and joint alignment, safety requirements and the severe clamping and fitting, and surface preparation before the welding are necessary for obtaining a good quality weld (Cao *et al.*, 2003).

2.2.2   Laser beam welding mode

In general, laser beam welding can be operated on either conduction or keyhole mode depending on the heat input (Kumar *et al.*, 2015a). The conduction mode has a laser power density of less than 10^3 W/cm^2 and the energy absorbed is transferred to the entire weld metal by conduction only (Figure 2.1a). Conduction mode has an aspect ratio of less than 0.5, low coupling efficiency and low welding depth. In contrast, the keyhole mode is generally characterized as a high energy process in the range of 10^5-10^7 W/cm^2. Keyhole is formed inside the weld zone due to the high power density which cause vaporization of the metal as shown in Figure 2.1(b). Under keyhole mode, the aspect ratio is above 0.7, narrower fusion zone and heat affected zone, and high efficiency and high welding depth were reported (Costa *et al.*, 2007).
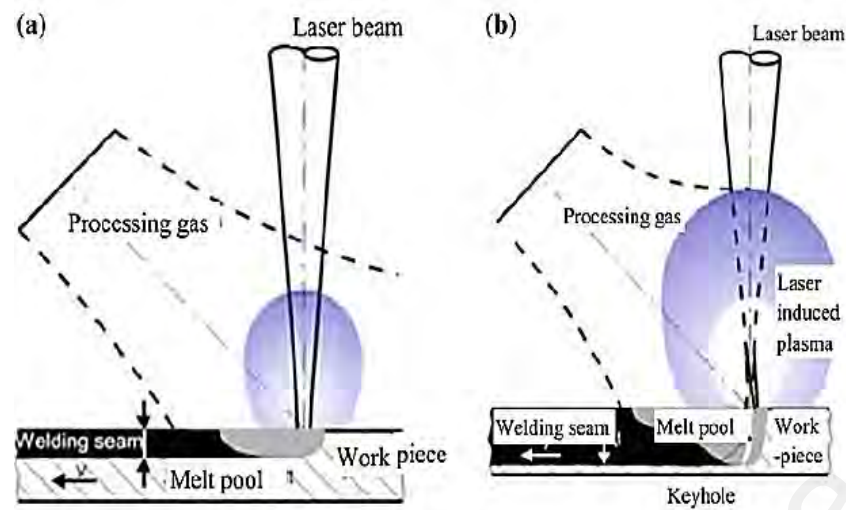
Figure 2.1: Laser beam welding modes: a) Conduction b) Keyhole (Kumar *et al.*, 2015a).

2.2.3 Laser beam welding process-related variables

2.2.3.1 Laser heat source

Materials are joined by different laser heat sources such as Nd:YAG , CO_2, diode, disk, and recently developed fiber lasers. However, CO_2 and Nd:YAG lasers are mostly used. Moreover, Nd:YAG continue to dominate the CO_2 laser as a result of the improvement in the output power, high beam quality and fiber glass delivery (Cao *et al.*, 2006). Disk laser source was reported to have high efficiency and beam quality compared to traditional CO_2 and Nd:YAG lasers (Caiazzo *et al.*, 2013). Recently, fiber laser heat source has gained attention as a suitable welding process for joining Ti and its alloys due of its compact size, high efficiency and beam quality (Campanelli *et al.*, 2015; Evtihiev *et al.*, 2016).

2.2.3.2 Laser power and welding speed

The effect of the laser power on the weld shape have also been reported in the literature. Laser power affect the weld geometry and quality. Many authors reported that the laser power has a direct effect on the weld penetration depth, whereas, welding speed influences the heat input. Generally, an increased in welding speed cause a decreased in

9

temperature due to shorter time for the laser beam to irradiate the workpiece. Therefore, change of welding speed affects the brazing time and the intermetallics formation (Li *et al.*, 2013). Takemoto et al. (2009) laser welded A6061 to steel using Zn filler and observed that the optimum wetting condition of liquid filler was realized at moderate laser output power and welding velocity.

2.2.3.3 Defocused position

Considerable number of studies suggested that the power density is determined by the laser power and the distance between the base metals and the focus plane (Ahn *et al.*, 2016). Kabir et al. (2010) reported that defocusing distance and welding speed could be optimized to obtain a good quality weld with low geometry defects. Kumar et al. (2017) observed that defocused position influenced weld geometry. However, the overall fusion zone area remained unaffected.

2.2.3.4 Shielding gas

Shielding gases are employed to protect the face and root of the weld metal from oxidation, to control convection in the melt pool, to control the plasma plume and protect the optic lenses from weld spatter and fumes (Cao *et al.*, 2003). A poorly shielded weld will exhibit porosity, undercut and bead roughness (Clarke, 2001). The widely used inert gas for shielding are argon, helium or argon-helium mixtures and sometimes nitrogen (Naeem, 1999).

2.3 Magnesium and its alloys

2.3.1 Overview of Magnesium

Magnesium (Mg) belongs to alkaline earth metals in the second group of periodic table. Mg has silvery-white color and comprised 2.7% of the earth's crust which makes it 8th most abundant element (Kulekci, 2008). As the lightest structural material with superior specific strength, Mg received significant attention in recent years particularly

in automotive, aerospace and aircraft industries. Magnesium has been described as a green engineering material and one of the most promising material categories in the 21st century (Liu, 2010). It has low density (1.74 g/cm^3), compared to the density of Ti (4.51 g/cm^3) or Al (2.7 g/cm^3), it is 61% lighter than Ti and 35% lighter than Al, possess excellent strength to weight ratio, excellent formability and damping capabilities, good castability, high elastic modulus, strong ability to withstand shock loads, and recyclability (Mordike & Ebert, 2001; Sakkinen, 1995). Because of these unique properties of Mg, not only heavy metals like steels, cast iron and copper base alloys, but even aluminum alloys are replaced by Mg based alloys (Blawert *et al.*, 2004; Kumar *et al.*, 2015b). However, at elevated temperature Mg alloys have limited strength, fatigue and creep resistance at elevated temperature. At room temperature, the hexagonal close packed (HCP) crystal structure of Mg resulted in limited ductility and cold workability. In addition, Mg alloys have poor surface properties such as low hardness and corrosion resistance, which limits their applications (Cao *et al.*, 2006). Therefore, extensive study is under way to boost the properties of Mg products (Aghion & Bronfin, 2000; Liu, 2010).

Recently, the use of Mg alloys have grown rapidly in high-technology based manufacturing sectors such as automotive and aerospace industries, where weight saving is crucial along with high specific strength (Aghion & Bronfin, 2000; Cole, 2016; Mordike & Ebert, 2001). With growing emphasis on weight reduction, Mg is considered as a material for use in the next generation automobiles, especially using casting approach (Froes *et al.*, 1998; Nasiri *et al.*, 2013b). Based on "Mg Vision 2020", the amount Mg in automobile could increase to as much as 350 lb by the year 2020 (Cole, 2003, 2016).

2.3.2 Magnesium alloys classification

Magnesium is not found in elemental form in nature but only in chemical complexes because of it high reactivity, widely distributed in rock structures, seawater and lake

brines (Kulekci, 2008). Mg is produced through either the metallothermic reduction of magnesium oxide with silicon or the electrolysis of magnesium chloride melts from seawater (Davies, 2003). The mechanical properties of Mg is affected by the production method (Atieh, 2013).

Pure Mg has low mechanical strength. Therefore, alloying has been the most commonly used method to improve properties of the Mg. Precipitation hardening and solid solution hardening are the primary mechanism for enhancing the mechanical properties of Mg. Most of alloying elements forms intermetallic phases with Mg (Kainer & Von Buch, 2003; Kumar *et al.*, 2015b). The main alloying elements are aluminum, zinc and rare earths.

Most Mg alloys are ternary types. Al is the main alloying element in the Mg-Al ternary series, this includes AZ (Mg-Al-Zn), AM (Mg-Al-Mn) and AS (Mg-Al-Si) alloys (Cao *et al.*, 2006). The Mg-Al-Zn group of alloys contains Al, Mn and Zn. These are the most common alloying elements for room temperature applications. The addition of Al (2-9%) with minor additions of zinc and manganese increases strength and hardness of Mg, at the expense of ductility and without impairing weldability and making the alloy responsive to heat treatment (Kulekci, 2008). Fe, Cu and Ni are considered impurities that should be controlled because they degrade the corrosion resistance of Mg alloys. Zn combined with Al overcomes the harmful corrosive effects of Fe and Ni impurities that may be present in Mg alloys. However, the higher the Zn content (over 1%) the higher the hot shortness, causing weld cracking. Mn improves yield strength and the saltwater resistance of Mg alloys (Blawert *et al.*, 2004; Kulekci, 2008).

On the other hand, thorium, cerium and zirconium are used for elevated temperatures and form the Mg-Zn-Zr group. The inclusion of zirconium forms oxides due to its affinity for oxygen, which are active as structure-forming nuclei, leading to physical properties

enhancement through precipitation hardening. The use of thorium or cerium has become more popular since they impart a significant increase in strength at the temperatures of 260°C to 370°C (Kulekci, 2008).

At present, no international code for designating Mg alloys exist. However, the ASTM standard has been the most commonly adopted system. According to ASTM system, the Mg alloys are designated using two letters denoting the major alloying elements, followed by a number, which denotes the nominal composition of the major alloying elements in wt.% (Handbook, 1990). Table 2.1 listed the mechanical properties of selected Mg alloys.

Wrought Mg alloys can be formed by rolling, extruding or forging in the temperature range of 300 to 500°C (Marya *et al.*, 2001). However, wrought semi-products are not available at reasonable costs, thus almost 85 to 90% of all Mg parts are produced by casting methods (Kumar *et al.*, 2015b; Polmear, 1995). In addition, approximately 70% of all Mg castings are produced by die casting. Nevertheless, gas porosity has been the principal challenge for Mg die casting owing to the high filling rate and quick cooling (Froes *et al.*, 1998). At present, there are 4 classifications of Mg die cast alloys commercially available: AZ series (Mg-Al-Zn), AM (Mg-Al-Mn), AS (Mg-Al-Si) and AE (Mg-Al-rare earth).

Table 2.1: Mechanical characteristics of selected Mg alloys (Elthalabawy, 2010).

ASTM	Basic Alloying Elements	Condition	Tensile Properties			Characteristics
			0.2% Proof Strength (MPa)	Tensile Strength (MPa)	Elongation (%)	
AZ31	Al, Zn	Annealed Sheet, Plate	120	240	11	Medium-strength alloy weldable, good formability
		Strain-hardned (H24)	160	250	6	
		Extrusion	130	230	4	
		Forging	105	200	4	
AZ91	Al, Zn	As-sand cast	95	135	2	General-purpose alloy used for sand and die casting
		Solution treated	80	230	4	
		Solution treated and aged	120	200	3	
		As-chill cast	100	170	2	
		Solution treated	80	215	5	
		Solution treated and aged	120	215	2	
HM21	Th, Mn	Sheet, plated solution treated, colded worked and aged	135	215	6	High-creep resistance to 350°C, weldable after short time exposure to 425°C
ZC63	Zn, Cu	Solution treated, aged	145	240	5	Pressure-tight casting, good elevated temperature strength, weldable
ZK51	Zn, Zr	Aged	140	253	5	Sand casting, good room temperature strength and ductility

Among the commercially available series, considerable attention was given to the Mg-Al-Zn system because it can be cast and formed by extrusion. In addition, the presence of the Al and Zn alloying elements enhanced the tensile and yield strength of the Mg-Al-Zn system (Kumar *et al.*, 2015b; Zhang & Xu, 2008). Recently, Mg-Al-Zn system has been applied in the auto-industries such as Volkswagen in the manufacture of various components (Davies, 2003; Kawalla *et al.*, 2008; Nasiri, 2013).

2.3.3   Weldability of magnesium alloys

The existence of weld imperfections such as oxide films and cracks restricted the Mg alloys to be welded except for some repaired structures (Haferkamp *et al.*, 2000). Hence, reliable joining process is inevitable for wider application of Mg alloys. Based on the existing literature, the weldability of Mg alloys components were investigated by mechanical fasteners and variety of joining techniques such as electron beam welding, tungsten arc inert gas (TIG), friction welding, metal arc inert gas (MIG), spot welding and laser beam welding (LBW) (Cao *et al.*, 2006; Manladan *et al.*, 2016). At present, MIG and TIG techniques are the commonly used welding techniques for Mg alloys. However, limitations still exist where the low speeds, large heat affected zone (HAZ) and fusion zone (FZ), high residual stress and distortion of arc-welded joints have caused attention to be drawn towards laser beam welding (Marya *et al.*, 2001; Schubert *et al.*, 2001), due to its high flexibility, adaptability, low residual stress coupled with low and precise heat energy input compared with other welding processes (Dilthey *et al.*, 1999; Kumar *et al.*, 2015b).

The effectiveness of the LBW of Mg alloys depends on its physical properties. Some of the inherent characteristics of Mg alloys include: high thermal conductivities and coefficients of thermal expansion, large solidification temperature ranges, strong tendency to oxidize, low viscosity and surface tensions, low laser beam absorptivity, high

solidification shrinkage, low melting and boiling temperatures and large freezing range of 420 to 620°C (Nasiri, 2013; Sakkinen, 1995). Noteworthy, LWB of Mg alloys has some processing complications and weld imperfections where the formation of unstable weld pool, spatter, undercut, porous oxide inclusions, loss of alloying elements, solidification and liquation cracking still exist (Marya *et al.*, 2001). Nonetheless, under optimum processing conditions, crack-free wrought Mg alloys laser welded joints with minimum imperfections can be achieved (Kumar *et al.*, 2015b; Weisheit *et al.*, 1998).

2.4   Titanium and its alloys

2.4.1   Titanium alloys overview

Titanium is the 9th most abundant element on the planet and 4th most copious structural material after Al, Fe and Mg. It was first discovered in England and Germany in 1790 and purified in early 1900s. Titanium and its alloys are one of the commonly used engineering materials in many areas of applications ranging from aerospace, medical, biomedical, biomaterial, petrochemical industries because of their low density, excellent corrosion resistance, high strength, and biocompatibility (Lütjering & Williams, 2007).

In recent years, Ti alloys has been used extensively in the manufacture of aero-engines (due to its high strength, high creep resistance); aircraft (high-strength-to-weight-ratio) and chemical industry (excellent corrosion resistance) (Fujii *et al.*, 2003; Schutz & Watkins, 1998). Nevertheless, the cost of Ti alloys raw material and fabrication restricted its applications to critical parts in which its usage is crucial for the desired performance (Lütjering & Williams, 2007).

The extraction of pure Ti is difficult because Ti is highly reactive metal, i.e. it easily reacts with oxygen and nitrogen and even with other refractories in the molten state. Ti has a higher melting point than Fe and its density falls in the intermediate between those of Al and Fe. Due to its non-magnetic nature, the thermal conductivity of Ti is low. The

high melting temperature and high reactivity to atmospheric gases at typical fusing temperatures make Ti alloys difficult to machine couple with the need of consideration in heating for fabrication at high temperatures and for welding (Kulkarni, 2015).

Titanium is an allotropic element (exists in more than one crystallographic form). Thus, it exits in hexagonal close packed (HCP) crystal structure called alpha phase (α-phase) and body centered cubic (BCC) crystal structure called beta phase (β-phase). However, the Ti exists in α-phase at room temperature. This crystal structure changes from α-phase to β-phase at 883˚C and is stable up to the melting temperature (Boyer, 1985; Kulkarni, 2015). The manipulation of these crystallographic variations through alloying additions, heat treatment, and thermo-mechanical processing are the source for the development of a broad range of Ti alloys and properties (Kulkarni, 2015).

The addition of alloying elements influence the transformation temperature, i.e. the alloying elements divides the single temperature for equilibrium transformation into two temperatures: α-transus and β-transus. The "α-transus" denote the temperature above which the α-phase begins to transform to β-phase, whereas, the "β-tansus" is the temperature above which it is all β-phase. Generally, the alloying elements can be classified as alpha or beta stabilizers. Some elements such as Ni, Fe and Cu decreased the transformation temperature and are called beta stabilizers. In contrast, elements such as Al, C, and O which increase the transformation temperature are called alpha stabilizers. Some elements, notably tin and zirconium behave as neutral solutes in Ti and have little effect on it (Leyens & Peters, 2003; Zhecheva *et al.*, 2005). Table 2.2 provides the list of most popular alloying elements used in Ti alloys and their stabilizing effect.

Table 2.2: Stabilizing effect of alloying elements on Ti alloys (Davis, 1997).

Alloying Elements	Range (wt.%)	Effect on structure
Aluminum	2−8	α stabilizer
Tin	2−11	α stabilizer
Chromium	2−12	β stabilizer
Copper	2−6	β stabilizer
Molybdenum	2−15	β stabilizer
Niobium	1−2	β stabilizer
Vanadium	2−20	β stabilizer
Zirconium	2−8	α and β strengthening
Silicon	0.05−1	Improves creep resistance

2.4.2   Titanium alloys classification

Titanium are classified into four categories, alpha (α) alloy, near alpha alloy, alpha and beta (α+β) alloy, and beta alloy (β). Table 2.3 shows the mechanical properties of various Ti alloys. In general, α alloy has higher ductility, but lower strength, whereas, β alloys has higher strength but lower ductility and poor weldability. On the other hand, α+β alloys displays a good balance of strength and ductility (Kumar *et al.*, 2015a).

Table 2.3: Comparison of mechanical properties of α, β and α+β (Leyens & Peters, 2003).

Mechanical Properties	α	β	α+β
Ductility	Medium	Low	High
Strength	Medium	Extreme high	High
Weldability	High	Low	Medium

At present, there are more than hundred grades of Ti alloys, but only about 20-30% have been commercially available. Among the various grades commercially available,

Ti-6Al-4V (T64) account for 56% of the total usage in industries (Atieh, 2013). The composition of Ti64 comprises Al as α-stabilizer and V as β-stabilizer. At room temperature, the microstructure of the T64 in equilibrium contained primarily α phase with some retained β phase (Caiazzo *et al.*, 2014). The β transus temperature for Ti-6Al-4V is about 995˚C.

Depending on the cooling rate and the prior heat treatment condition, the micro-constituents and microstructures of Ti64 are divided into several types, namely grain boundary allotriomorph α, primary α, Widmanstatten basket weave and martensitic (Kumar *et al.*, 2015a). Squillace et al. (2012) reported that the high heating above the beta transus and fast cooling rate were the main cause of martensitic α′ formation. The authors suggested a cooling rate of 410˚C/s for the base metal of Ti64 alloy for complete transformation to martensitic α′ phase.

Moreover, Ti-6Al-4V has an outstanding biocompatibility, superplastic formability, corrosion resistance and high specific weight, which facilitates its applications in aerospace, chemical, biomedical, nuclear and marine industries. The heat of fusion of Ti-6Al-4V is twofold of Fe. However, its thermal conductivity is very poor. In view of these unique properties, the welding of Ti-6Al-4V by traditional joining processes is challenging (Yang *et al.*, 2010).

2.4.3 Weldability of titanium alloys

Weldability refers to as the ability to produce a quality weld under specific welding condition. During welding, the base materials microstructure and mechanical properties change at the weld zone. Ti and its alloys are considered weldable by advanced joining techniques, namely plasma welding, electron beam welding and laser beam welding. The investigation of weldability and characterization of Ti joints is promising challenge for research and development (R & D) (Kumar *et al.*, 2015a).

Considerable number of authors reported that commercially pure Ti and all α alloys have good weldability, strength and toughness (Amaya *et al.*, 2013; Destefani, 1992). On the other hand, α+β exhibited an excellent formability and weldability and their properties are affected by heat treatment. Besides, Ti-6Al-4V is the best weldable amongst the α+β. In contrast, β alloys exhibited poor weldability owing to the degradation of strength after welding (Destefani, 1992).

Interestingly, the low thermal conductivity of Ti alloys prevents heat dissipation during welding. Costa et al. (2007) demonstrated that under suitable joining processing, Ti-6Al-4V welds has the ductility and corrosion resistance almost similar to that of the base material, whereas, inappropriate welding method embrittled the joint.

Titanium alloys have high rate of laser beam absorption (0.4%) and high melting temperature (about 1670˚C), thus requiring extremely high energy to weld. Therefore, joining Ti alloys by LBW technique is the most viable option (Quintino *et al.*, 2007). Recently, laser beam welding gained popularity as a promising joining technology for Ti alloys in industries because of its high precision, high weld quality, high efficiency, excellent flexibility, in addition to low deformation and distortion compared to other traditional welding processes (Kumar *et al.*, 2015a; Zhang *et al.*, 2014).

Nevertheless, the laser beam welding techniques for Ti alloys is a complicated process because of the necessity to fulfil some specific requirements. Ti alloys were reported to be extremely active at high temperatures, particularly in a molten state and readily pick up atmospheric gases, dirt, grease and refractories leading to embrittlement of the weld pool. Therefore, Ti alloys during laser beam welding have to be completely shielded in an inert or vacuum environment (Costa *et al.*, 2007). The widely used inert gas for shielding the Ti alloys welds are argon, helium or argon-helium mixtures. However, argon is the most preferred choice for Ti alloys welds.

2.5   Advances in welding and joining Mg/Ti alloys

2.5.1   Introduction

The flexibility in the production of components was enhanced by the incorporation of joining technology in the manufacturing process. However, careful selection of the joining techniques for the dissimilar parts is essential (Atieh, 2013). Different joining processes have been attempted to join Mg/Ti, and they can be categorized as solid-state processes such as friction stir welding (FSW), diffusion bonding and fusion-based processes, including arc welding and laser beam welding. To achieve metallurgical compatibility and joint formation, these processes are used in combination with interlayers/filler metals such as Al, Zn, and Ni. In this section, the potential of these methods for joining Mg/Ti are reviewed.

2.5.2   Solid-state joining processes

Several solid-state joining methods have been used to weld Mg/Ti. The formation of defects such as surface voids and cracks are often eliminated because the parent metals remain in the solid-state. Nonetheless, the service conditions could make specific methods inappropriate as most of the processes are applicable to only certain geometries. Generally, in solid-state joining, the joint performance is influenced by the intimate contact between the dissimilar materials and the microstructure, particularly the formation of IMCs (Chen & Nakata, 2010).

2.5.2.1 Friction stir welding (FSW)

Friction stir welding (FSW) is a solid-state joining method that operates by generating frictional heat between a rotating tool and the base materials. The welds are created by the combined action of frictional heating and plastic deformation due to the rotating tool. Compared to traditional fusion welding, FSW offers some unique advantages such as absence of flux or filler and very high heat efficiency. In addition, with combination of

frictional heat and intense deformation caused by the tool, local forging and stirring effect resulted in metallurgical bonding, which in turn improved the bond strength (Aonuma & Nakata, 2009, 2010, 2012). The typical schematic of FSW is shown in Figure 2.2. The probe was inserted in Mg alloy side and offset slightly into Ti sheet side to guarantee direct contact between them (Fukumoto *et al.*, 2004; Watanabe *et al.*, 2005).
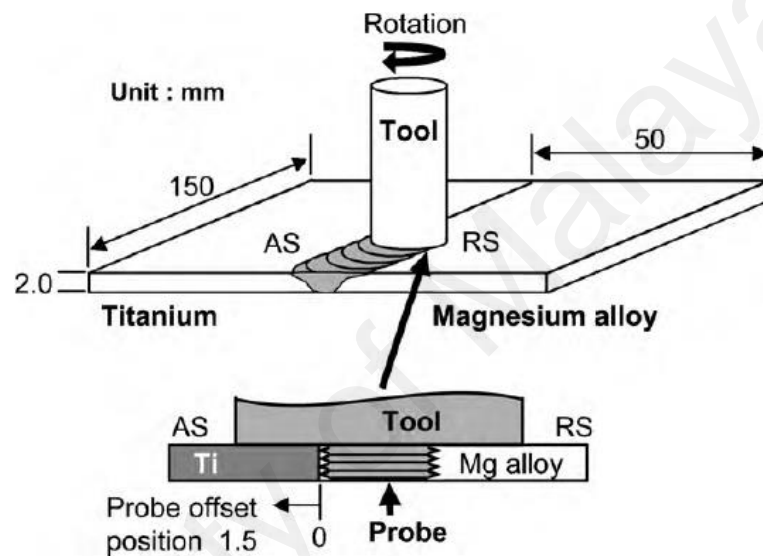
Figure 2.2: Illustration of FSW process (Aonuma & Nakata, 2010).

There is limited work conducted on FSW of Mg/Ti alloys. Aonuma et al (2009) investigated friction stir lap-welded TA2 and Mg-Al-Zn (AZ31B, AZ61A, AZ91D) alloys. The interfacial characterization showed that Ti-Al IMC layer identified as $TiAl_3$ was observed at the Ti interface. Furthermore, when the amount of Al in magnesium alloy increased, the thickness of Ti-Al IMC increased, whereas, the tensile strength decreased as shown in Figures 2.3 and 2.4, respectively. Aonuma et al. (2010) examined the effect of Ca and Al alloying elements on friction stir lap-welded Mg–Al–Ca (AMCa602 and AM60)/TA2. For AM60/TA2 joints, a thick $TiAl_3$ intermetallic was formed at the

22

interface because the Al element in the matrix is in solid solution condition and easy to diffuse at elevated temperature, whereas, a thin layer of Ca and Ti-Al layer were observed for AMCa602/TA2. Because of the high affinity of Ca and Al (Yamamoto *et al.*, 2007), the content of Al in the sold-solution of AMCa602 matrix was reduced by Al_2Ca compound formation. The formation of Al_2Ca suppressed the growth of the $TiAl_3$ and improved the joint performance. Aonuma et al. (2012) also studied the performance of ZK60/TA2 joints produced using FSW. The results showed that a thin layer rich in Zn and Zr was produced, which enhanced the joint performance (237 MPa). In contrast, no reaction layer was observed when pure Mg was joined to TA2 which resulted in poor tensile strength (135 MPa).
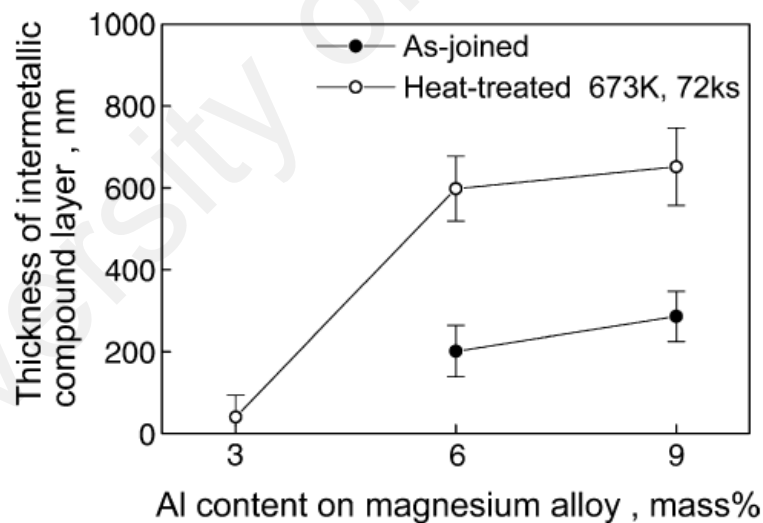
Figure 2.3: Effect of Al contents on friction stir welded TA2/Mg-Al-Zn IMC thickness (Aonuma & Nakata, 2009).
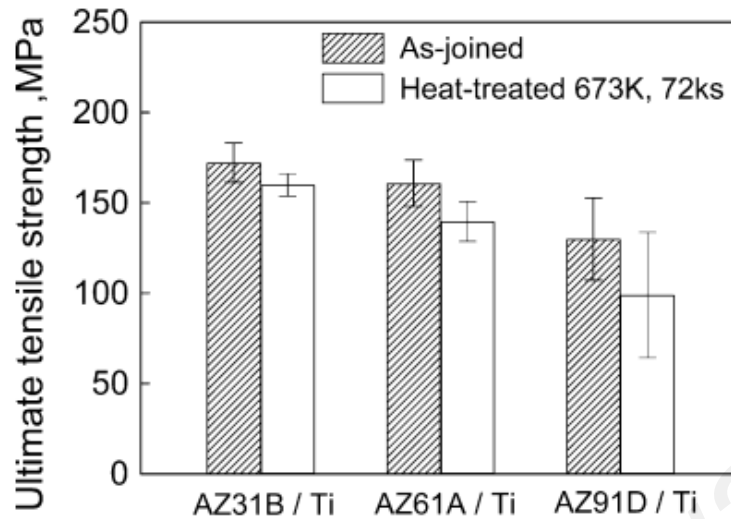
Figure 2.4: Ultimate tensile strength of Mg alloy/Ti joints with increasing Al content (Aonuma & Nakata, 2009).

Tanabe and Watanabe (2008) studied the performance of AZ31B/commercially pure Ti (CP-Ti) joints produced using FSW. They reported that Ti fragments in Mg affected the joint strength. The probe geometry was found to influence the joint strength.

The friction heat generation and atom diffusion behavior during ZK61/TA2 friction welding were also examined, and rotational speed and axial pressure played an important role in the defining the temperature and friction coefficient (LI *et al.*, 2012). Recently, Lakshminarayanan et al. (2015) investigated the performance of friction welded AZ31B/CP-Ti. The mechanical metal transfer caused by higher strain rate and excessive plastic deformation resulted in grain refinement. Phase analysis showed that the Al from the Mg base metal diffused toward the weld interface and produced a thin discontinuous IMC (identified as Ti$_3$Al) by reacting with Ti at the weld interface. Figure 2.5(a) and (b) show the SEM micrograph and SEM-EDS of the Mg-Ti. As shown on Figure 2.5(a), the average thickness of the thin discontinuous IMC was below 15 µm. The SEM-EDS line

scan shown in Figure 2.10(b), shows the segregation of Al at the interface, while Ti and Mg changed steadily.

The major drawback of FSW may be related to the processing heads, which impose size and shape limitations. Thus, the process is best use with long and straight welds. In addition, keeping the interlayer at the interface between the Ti and Mg is very difficult due to the stirring action of the pin and material flow with high plasticity along the interface. Thus, FSW is not widely adopted by automotive and other mass production industries.
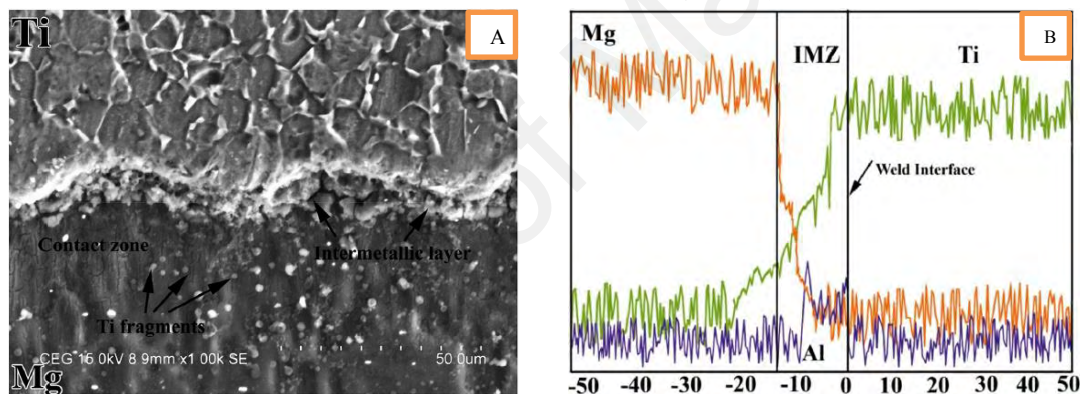
Figure 2.5: (a) SEM image of Mg-Ti interface and (b) SEM-EDS line scan (Lakshminarayanan *et al.*, 2015).

2.5.2.2 Diffusion bonding

Diffusion bonding relies on combination of micro-deformation at the bonding interface and the inter-diffusion of atoms between the materials being joined (Freer, 1982). Diffusion bonding has the potential to produce a perfect welds with no fusion zone and an absence of heat affected zone. However, the process is cost-effective only when close dimensional tolerances, expensive materials or special material properties are involved. Even then, not all metals can be easily or effectively diffusion bonded.

Transient liquid phase (TLP) bonding which is a variant of diffusion bonding, is an alternative technique for welding advanced alloys such as Mg to Ti alloys (Atieh & Khan, 2013, 2014a, 2014b, 2014c, 2014d; Jiangtao *et al.*, 2006). During TLP bonding, metallurgical bonding is achieved with addition of thin interlayer that forms a eutectic reaction at the bond region (Cook & Sorensen, 2011). Through isothermal solidification accompanied by solid state homogenization, joints with microstructure characteristics and mechanical properties comparable to the parent materials could be achieved (Atieh, 2013).

Xiong et al. (2006) investigated the diffusion bonding behavior of Mg/Ti using a pure Al interlayer. Bonding temperature was observed to have great effect on the kinetic factors of AZ31B/Al/Ti-6Al-4V interfacial reaction, which decided the composition and distribution of the reaction product. When the bonding temperature was lower than 450°C, no liquid phase was produced and bonding of AZ31B and Ti-6Al-4V was difficult to be realized. The joint with maximum shear strength of 72.4 MPa, which is 84.2% of AZ31B strength, was achieved after bonding at 470°C for 180 min. The joints were bonded by $Mg_{17}Al_{12}$ and Ti_3Al phases at the interface. Atieh et al. (2013) examined the effect of bonding parameters on microstructural development and joint strength of TLP bonded AZ31 Mg alloy to Ti6Al4V using pure Ni interlayer. They reported that the shear strength of the joints reached a maximum value of 39 MPa for a bonding time of 20 min at 540°C. However, joint strengths decreased with an increase in bonding time to 60 min due to the formation of intermetallics within the joint during isothermal solidification. The long thermal cycle of diffusion welding/brazing process promotes the formation of brittle intermetallic compounds along the interface of dissimilar joints. In contrast to the traditional TPL process, the microstructural characterization of the joints revealed that the bonding mechanism involves Ni-Mg eutectic formation at the Mg-interface with solid-state diffusion and bond formation at the Ti-interface, thus, it was characterized as

"semi-solid TPL bonding". Considerable increase in the joint performance to 57 MPa was observed when Ni and Cu sandwich foils where employed (Atieh & Khan, 2014d). The low shear strength observed was attributed to the fact the foils thickness produced a large volume of thick IMCs. These IMCs reduce the direct contact area and, hence, affect the bond strength. Moreover, improvement in the joint shear strength was achieved with electroplated coatings (Atieh & Khan, 2014b, 2014c). For instance, electrodeposition of thin (12 μm) coating improved the flow and uniformity of the liquid, which enhanced the joint strength to 61 MPa at optimum TPL bonding parameters (520°C, 0.2 MPa, 20 min) (Atieh & Khan, 2014c). In addition, the maximum shear strength of 69 MPa was obtained with an electrodeposited Ni coating containing a dispersion of nanoparticles of pure Cu (Atieh & Khan, 2014a). The addition of nanoscale copper dispersion in Ni coating facilitates the bonding process through shorter diffusion distances. However, the bond strength could be severely affected by the IMCs formation and agglomeration of the nanoparticles as shown in Figure 2.6. Therefore, careful selection of the type and application of nanoparticle dispersion is crucial.

In general, selection of the bonding parameters (bonding temperature, bonding time, applied pressure and surface roughness) played a significant role in getting a sound joint. Beside process parameters, the joint strength and the microstructural developments is influence by the interlayer material. Furthermore, nanoparticles dispersed coat could improve joint strengths significantly (Atieh & Khan, 2014a). The use of different interlayer facilitate the bond realization in both solid-state and liquid-phase diffusion bonding processes. In contrast to high bonding temperature and pressure are required for direct joining without interlayer, using eutectic interlayers lowered the temperature and applied pressure. However, IMCs are formed (Atieh, 2013). Nevertheless, diffusion bonding is limited to certain geometries and the bond formed are characterized by weak strength. Thus, diffusion bonding is not classified as a mass production process.
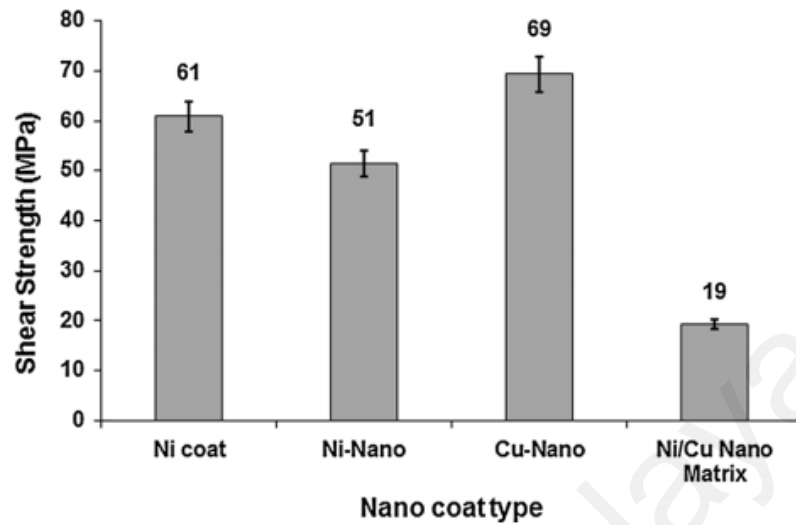
Figure 2.6: Shear strength of AZ31/Ti6Al4V joint under different coat types (Atieh & Khan, 2014a).

2.5.2.3 Ultrasonic spot welding

In principle, ultrasonic spot welding (USW) is a solid-phase joining process that is characterized by a low energy input and a short welding time. During USW, the welds is achieve using frictional interaction formed under pressure by transferring hing frequency vibration waves onto the surfaces. At present, the research conducted on joining Mg alloys to Ti using USW is limited (Ren *et al.*, 2017; Zhao *et al.*, 2017). Ren (2017) investigated the weld strength and microstructure at the joint interface of ultrasonically welded AZ31B and Ti6Al4V alloys. The results showed that grain refinement occurred on the Mg interface. Unlike during FSW (Aonuma & Nakata, 2009, 2010) and laser welding (Tan *et al.*, 2016a; Tan *et al.*, 2016b) where Ti/Al IMC layer was observed at joint interface, neither transition layer nor IMC was formed during USW probably because its very low heat input compared to those joining techniques. Therefore, the bond is achieved on a micro-scale.

2.5.3 Fusion welding processes

Fusion welding is the most commonly used welding technique for joining metals (Sun & Karppi, 1996). Therefore, considerable number of authors concentrated on joining of dissimilar metals using these methods despite their obvious difficulties, such as coarsening of the grain size, voids and cracks at typical fusion welding temperature. During fusion welding, the joint formation is achieved by melting and solidification (Atieh, 2013). There are different fusion welding processes, such as conventional shielded metal arc, gas tungsten arc, gas metal arc, submerged arc welding, electron beam welding and laser welding. Of these processes, gas metal arc welding (Cao *et al.*, 2014), gas tungsten arc (Xu *et al.*, 2014a; Xu *et al.*, 2017; Xu *et al.*, 2014b; Xu *et al.*, 2016), and laser beam welding (Gao *et al.*, 2011; Gao *et al.*, 2012; Tan *et al.*, 2016a; Tan *et al.*, 2016b; Tan *et al.*, 2017b; Zang *et al.*, 2018; Zhang *et al.*, 2018b) have been investigated for joining Mg alloys to Ti.

2.5.3.1 Cold metal transfer (CMT) welding

Cold metal transfer (CMT) welding is a modified metal inert gas (MIG) welding, introduced a new way to join advanced materials, especially dissimilar materials such as Mg/Ti and Mg/Steel (Cao *et al.*, 2014; Cao *et al.*, 2016). The cold metal transfer welding uses a new method of droplet detachment based on short circuit welding, which reduced thermal input and resulted in low distortion and high precision. Cao et al. (2014) joined AZ31B/TA2 by CMT technique using two lap configurations as illustrated in Figure 2.7. It was found that for the two configurations; the brazing interfaces were consisted of Ti_3Al, $Mg_{17}Al_{12}$ and $Mg_{0.97}Zn_{0.03}$ IMCs resulted from the diffusion of Al and Zn from the molten Mg and the filler wire, which reacted with Ti substrate. The highest shear load of 2.1 kN was achieved for Mg-Ti joint compared to only 1.83 kN for Ti-Mg joint.

To enhance the joints performance during CMT welding, the local melting of the Ti was the key, unfortunately the arc temperature made the Ti base metal to melt little because the melting point of the wire was merely 649˚C. Future researchers should concentrate on offsetting the filler wire towards the Ti sheet to address this problem.
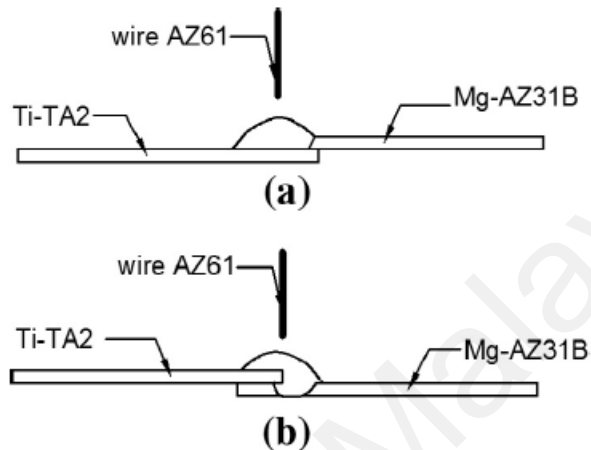
Figure 2.7: Illustration of (a) Mg-Ti and (b) Ti-Mg joints (Cao *et al.*, 2014).

2.5.3.2 Tungsten inert gas (TIG) welding

Tungsten inert gas (TIG), a variant of arc welding, offers additional benefits such as flexibility, high efficiency, good joint quality, and has the potential to join dissimilar metals such as Mg/Ti (Xu *et al.*, 2014a; Xu *et al.*, 2017; Xu *et al.*, 2014b; Xu *et al.*, 2016). In TIG welding, the arc is maintained between the workpiece and a tungsten electrode. This process uses a non-consumable electrode where gas is fed through the torch to shield the electrode and molten weld pool.

Xu et al. (2014a) studied the TIG lap welded TA2/AZ31B dissimilar metal joints using AZ31B Mg based filler. It was found that the coarse-grained fusion zone with precipitated phase of $Mg_{17}Al_{12}$ and a distributed Mg/Ti solid solution were observed. Under optimum process parameters a joint with maximum shear strength of 193.5 Nmm^{-1} was obtained. However, excessive grain coarsening was observed at the fusion zone due to wide

differences in thermal properties of the base metals. To enhance joint characteristics, dynamic grain refining method using ultrasonic assisted TIG brazing techniques were used. With the ultrasonic power (1.2 kW) applied in the molten metal and subsequently solidification stage, nucleation and cooling rates of molten metal were increased, leading to the efficient refinement of columnar α-Mg grains and enhanced the joint strength 193 Nmm^{-1} to 228 Nmm^{-1} (Xu *et al.*, 2014b).

In comparison, Xu et al. (2016) examined the TIG welding behavior of a AZ31B to Ti-6Al-4V using AZ31B filler wire. Robust joints were obtained with welding current in the range of 60-70 A, and Mg/Ti diffusion reaction layers accompanied with Mg$_{17}$Al$_{12}$ precipitate phase were formed at the interface of the joint. A joint with maximum tensile strength of 190 MPa was achieved. Further improvement in the joint performance was obtained using high-energy shot-peening (HESP) treatment (Figure 2.8) (Xu *et al.*, 2017). The addition of the HESP treatment eliminated the surface voids and cracks and introduced high compressive residual stress and surface strain strengthening. As shown in Figure 9(a and b), lots of voids and cracks occurred for the TIG welded Mg/Ti interface without HESP treatment. However, these defects were almost eliminated through plastic deformation of the surface layer induced by HESP, as illustrated in Figure 2.9(b, c, e and f). When the peening time was 60 s and peening pressure was 0.15 MPa, a joint with maximum tensile strength of 241 MPa was achieved.
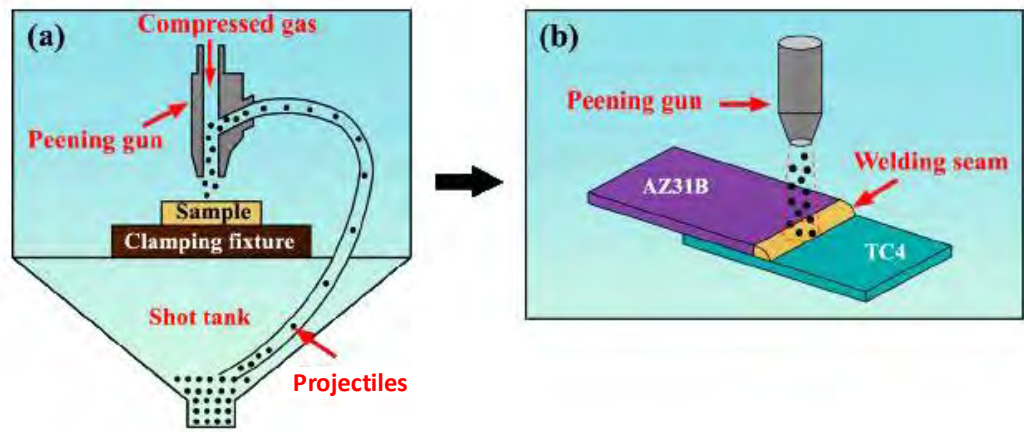
Figure 2.8: Schematic of HESP assisted TIG process (Xu *et al.*, 2017).
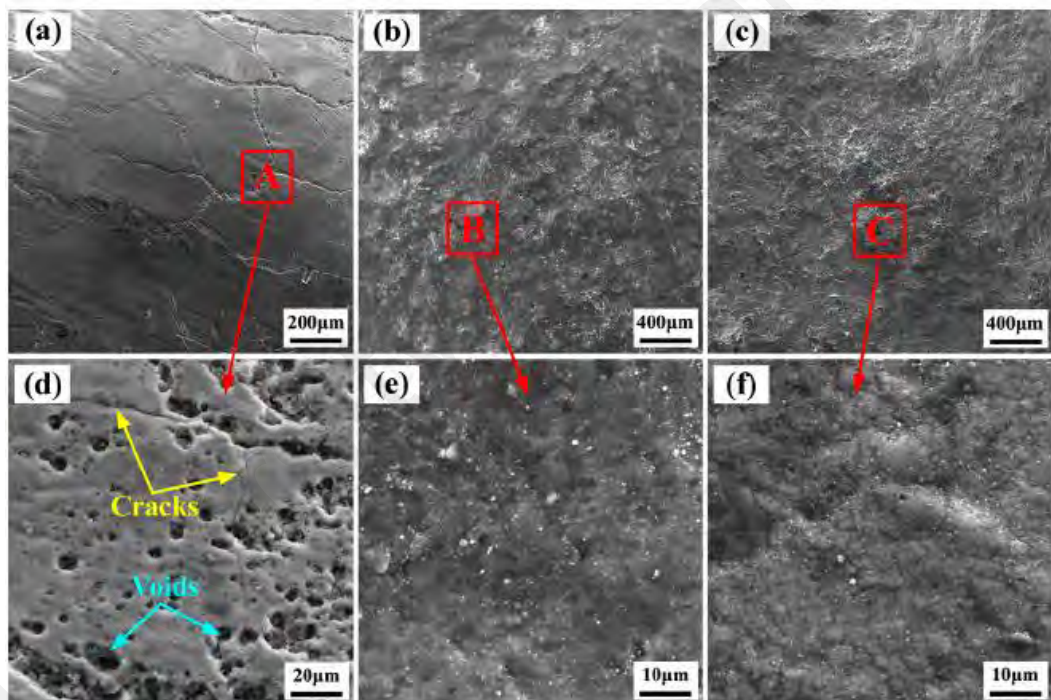
Figure 2.9: Surface appearance of HESP assisted TIG welded-brazed Mg/Ti joints: (a)-(c) 0 s, 60 s, and 180 s peening times; (d)-(f) higher magnification images of region a, b and c (Xu *et al.*, 2017).

Different authors employed various techniques to enhance the joint mechanical resistance. However, compared with Mg alloy base metal the joint performance is still low. Thus, extensive study is still required to improve the joint mechanical resistance.

Although some degree of success has been achieved with ultrasonic and HESP assisted TIG, other surface strengthening technology should be explored.

2.5.3.3 Laser beam welding (LBW)

Laser beam welding presents a viable option for welding dissimilar metals such as Mg/Ti due its flexibility, adaptability and excellent joining qualities (Baqer *et al.*, 2018; Gao *et al.*, 2011; Gao *et al.*, 2009). Despite the lack of intermixing between the Mg and Ti at typical fusion welding temperature, joining Mg/Ti in keyhole mode was examined (Gao *et al.*, 2012). Gao et al. (2011; 2012) performed laser welding of AZ31B to Ti-6Al-4V butt joints using AZ31 filler. The authors showed that laser beam offset influences the joint formation. Mg-Al eutectic and α-Mg were observed at the interface of the joints which the authors believed to have played a role in enhancing the joint strength.

In contrast, laser heat conduction welding technique has also been explored to joined this immiscible couple using Al foil (Zang *et al.*, 2018) and Ni coating (Zhang *et al.*, 2018a) by Tan and his co-workers. For Al added joints, $TiAl_3$ was produced at the fusion zone-Ti interface. The thickness of the $TiAl_3$ IMC layer slightly changed while Mg-Al become denser with the increasing Al interlayer thickness. The analysis of the joint mechanical resistance showed that the Al interlayer thickness also affected the joints tensile shear performance as shown in Figure 2.10. In contrast, the effect of laser power on Mg/Ni/Ti joints showed that the Ni coated layer diffused into the Ti substrate creating and a Ti solid-solution and Ti_2Ni. The thickness of the reaction layer increased with increased in laser power. At optimum laser power (1500 W), tensile shear performance of 144 N/mm was achieved. However, the instability of the Mg molten pool under the action of gravity coupled with the severe evaporation of the Mg base metal made the laser heat conduction welding method unsteady as shown in Figure 2.11.

Therefore, to address the vaporization of the Mg and enhance the process stability, laser welding-brazing (LWB) with Mg based filler wire was proposed. Tan et al. (2016a; 2016b) examined AZ31B/Ti-6Al-4V lap joints made by LWB methods using Mg based filler. It was observed that direct joining or using a filler wire with low Al content resulted in the mechanical bonding. In contrast, a thin interfacial reaction layer was present when Al content in the Mg-filler was 9% (AZ91). The newly formed layer was analyzed by TEM bright field image (Figure 2.12a and b) and HAADF micrograph (Figure 2.12c) with corresponding SADP (Figure 2.12d). The thin IMC was indexed as Ti-rich Ti_3Al phase. The formation Ti_3Al interfacial layer prevented crack propagation and enhanced the joints performance (Tan *et al.*, 2016a). The outcome of this study proved that Al played an indispensable role in Mg/Ti joint formation and controlling the heat input of welding parameter and the content of interlayer elements were effective ways to regulate interfacial reaction. However, the content of the Al was not easy to control because of the limited Al content added in the Mg filler (9 wt% is considered as maximum Al content without excessive erosion of the base metals). Therefore, addition of suitable interlayer material is still required.
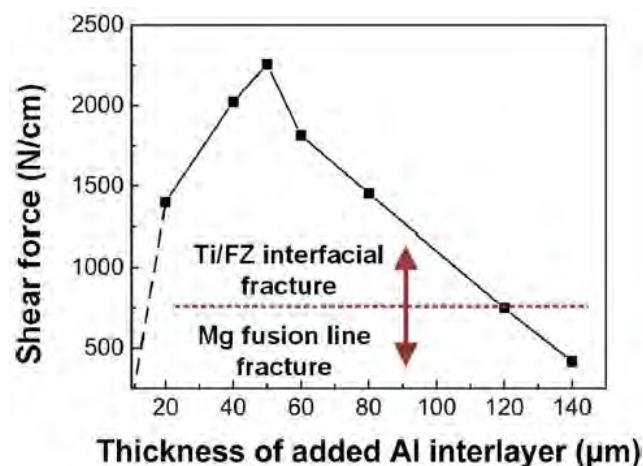
Figure 2.10: Mg/Ti joint tensile-shear performance at different Al thickness (Zang *et al.*, 2018).
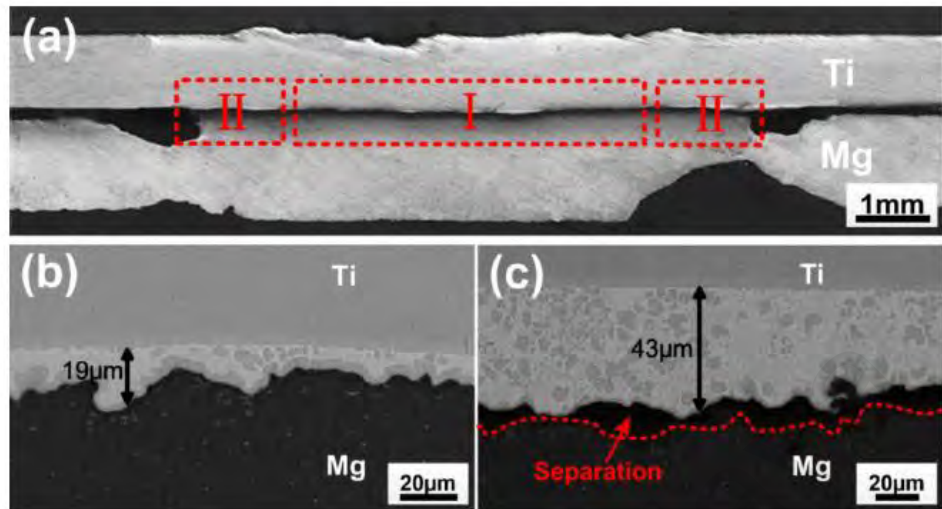
Figure 2.11: Laser conduction welded Mg/Ti: (a) optical micrograph, (b) SEM micrograph of the zone I in (a) and (c) SEM micrograph of the zone II in (a) (Zhang *et al.*, 2018a).
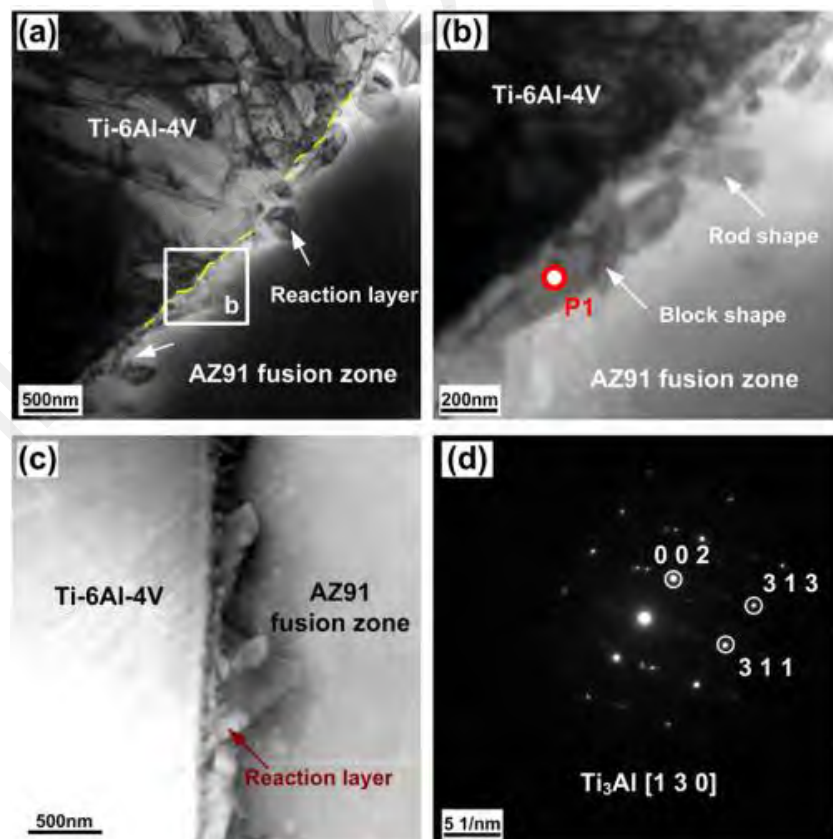
Figure 2.12: TEM images of Mg/Ti joint interface: (a) Interface bright field image, (b) Higher magnification of (a), (c) HAADF image of (a) and (d) SAED of the interface (Tan *et al.*, 2016a).

2.6   Numerical simulation of laser beam welding

Laser beam welding has received great attention for industrial production in the last two decades due to its high flexibility and excellent joint qualities (Otto & Schmidt, 2010). However, the full potential of the technique has yet to be realized. Complicated phenomena occur during laser beam welding such as laser light absorption and temperature dependency of material properties occur in a little time. In addition, optimizing the process parameters using the traditional trial and error approaches have faced a lot of complications. Therefore, the pre-requisite for enhancing the reliability of laser beam technology is by thorough understanding of the beam-material interaction, the resulting process dynamics and the development of appropriate control techniques (Tsirkas *et al.*, 2003).

In recent years, numerical simulation of the welding method has gained enormous importance in welding research, such that the physical essence of some complicated phenomena can be explicitly clarify with aid of simulation results. In addition, it facilitates assessment of distortions, transient and residual stresses. Moreover, phenomenological models resulting from the experimental findings can be verified by means of an application into the simulation model (Otto & Schmidt, 2010). Nevertheless, the full potential of laser technology simulation has yet to be realized due to the complexity of the techniques where different physical phenomena such as metallurgical, thermal and mechanical interacted with each other (Tsirkas *et al.*, 2003). To minimize the complexity of the simulation process in the state of the art models most of these physical phenomena are considered as decoupled or even neglected based on the process to be simulated. Therefore, these models can only examine certain effects of the processing such as thermal cycles or residual stresses.

Based on the existing literature, the distortions, transient and residual stresses of structural parts during the welding process have been extensively studied using a number of analytical numerical models. These include analytical models (Tanigawa *et al.*, 1996; Yang & Xiao, 1995), 2D (dimensional) FEM (Fujii *et al.*, 2000), and 3D FEM of laser (Frewin & Scott, 1999; Tsirkas *et al.*, 2003) and arc welding (Brown & Song, 1992; Karlsson & Josefson, 1990). Nevertheless, in these models not all the process parameters affecting the welding were taken into consideration. It has been enormously agreed that introduction of the metallurgical transformation into the model and correct representation of the keyhole are the most influential aspects of the laser beam welding simulation (Frewin & Scott, 1999; Tsirkas *et al.*, 2003).

In the present research work, numerical analysis of the temperature field during laser welding-brazing of Mg/Ti has been carried out to help in the analysis of the phase evolution during the LWB process. A 3D FEM model has been used for the numerical solution. In the boundary condition, two modes (convection and radiation) of heat transfer have been considered. In addition, the reaction products at different regions of the brazed interface were analyzed.

2.7   Summary

As there is a desire in the high-technology based manufacturing sectors to join Mg/Ti in order to achieve lighter weight, versatile and tailored properties in one composite part, development of a reliable joining technology for joining Mg/Ti parts will expedite the application and use of both Ti and Mg alloys in these industries. The huge discrepensies in their physical properties and limited solubility imposed difficulties in joining them. At present, Mg/Ti sheets were welded by variety of joining techniques, including solid-state methods like friction stir welding (FSW), diffusion bonding, and ultrasonic welding and fusion based processes such as arc welding and laser beam welding.

The review of the literatures show that joining Mg/Ti by conventional fusion welding technologies has some shortcomings such as coarsening of the grains, voids and cracks formation, which lower the surface formability and significantly deteriorate joints performance. In addition, solid-state joining methods such as FSW and diffusion bonding have significant limitations and were not widely adopted by automotive and other mass production industries.

Therefore, in order to keep the Ti in the solid state and avoid evaporation of the Mg, the remaining option to join Mg to Ti will be the LWB technique using another element that has a substantial solubility with Ti and Mg and act as intermediate element or alloy. The formation of the IMCs would indicate that metallurgical bonding was achieved. However, generation of thick IMCs along the interface is not favorable due to degradation of joint mechanical performance. Laser beams with high precision and high-energy concentration can provide high welding speeds and high cooling rates. The resulting limited reaction time minimizes the thickness of the IMCs. Therefore, using a laser welding-brazing for joining Mg/Ti alloys would be a viable approach.

The effects of interlayer materials on joint performance has been the focus during dissimilar welding and this has resulted in a dearth of information concerning the influence of interlayers on intermetallic phase formation at dissimilar joint interface. For instance, it is not possible based on the published literature to determine whether a particular interlayer will improve the interfacial reactions and avoid the generation of thick IMCs at the interface, how it will do so, under what conditions it is best applied and what its overall effect will be on the joint mechanical properties (Maldonado-Zepeda, 2001).

Generally, the selection of suitable interlayer for joining Mg/Ti alloys largely depends on the interlayer composition that gives excellent wetting and bonding without

generating thick layers of IMCs at the joint interface (Atieh & Khan, 2014c). Ni and Cu are considered as the most widely used elements for improving weld properties such as strength, ductility and toughness (Amer *et al.*, 2010; Migiakis & Papadimitriou, 2009). Cu and Ni can react with Mg and Ti in terms of their binary phase diagrams, thus metallurgical bonding between AZ31B and Ti-6Al-4V may be realized, which may contribute to the enhancement of the joint performance. Furthermore, the Ni-Cu binary phase diagram belongs to an isomorphous system (100% liquid and solid solubility). Therefore, a reasonably homogeneous microstructure with excellent corrosion resistance can be expected (Yue *et al.*, 2010). Atieh et al. (2014c) observed that compared with using foils in which the foils thickness produced a large volume of thick IMCs, the electrodeposition of thin coats improved the joint strength.

Based on this considerations, in the present research electrodeposition of pure Ni and Cu layer was employed as the interlayer materials to join the immiscible Mg/Ti by laser welding-brazing technique. The influence of the interlayer on the interfacial reaction and joint performance were studied. Moreover, numerical analysis of the temperature field was performed to help in the analysis of the phase evolution during the LWB process. Based on the above analyses, the bonding mechanism was elucidated.

CHAPTER 3: MATERIALS AND METHODS

3.1   Introduction

This chapter detailed the materials adopted in this study, the samples preparation for welding and metallographic analysis, numerical analysis and characterization of the weld quality are presented.

Different metallurgical techniques were employed to investigate and analyze the microstructure developments of the welded samples such as optical microscopy (OM) and scanning electron microscopy (SEM). The elemental composition analysis was carried out using energy dispersive spectroscopy (EDS) and X-ray diffraction (XRD). In addition, numerical simulation of the welding temperature field distribution at different regions of the joint was carried out using finite element (FEM) MSC Marc software to help in the analyses of the reaction products evolution during LWB process.

Furthermore, the joint quality is estimated through hardness and tensile-shear testing. Generally, the hardness evaluations are used to measure the homogeneity of the joint region and the influence of new phase's formation on the joint characteristics, whereas, the tensile shear test, is used to correlate the relationship between the microstructural evolution and mechanical properties.

3.2   Materials

Commercially available AZ31B and Ti-6Al-4V with dimension of $100 \times 50 \times 1.5$ mm and $100 \times 50 \times 1$ mm, respectively were used in this study. The base materials dimensions were chosen based on previous study (Tan *et al.*, 2016a). In addition, commercially available AZ92D Mg based filler wire having a diameter of 3.5 mm was chosen for this work. Table 3.1 listed the compositions of these materials. Moreover, the physical and mechanical properties of these metals are presented in Table 3.2.

Table 3.1: Composition of the base and filler materials (wt%).

Alloy	Al	Zn	Mn	Fe	V	Si	Mg	Ti
AZ31B	2.5-3.5	0.5-1.5	0.2-0.5	0.005	---	0.1	94.395-96.695	---
Ti64	5.5-6.8	3.5-4.5	---	0.3	3.5-4.5	---	---	83.9-87.2
Filler Metal	8.3-9.7	1.7-2.3	0.15-0.5	0.005	---	0.05	87.445-89.795	---

Table 3.2: Physical and Mechanical properties of AZ31B and Ti64 (Atieh, 2013).

Properties		Ti64	AZ31B	
Mechanical	Hardness (HVN)	300-400	68	
	Yield Strength (MPa)	800-1100	203.7	
	Tensile Strength (MPa)	900-1200	271.2	
	Elongation (%)	13-16	13.2	
Physical	Crystalline Structure	BCC, HCP	HCP	
	Density (g/cm^2)	4.5	1.77	
	Electrical Resistivity ($\mu\Omega$m)	1.67	10	
	Coefficient of Thermal Expansion (10^{-6}K^{-1})	9	26	
	Thermal Conductivity (WM^{-1}K^{-1})	7	0.23	
	Melting Temperature (˚C)	1670	T solidus	T liquidus
			582	628

3.3 Experimental methods

The experimental methods are summarized in Figure 3.1. They include electro-deposition of interlayers, samples preparation, joining, metallographic examination and mechanical testing.
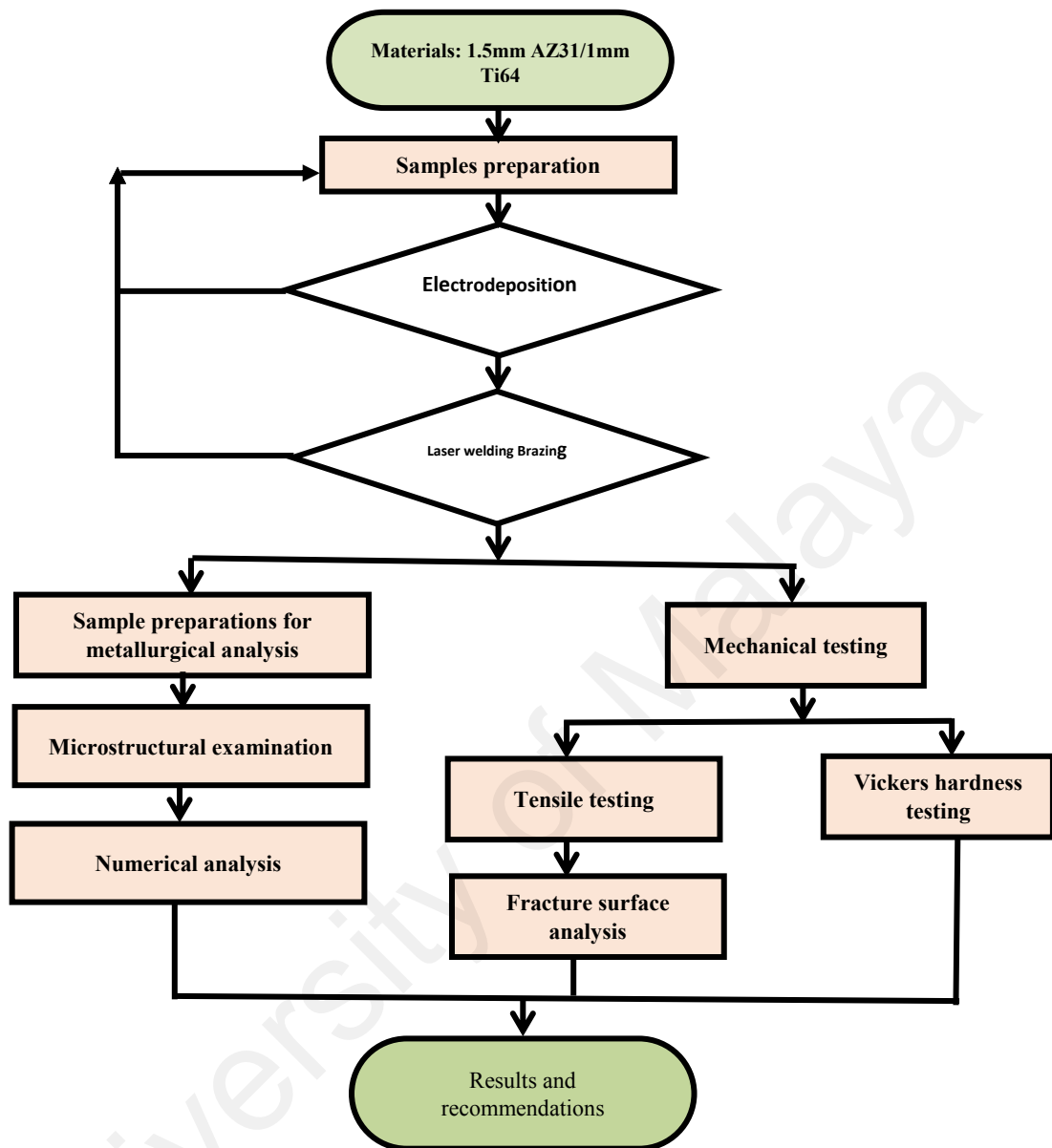
Figure 3.1: Flowchart of experimental methods.

3.3.1 Electrodeposition process

The electrodeposition of Cu and Ni metals layers on the Ti substrate was carried out based on the American Society for Metals (ASM) standard (Handbook, 1982). Prior to electrodeposition, a solution of an acid containing 15% hydrochloric acid, 5% hydrofluoric acid and 80% deionized water for 3 min was used to remove oxide film on

the Ti surfaces. The electroplating of the pure Cu and pure Ni on the Ti substrate was performed in a 500 mL beaker containing the plating solution shown in Table 3.3 and Table 3.4. Figure 3.2 shows the electrodeposition equipment and schematics of electro-plating process. Direct current (DC) power was used during the Cu and Ni electrodeposition process, with pH value of 5 at 35˚C. Furthermore, the current density and magnetic stirrer to agitate the bath were kept at 0.3 A/dm^2 and 200 rpm, respectively. The electro-plating time was used to control the coating thickness. For each coating condition, the average of at least five coating thickness were measured using SEM cross sectional micrograph. In addition, EDS mapping of the coating was carried out to ensure the defect free layer deposition on the Ti substrate.

Table 3.3: Cu electroplating solution compositions (wt%).

Composition	$K_4P_2O_7.3H_2O$	$C_6H_{17}N_3O_7$	$CuSO_4.5H_2O$	$Na_2HPO_4.12H_2O$
Amount (g/L)	220	20	48	24

Table 3.4: Ni electroplating solution compositions (wt%).

Composition	$NiSO_4.6H_2O$	NaCl	Na_2SO_4	H_3BO_3	$MgSO_4.7H_2O$
Amount (g/L)	180	10	70	30	60
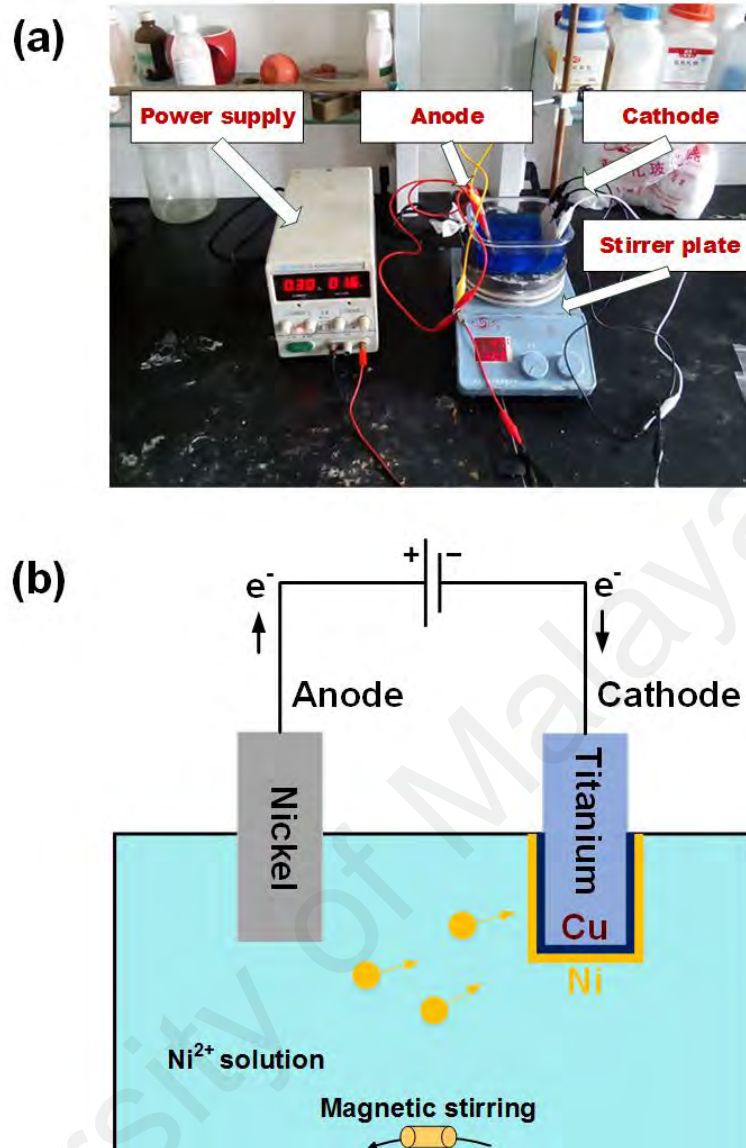
Figure 3.2: (a) Electrodeposition equipment set-up; and (b) Illustration of the Cu-Ni layer electro-plating process.

3.3.2   Laser welding-brazing (LWB) process

A 6-kW fiber laser (IPG-6000) with a beam parameter product of 8 mm/mrad and 1070 nm wavelength was used in this study. The Mg/Ti joint was prepared in a lap configuration with AZ31 situated above the Ti64 plate. The oxide layer on the Mg surface was removed with stainless steel wire brush prior to welding. The filler wire was cut into pieces and preset on the work-piece at the joint interface prior to heating and brazing as illustrated in Figure 3.3. The edge of the Mg was irradiated by vertical laser beam. The

beam was defocused in order to increase laser beam spot size and argon gas (99.99% purity) was used to shield the joint from oxidation. Table 3.5 shows the LWB process parameters optimized in this work. The experimental parameters were selected based on a preliminary results.
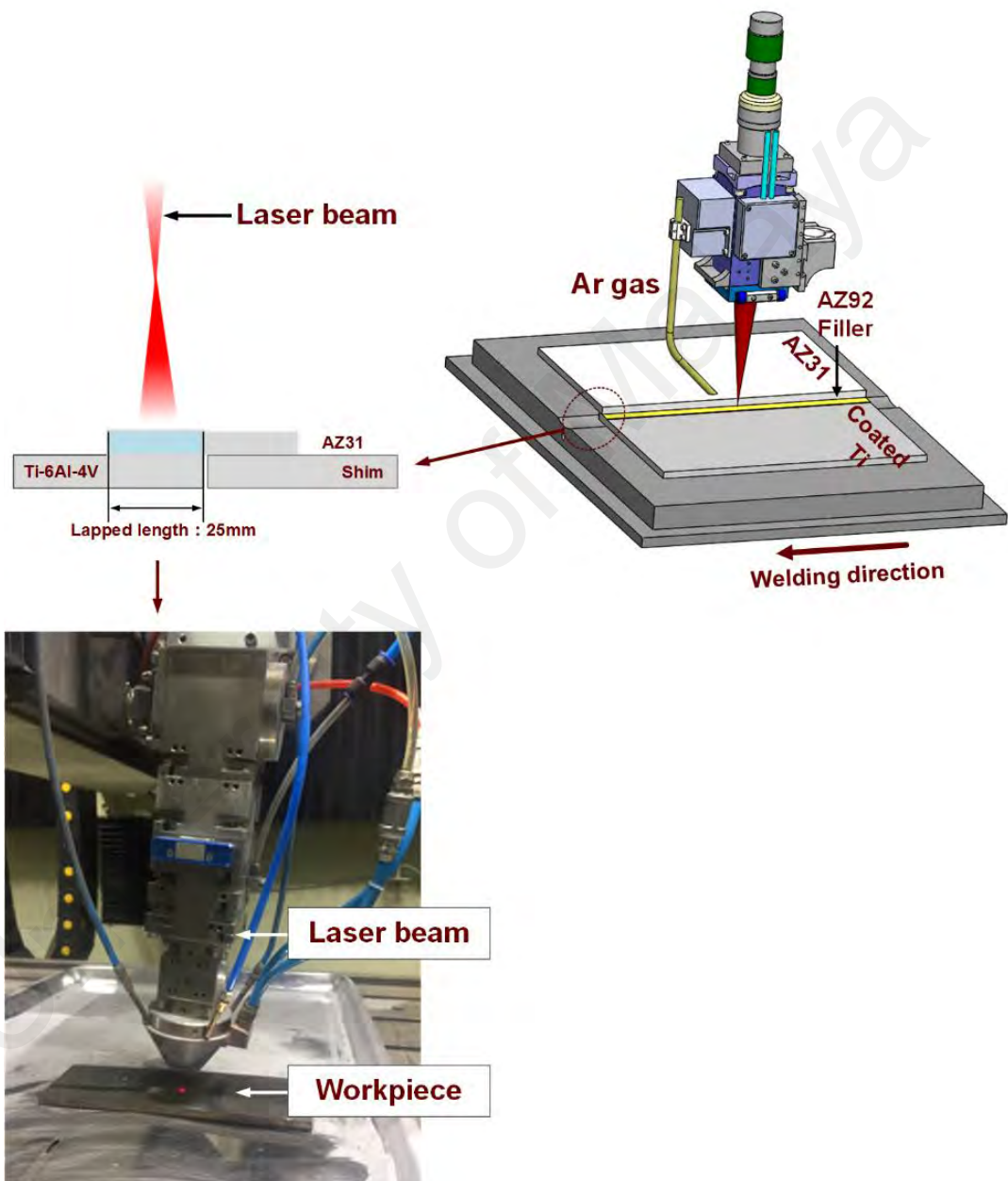
Figure 3.3: Illustrations of the laser welding-brazing experimental set up.

Table 3.5: Laser welding-brazing optimized parameters.

Laser output power (W)	1400
Defocus distance from Ti sheet (mm)	+30
Welding velocity (m/min)	0.3
Ar shielding gas flow rate (L/min)	20

3.3.3 Metallographic investigations

Standard procedures were adopted to prepare the metallographic specimens after welding (Standard, 2001). OLYMPUS-DSX510 Optical microscopy (OM) and Zeiss Merlin Compact SEM equipped with EDS were adopted to observe cross sectional microstructures morphologies and fracture surface. The reaction products formed were verified by XRD (Panalytical X'pert 3 Powder) using a copper target at 35 mA and 40 kV. The 2θ scans were carried out from 20° to 90°, at a step size of 0.04° and 1 second per step. The processing of the diffractograms was performed in the software package PDXL-2 and using ICDD PDF-2 databases.

3.3.4 Mechanical testing

3.3.4.1 Hardness test

Hardness profiles across the joint regions is proven as an effective technique for identifying the phases and microstructural changes along the weld zone under different joining conditions. Unlike the tensile test, the hardness measurement can give rough estimation of the mechanical characteristics of a particular phase that may arise within the bonding region. Hence, the welded samples was prepared for hardness measurements. Vickers' hardness tester was employed to quantify the variations in the hardness across the joint zone.

In view of the huge discrepancies in hardness value between the base materials, experimental trials were performed to determine appropriate load such that a distinct

indentation on the Ti64 is achieved and the indent be small enough to quantity the small phases' hardness values in the AZ31B. A value of 100 g and 10 s dwell time were used for all hardness measurements. The test was made according to the ASTM E384 standard (Kuhn & Medlin, 2000).

The Vickers' hardness (HV) is computed based on the surface area of the indent using Equation 3.1:

$$Hv = \frac{1.854P}{D^2} \qquad (3.1)$$

Where, P is the applied load and D is the average of the diagonals.

3.3.4.2 Tensile-shear test

For practical applications, the joining of AZ31 alloy to Ti-6Al-4V may be carried out using sheet metal. The common dissimilar joint strength testing for sheet metals is lap shear tests (Ziegelheim *et al.*, 2007). In addition, the shear-test causes failure, thus provide information on the failure type and failure location.

The samples for the tensile shear analysis was machined into 50 mm long and 10 mm wide in accordance with previous study (Tan *et al.*, 2016a). The lap shear tests was achieved using Instron 5967 tensile tester machine. To minimize induced couples or bending of the specimens, shims were added to each of the sample as illustrated on Figure 3.4. Room temperature tensile shear testing was performed at 1 mm/min crosshead-speed. The mechanical resistance of the joint was obtained through tensile shear testing of at least three samples.
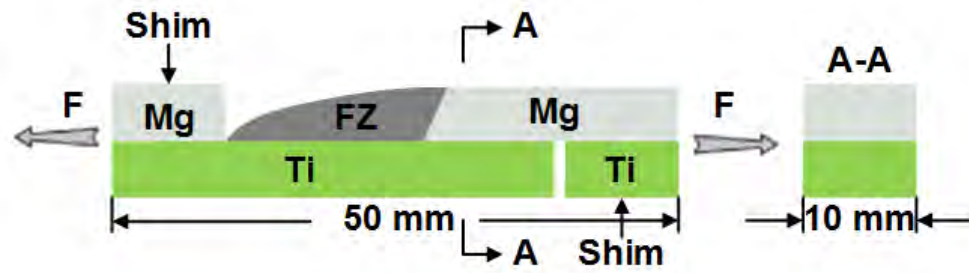
Figure 3.4: Illustration of tensile test specimen.

3.3.5 Temperature field numerical simulation

3.3.5.1 Mathematical description of the model

To obtain the temperature field distribution profiles of the joint at the interface, 3D heat conduction temperature field of laser welded-brazed Mg/Ti was established. The welding temperature field distribution at different regions of the joint was performed using FEM MSC Marc software. During the modelling process, the effect of the coating layer was neglected, considering that compared with thickness of the base metals the electrodeposited interlayer thickness was very small. In order to make the model a pragmatic one, the following key assumptions were made during the calculation:

1. Workpiece is moving in one direction at constant velocity, i.e., X-direction.

2. The effect of the shielding gas is neglected.

3. Half of the geometry is considered for the calculation.

4. Ambient temperature is set at 20°C.

5. All the materials properties are temperature dependent.

6. The materials used are isotropic.

7. Only considered the thermal conduction between the workpiece and the atmosphere and ignored the heat conduction of the fixture to the workpiece.

Under the assumptions, the 3D transient heat transfer steady-state equation is obtained:

$$\rho C_P \frac{\partial T}{\partial t} = \frac{\partial}{\partial x}(k\frac{\partial T}{\partial x}) + \frac{\partial}{\partial y}(k\frac{\partial T}{\partial y}) + \frac{\partial}{\partial z}(k\frac{\partial T}{\partial z}) + q_a \qquad (3.2)$$

Where, C_P specific heat capacity, k thermal conductivity, T is the temperature, q_a is the volumetric heat source within the laser's range of action.

3.3.5.2 Heat source model

In this work, a fiber laser was employed. During welding, the Mg based filler and part of Mg base metal melted by the laser irradiation, which wetted and spread on the surface of the Ti64 to form the welded joint. Thus, the welding was accomplished by conduction. As a result, Gaussian face function (Equation 3.3) was employed to describe the energy distribution (Chen *et al.*, 2011):

$$q_s(x,y) = \frac{\alpha Q_s}{\pi r_s^2} \exp(-\frac{\alpha(x^2 + y^2)}{r_s^2}) \qquad (3.3)$$

Where, Q_s=heat source power, r_s=effective radius, α=heat efficiency and q_s=linear energy.

3.3.5.3 Boundary condition

The Gaussian face function is used to consider convection and radiation heat losses. The convection heat transfer was characterized by the Newton's law of cooling, whereas, Stefan-Boltzmann's expression represented radiation heat loss. However, the laser heat source was at the top surface and the initial temperature was chosen to be 20˚C. Hence, the equation will be:

$$k\frac{\partial T}{\partial z} = -q_{cr} \qquad (3.4)$$

$$q_{cr} = \partial_{cr}(T - T_\infty) \qquad (3.5)$$

Where, q_{cr} is the heat flux density because of convection and radiation losses, ∂_{cr}

increased heat transfer coefficient，T_∞ is the ambient temperature.

3.3.5.4 Finite element model

The temperature field distribution induced was analyzed using 3D finite element model using MSC Marc software. The meshing patterns adopted is shown in Figure 3.5. In this study, a refined meshes were employed at the weld seam and heat affected regions, whereas, coarse meshes were made away from weld region as depicted in Figure 3.5 to ensure numerical precision and simplify the simulation process. Furthermore, the simulation was performed only for half of the geometry due to its symmetrical nature. The model validation was described in the results section.

3.3.5.5 Materials properties

The thermo-physical properties of the base metals such as thermal conductivity and specific heat changed with temperature. Therefore, to ensure the model precision, the main thermo-physical properties of Mg and Ti with temperature change were added into the MSC. Marc. Figure 3.6 shows the thermo-physical properties of the base metals adopted in this research.
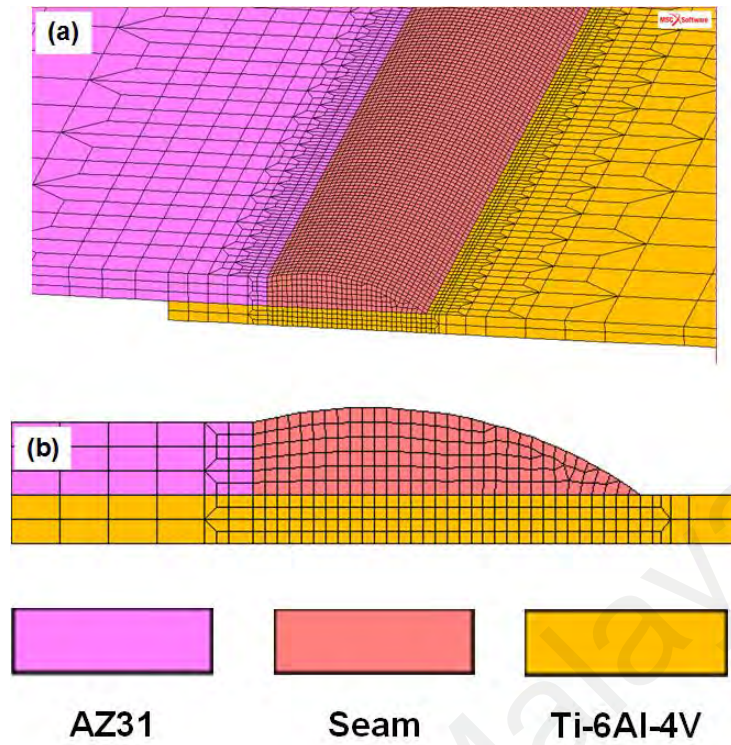
Figure 3.5: Computed meshes: (a) the grid; and (b) the cross-section.
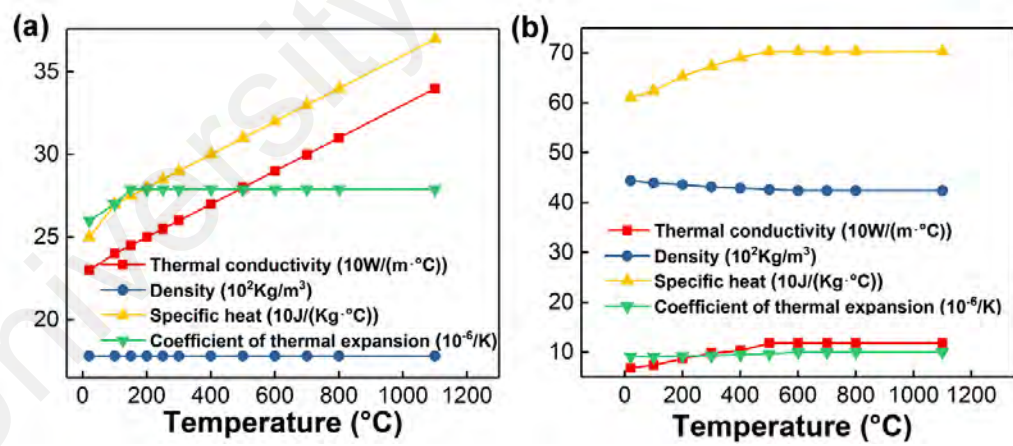
Figure 3.6: Materials properties of (a) AZ31; and (b) Ti64 (Zang *et al.*, 2018).

CHAPTER 4: RESULTS AND DISCUSSION

4.1 Influence of interlayer arrangements and heat input on joint formation

A fiber laser welding-brazing method has been developed for welding AZ31/Ti64 sheets in the lap joint configuration using electrodeposited Cu-Ni layer. The weld appearance, cross-sectional microstructure morphology and mechanical performance of the joints were examined using two interlayer arrangements; AZ31/Cu-Ni/Ti64 and AZ31/Ni-Cu/Ti64 at different heat input. Table 4.1 shows the laser welding-brazing parameters adopted. The experimental parameters were carefully chosen based on preliminary results. Moreover, numerical analysis was performed to examine the phase evolution during the LWB process. The bonding mechanism was also discussed.

Table 4.1: Laser welding-brazing parameters used in this experiment.

Laser output power, P (W)	1000, 1200, 1400, 1600, 1800, 2000, 2200
Defocus distance from Ti sheet (mm)	+30
Welding velocity (m/min)	0.3
Ar shielding gas flow rate (L/min)	20

4.1.1 Electrodeposition of Cu and Ni layer

The electroplating of the pure copper and nickel followed a sequence of Cu and finally Ni on the Ti substrate (Cu-Ni) were performed in a 500 mL beaker containing the plating solution shown in Table 3.3 and Table 3.4. In order to get a 10 µm thick uniform Ni and Cu layer on the Ti substrate, different electrodeposition durations and current densities were attempted. When the electroplating was performed at current density of 0.3 A/dm^2 for 10 min, an approximate 5.38 ± 0.10 µm Cu and 5.03 ± 0.30 µm Ni coating layer on the Ti substrate was achieved. Figure 4.1 shows the cross sectional view and energy-

dispersive EDS mapping of the Cu-Ni layer. Similarly, the effect of the layer arrangement on the joint quality was also investigated using the above electrodeposition procedure with a sequence of Ni and finally Cu (Ni-Cu) on the Ti substrate. The corresponding SEM cross-sectional view and EDS mapping of the coating layer on the Ti substrate are shown on Figure 4.2. The coatings were of relatively uniform with a void free interface.
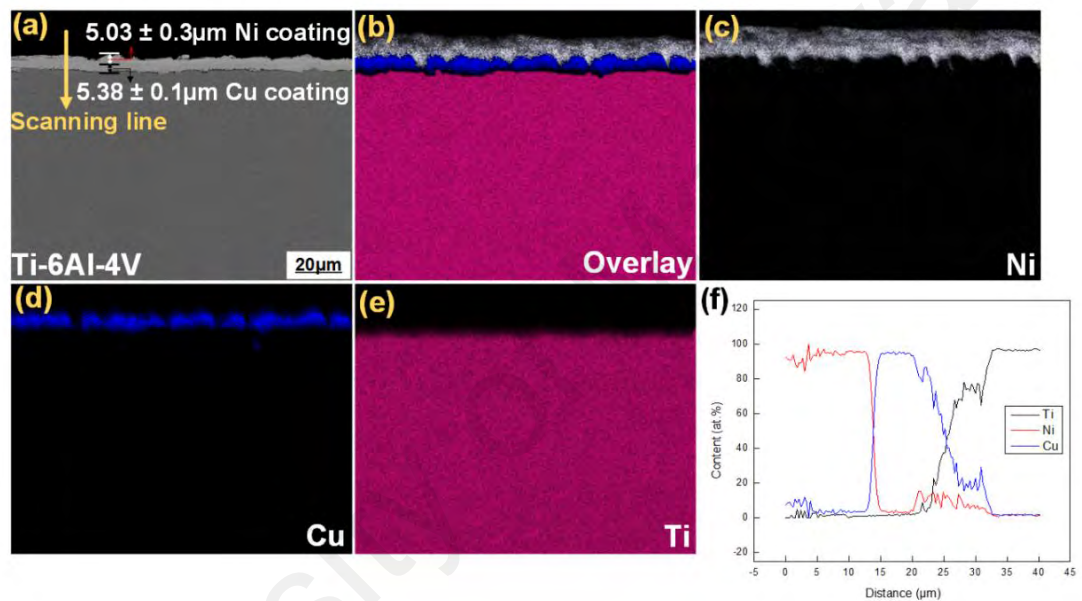
Figure 4.1: SEM cross-sectional view and EDS mapping of Cu-Ni: (a) corresponding image; (b) Overlay image, (c)-(e) Ni, Cu, and Ti; (f) line scanning results.
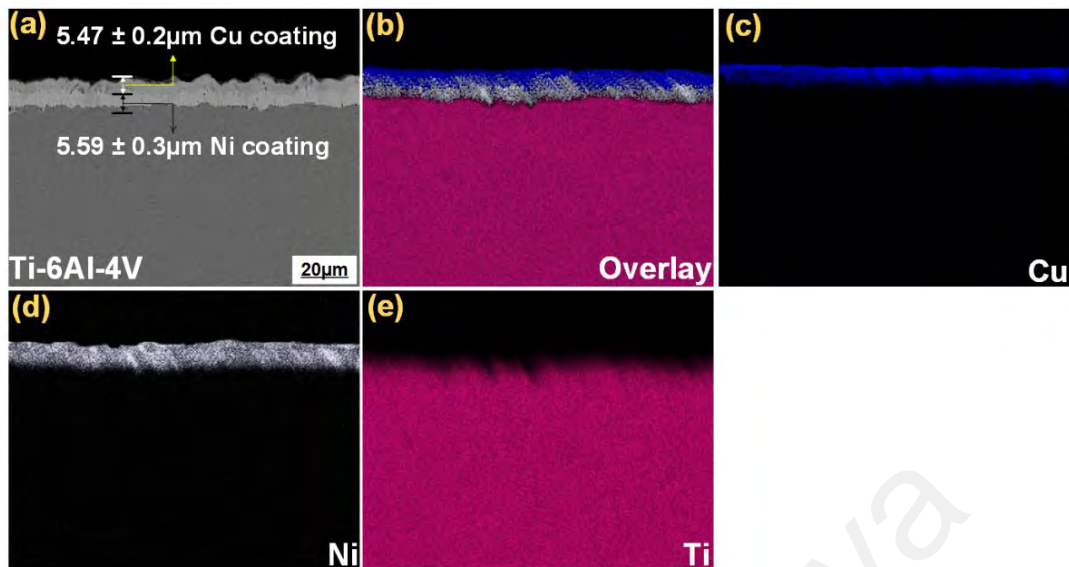
Figure 4.2: SEM cross-sectional view and EDS mapping analysis of Ni-Cu: (a) corresponding image; (b) Overlay image, (c)-(e) Cu, Ni, and Ti.

4.1.2 Weld appearance and cross-sections

The heat input and weld quality are directly influence by laser power (Li *et al.*, 2018). Therefore, to produce high quality interfacial layers, it is essential to maintain a reasonable control of heat input during the LBW process. A typical appearance and cross section of the joints at different laser power are shown in Figure 4.3. In both cases, smooth weld surface was observed even when the laser output power was low (1000 W), indicating that the filler wire required low heat input to melt. Nevertheless, an incomplete brazing between the liquid filler and Ti64 was formed (Figure 4.3a). The incomplete brazing could be associated with the size of the laser beam spot (2.4 mm) at the defocused distance was lower than the diameter of the filler wire diameter (3.5 mm). Hence, most of the energy was used to melt the filler wire, which resulted in insufficient pre-heating of the Ti64 sheet. Increasing the laser power from 1200-1600 W improved the wetting of brazing alloy on the Ti64. However, increasing the laser power beyond 1600 W decreased the seam width (Figure 4.3c), due to evaporation of Mg fusion zone (FZ).

In order to demonstrate the wettability of molten filler on Ti64 surface in both processing conditions, the variation in seam width and contact angle with laser power were analyzed as displayed in Figure 4.4. When the laser output power was 1000 W (Figure 4.4a), the contact angle of 47.26° was formed for AZ31/Ni-Cu/Ti64 compared to 38.6° for AZ31/Cu-Ni/Ti64. The contact angle reduced to 15.2° in the AZ31/Cu-Ni/Ti64 compared to 16.9° for AZ31/Ni-Cu/Ti64 with further increased in laser power. In contrast, the seam width of AZ31/Ni-Cu/Ti64 increased from 7.09 mm to 7.50 mm when the laser output power raised from 1200 to 1400 W. Nevertheless, further increase in laser output power resulted in the decrease in the seam width to 7.0 mm. Similarly, for AZ31/Cu-Ni/Ti64, seam width increased from 7.13 mm to 7.40 mm and then declined to 7.16 mm. This observation could be attributed to the amount of heat input. The results showed that optimum heat-input facilitated the wettability of the brazing alloy, whereas, high heat-input resulted in severe evaporation. Similar phenomenon was reported for Mg/steel joint (Li *et al.*, 2013). Moreover, this study showed the ability of AZ31/Ni-Cu/Ti64 joints to lower the contact angle and promote the spreading of filler compared to AZ31/Cu-Ni/Ti64.
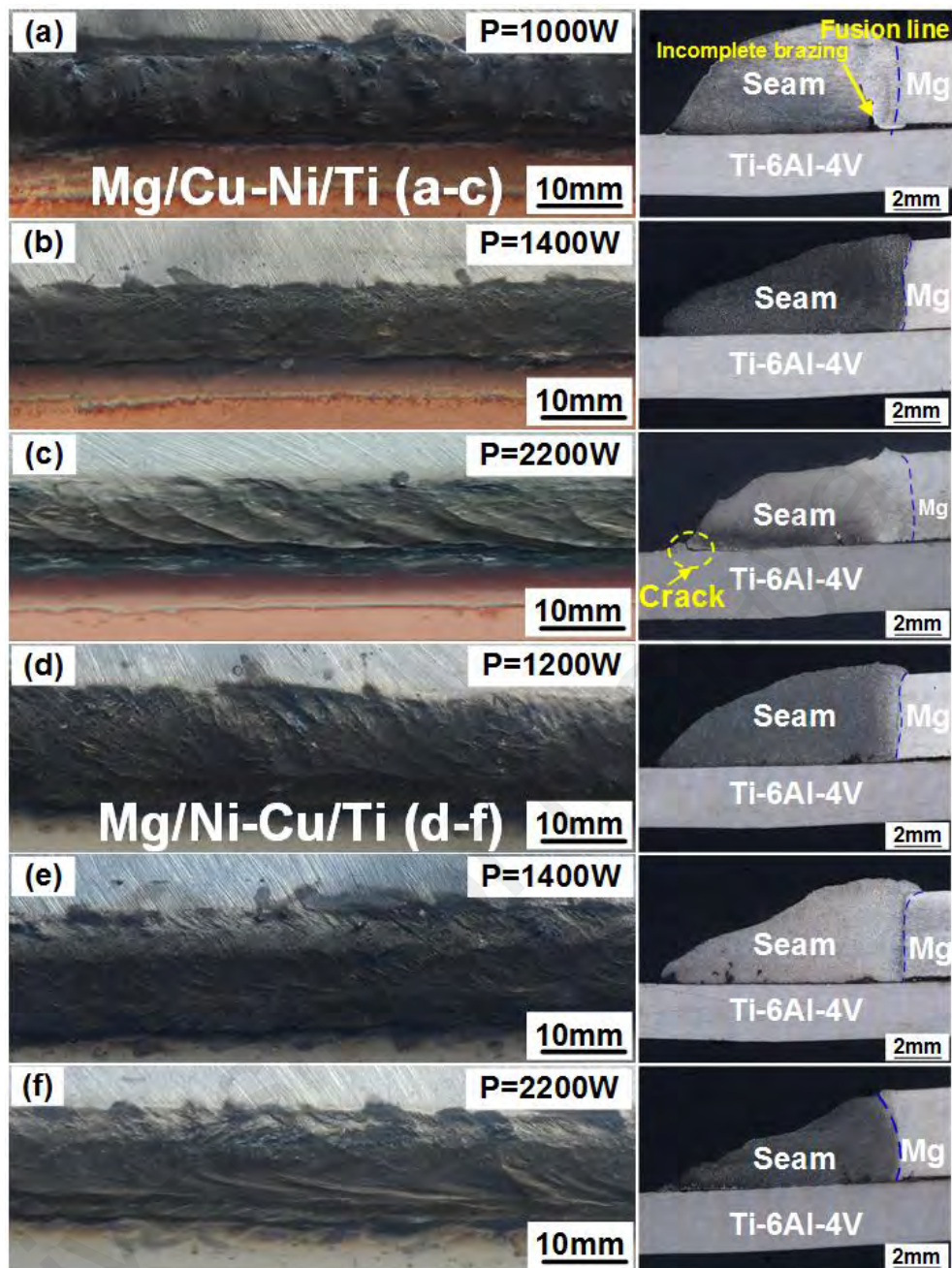
Figure 4.3: Laser welded-brazed Mg/Ti bead appearance and cross-sections: (a)-(c) AZ31/Cu-Ni/Ti64 and (d)-(f) AZ31/Ni-Cu/Ti64.
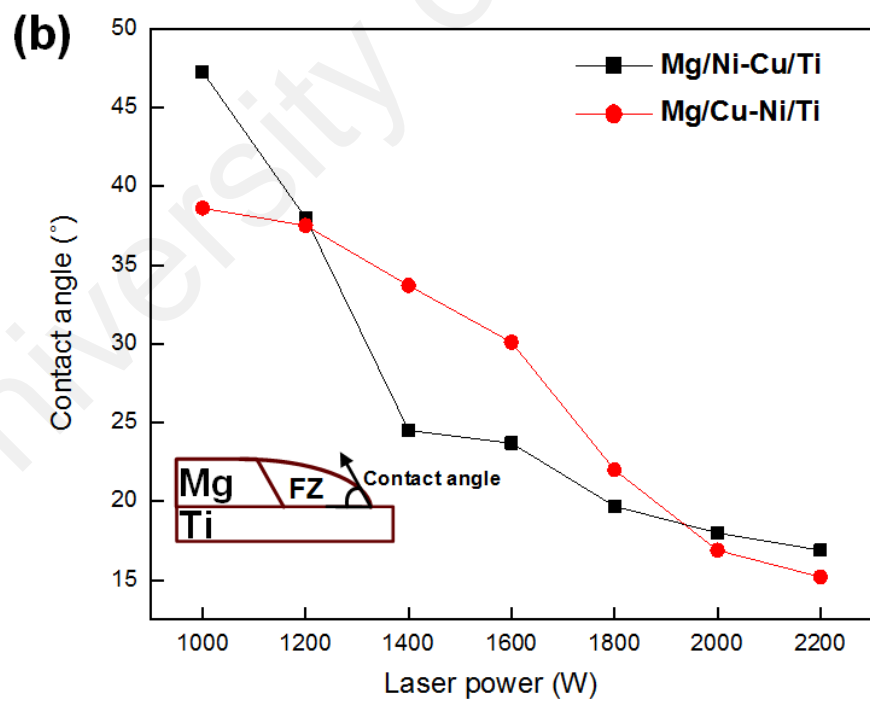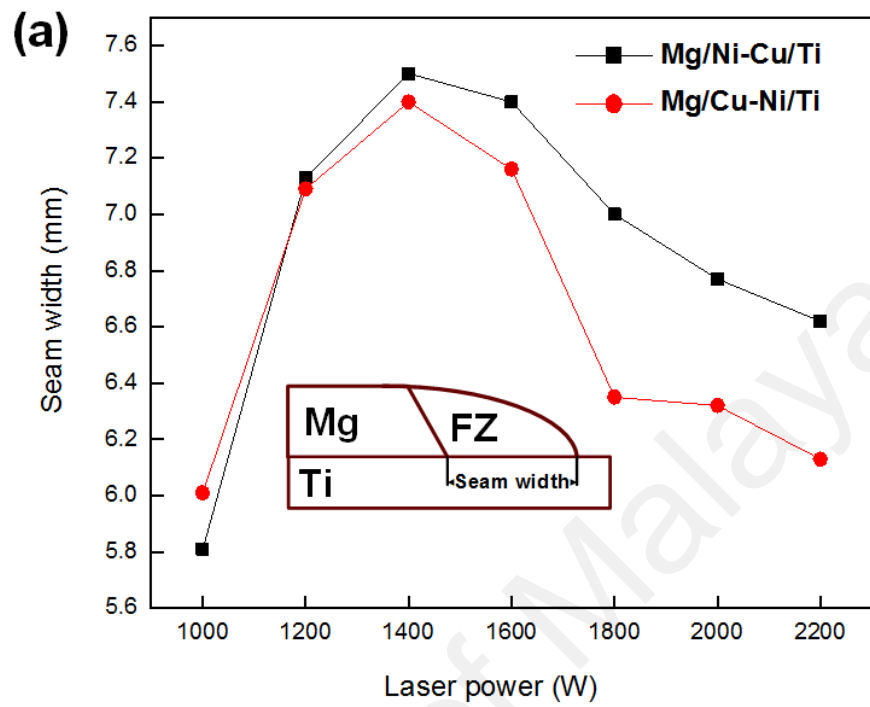
Figure 4.4: Variation in (a) seam widths and (b) contact angles with different coating arrangements.

4.1.3 Interfacial microstructure development and composition analysis

The interfacial microstructural evolution is greatly influenced by the heat input. Figures 4.5 and 4.7 show a typical cross sectional microstructure morphologies of AZ31/Ni-Cu/Ti64 and AZ31/Cu-Ni/Ti64 joints prepared at 1000, 1400 and 2200 W, respectively. The high temperature gradient during LWB process caused the interfacial microstructure along the interface to vary (Tan *et al.*, 2016c). Thus, the interface was divided into laser irradiation, middle and weld toe regions.

4.1.3.1 AZ31/Ni-Cu/Ti64 joints

Figures 4.5(a)-(c) show the cross sectional microstructure morphologies of AZ31/Ni-Cu/Ti64 prepared at 1000 W and the relevant EDS analysis is shown in Table 4.2. At the FZ, the EDS analysis showed that the dark phase (Point P1 in Figure 4.5a) consisted of 97.51 at.% Mg and 1.69 at.% Al, suggesting it was α-Mg. Meanwhile, the secondary phases (P2 in Figure 4.5a) far from the interface consisted of 10.74 at.% Al and 88.11 at.% Mg, which was verified as $Mg_{17}Al_{12}$. This precipitated phase was produced during the eutectic reaction, which was also reported during TIG welded Mg-Ti (Xu *et al.*, 2016). Moreover, a great number of dendritic structures (P3 in Figure 4.5a) dispersed around the α-Mg solid-solution matrix, having lamellar morphology were also observed nearby FZ-Ti brazed interface. Under the action of flow and vortex, a large amount of Cu coating was dissolved into the liquid filler and reacted with Mg. These dendritic phases consisted of 8.84 at.% Al, 80.92 at.% Mg, 0.09 at.% Ti, 0.55 at.% Ni and 9.60 at.% Cu. Based on previous study (Zhang *et al.*, 2018c), these phases were confirmed as Mg-Cu eutectic structure (α-Mg+Mg_2Cu). Eutectic reaction took place at 485°C: liquid ↔ Mg + Mg_2Cu. The Mg-Cu eutectic structure was also observed while joining Mg/steel using copper interlayer (Wang *et al.*, 2016). Besides, some bulk phases (P4 in Figure 4.5a) were observed adjacent to the FZ-Ti brazed interface. This phase was characterized as Mg-Al-Ni phase as it contained mainly 18.91 at.% Al, 42.64 at.% Mg, 30.65 at.% Ni and 7.48

at.% Cu, in accordance with Mg-Al-Ni phase diagram (Tan *et al.*, 2017b). The formation of this bulk phase could be associated with melting and diffusion of Ni coating into the FZ. On the other hand, no apparent IMC was produced at both direct irradiation and middle regions in Figure 4.5(a) and (b). EDS line scanning results (Figure 4.6a) across the direct irradiation region showed that the Ti content increased and Mg decreased with an apparent segregation of Al at the brazed interface. According to the atoms ratios in Figure 4.6(a), the Ti-Al IMC was identified as Ti_3Al. The thickness of this reaction layer was 6.80 μm. In contrast, there was no Cu observed at the interface, signifying that the Cu coating melted completely and dissolved inside the FZ. At low heat input, some un-melted Ni coating (P6 in Figure 4.5b) was observed at the middle region. At the weld toe region, thin IMC (P7 in Figure 4.5c) was produced. This layer consisted of 21.62 at.% Al, 68.13 at.% Ti, and 6.76 at.% Ni, which was characterized as Ti_3Al phase (Zhang *et al.*, 2018b).

Further increase in the laser power to 1400 W (see Figure 4.5(d-f)) and 2200 W (Figure 4.5(g-i)), more $Mg_{17}Al_{12}$ secondary phase was precipitated and less Mg-Cu eutectic phase adhering to the brazed interface were observed. Furthermore, smaller size and wider dispersal of Mg-Al-Ni phase in the entire fusion zone as observed at point P10 in Figure 4.5(d). This could be associated with Al, Cu and Ni atoms diffusing to a large area with increasing heat input. On the other hand, light gray (P8 in Figure 4.5d) and dark gray (P9 in Figure 4.5d) mixed IMC formed at the interface. The light gray layer consisted of 31.30 at.% Al, 46.81 at.% Ti, 16.82 at.% Ni and 4.14 at.% Cu, which was identified as Ti_2Ni IMC, whereas, the dark gray layer contained 22.72 at.% Al, 68.78 at.% Ti, 7.12 at.% Ni and 2.25 at.% Cu, suggesting it was Ti_3Al according to Ti-Al binary diagram (Witusiewicz *et al.*, 2008). The formation temperatures of Ti_3Al and Ti_2Ni were 1180˚C and 984˚C, respectively, suggesting that the formation of Ti_2Ni required 1 at.% Ni while that of Ti_3Al was 12 at.% Al. Thus, more Al atoms concentrated at the interface and some

Ti$_3$Al IMCs were formed at 1180°C. On the other hand, Ni atoms dispersed around Ti$_3$Al phase with a lower aggregation than that of Al atoms. However, owing to the only 1 at.% Ni demanded, some Ti$_2$Ni phases were formed around the Ti$_3$Al.

The corresponding EDS line scan conducted across the direct irradiation regions of the 1000 W, 1400 W and 2200 W prepared joints are shown in Figure 4.6(a to c). Although, all the three joints exhibited similar EDS trends, the thickness of the intermetallic grew from 6.80 µm to 51.51 µm when the heat-input increased. This suggested that thickness of the Ti-Al and Ti-Ni mixed reaction layer increased with heat input. Furthermore, small Cu concentration at the brazed interface in Figure 4.6(b) was associated with existence of the Mg-Cu eutectic structure, which adhered to the FZ-Ti brazed interface.
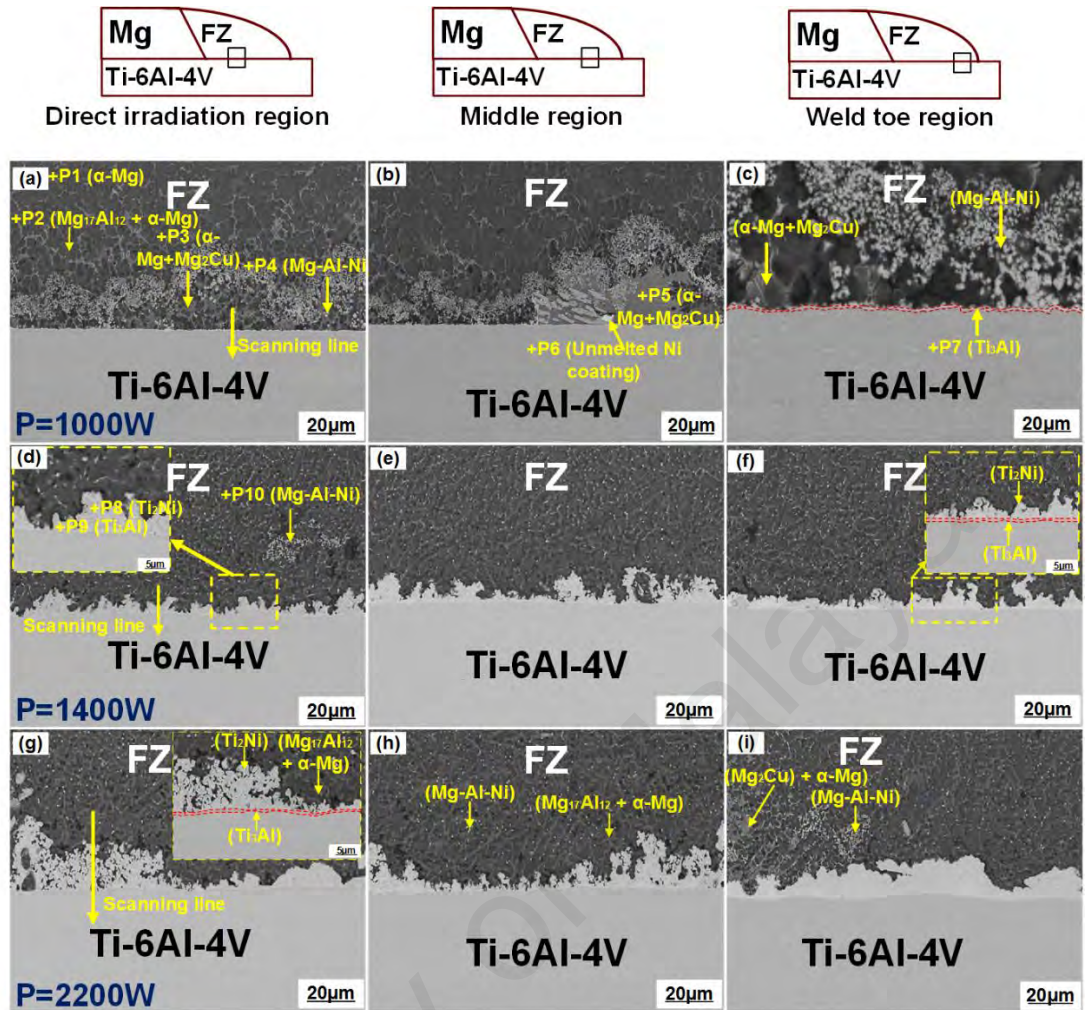
Figure 4.5: Microstructure of AZ31/Ni-Cu/Ti64 at different heat input: (a)-(c) 1000 W; (d)-(f) 1400 W and (g)-(i) 2200 W.

Table 4.2: EDS result of various points presented in Figure 4.5 (at.%).

Point	Mg	Al	Ti	Ni	Cu	Possible phases
P1	97.51	1.69	0.07	0.38	0.35	α-Mg
P2	88.11	10.74	0.07	0.14	0.94	$Mg_{17}Al_{12}$ + α-Mg
P3	80.92	8.84	0.09	0.55	9.60	α-Mg + Mg_2Cu
P4	42.64	18.91	0.31	30.65	7.49	Mg-Al-Ni
P5	84.49	0.13	0.13	2.49	12.76	α-Mg + Mg_2Cu
P6	2.38	---	0.91	95.39	1.32	Un-melted Ni coating
P7	1.10	21.62	68.13	6.76	2.39	Ti_3Al
P8	0.52	31.30	46.81	16.82	4.55	Ti_2Ni
P9	---	22.72	68.58	5.12	3.58	Ti_3Al
P10	31.60	42.62	0.83	19.69	5.26	Mg-Al-Ni
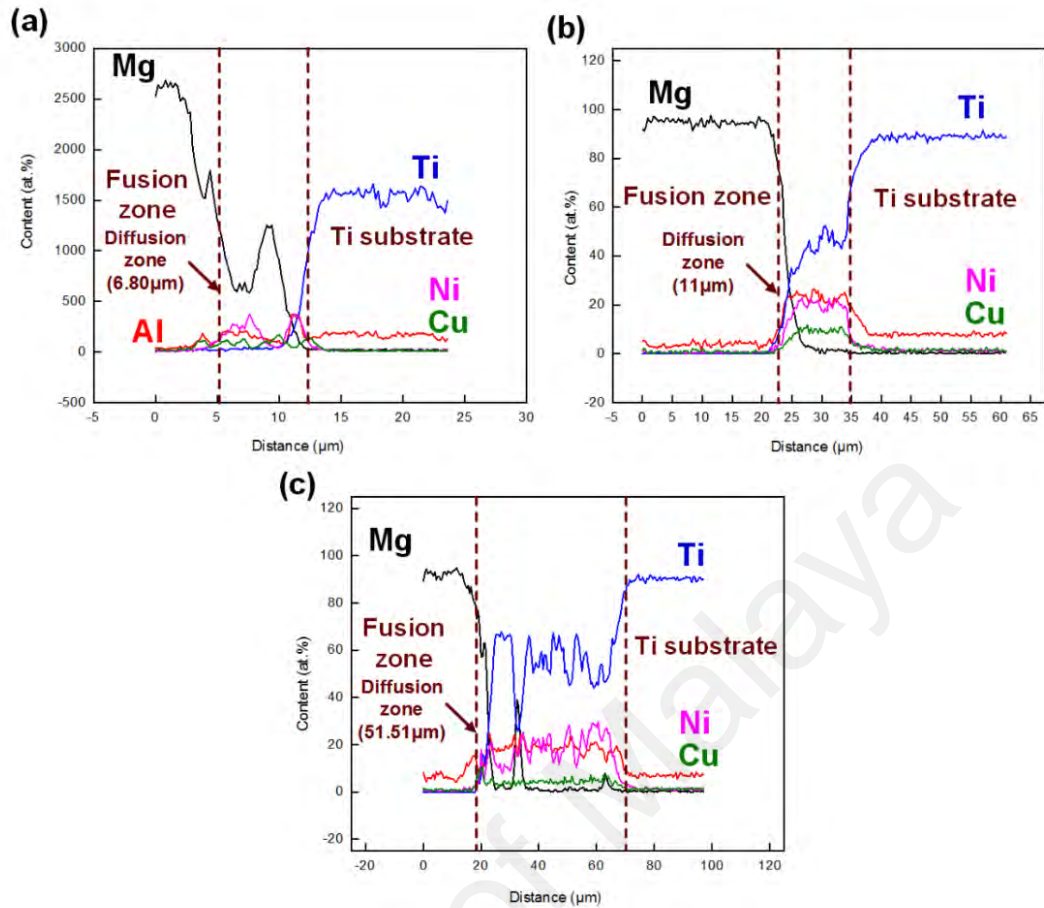
Figure 4.6: AZ31/Ni-Cu/Ti64 line scanning results at direct irradiation zone: (a) 1000 W, (b) 1400 W, and (c) 2200 W.

4.1.3.2 AZ31/Cu-Ni/Ti64 joints

Figures 4.7(a)-(c) show the SEM cross sectional microstructure morphologies AZ31/Cu-Ni/Ti64 joint prepared at 1000 W. The relevant EDS analysis is shown in Table 4.3. It was found that an IMC was formed at direct irradiation area in Figure 4.7(a). This layer consisted of light gray (Point P4 in Figure 4.7a) and dark gray (P5 in Figure 4.7a) phases. According to the EDS analyses, the light gray phase contained 23.17 at.% Al, 49.76 at.% Ti, 24.77 at.% Ni and 1.88 at.% Cu, which was identified as Ti_2Ni IMC, whereas, the dark gray phase observed below the light gray phase consisted of 21.62 at.% Al, 68.97 at.% Ti, 7.23 at.% Ni and 2.18 at.% Cu, suggesting it was Ti_3Al in accordance with Ti-Al binary diagram (Witusiewicz *et al.*, 2008). The diffusion of Al and Ni atoms

to the Ti substrate resulted in the formation of this mingled IMC layer. EDS line scanning

was performed across the direct irradiation region and the result is shown in Figure 4.8(a).

It was found that the Ti content increased and Mg decreased with an apparent segregation

of Ni and Al at the brazed interface, signifying the Ti-Ni and Ti-Al IMCs formation.

Furthermore, no Cu segregation was noted, indicating that under the action of flow and

vortex, the Cu layer dissolved into the liquid filler and participated in the microstructure

development. Zhang et al. (2018c) demonstrated that Cu could promote Al and Ti atoms

diffusion. Thus, continuous Ti_3Al IMCs evolved across the brazed interface. In other

words, the Cu coating played an inhabitation effect. According to the EDS analyses, the

dark phase (P1 in Figure 4.7a) mainly contained 92.51 at.% Mg and 6.69 at.% Al,

indicating that the dark phase was α-Mg. A great number of lamellar shape microstructure

(P2 in Figure 4.7a) was formed adjacent to the Ti substrate. The lamellar shape

microstructure consisted of 10.79 at.% Al, 80.84 at.% Al and 8.05 at.% Cu. In agreement

with previous work (Zhang *et al.*, 2018b), point P2 was identified as Mg-Cu eutectic

structure (α-Mg + Mg_2Cu). In addition, the formation of Mg-Cu eutectic structure was

also reported by Tan et al. (2015) while welding of Mg/Cu. Besides the lamellar structure,

a number of bulk phases (P3 in Figure 4.7a) were found to concentrate close the brazed

interface. This phase was characterized as Mg-Al-Ni phase as it contained 44.08 at.% Al,

21.06 at.% Mg, 32.90 at. % Ni, 1.74 at.% Cu (Tan *et al.*, 2017b). The formation of this

bulk phase could be associated with melting and diffusion of Ni coating into the FZ, which

reacted with Mg and Al atoms. Similarly a great number of Mg-Cu and Mg-Al-Ni were

observed at both middle and weld toe regions nearby the braze interface as presented in

Figures 4.7(b) and (c). The formation of these phases at low heat input could be associated

with flow and vortex generated in the molten pool, which resulted in large amount of the

Ni and Cu dissolved into the FZ and induced reaction with Mg. A large amount of un-

melted Ni coating (P6 in Figure 4.7b) was also observed at the middle region at low heat

input. Generally, Cu has a low absorptivity to laser beam. Therefore, when Cu layer was on top of Ni (as in the Cu-Ni layer arrangement) at low heat input most of the laser beam energy would be reflected leaving only small amount of energy to irradiate the joint, thus explaining the large amount of un-melted Ni coating observed. In addition, a thin interfacial reaction layer (P7 in Figure 4.7c) was produced at the weld toe region and from the EDS analysis, this phase confirmed as Ti_3Al.

Figures 4.7(d-f) and (g-i) show the SEM micrograph of the Mg/Cu-Ni/Ti joints produced at 1400 W and 2200 W, respectively. As the heat input increased, a great number of secondary phases (P9 in Figure 4.7e) consisting of 13.74 at.% Al and 85.68 at.% Mg believed to be $Mg_{17}Al_{12}$, was precipitated in the entire α-Mg solid-solution. This phase was produced during eutectic reaction (Xu et al., 2016). However, less Mg-Cu eutectic phase coupled with reduction in size and dispersal of Mg-Al-Ni ternary in the entire FZ was detected (Figure 4.7f). At the brazed interface, Ti_2Ni and Ti_3Al mixed reaction layer was produced, similar to that of joint produced in 1000 W. To further identify the concentration of element at the brazed interface of the direct irradiation area, EDS line scanning was performed as presented in Figure 4.8(b) and (c). Diffusion zone increased with increasing heat input reaching a maximum of 28.31 μm as shown in Figure 4.8(c). Along the brazed interface, concentration of Al and Ni were observed, suggesting possible formation of Ti-Ni and Ti-Al IMCs. Furthermore, no Cu segregation was noted owing to the dissolution Cu layer inside the FZ. The small Cu segregation at the interface in Figure 4.8(c) was associated with the existence of Mg-Cu, which adhered to the interface. At the weld toe region, an obvious crack was formed when the laser power was 2200 W, as shown in Figure 4.7(i), due to severe evaporation of FZ at excessive laser power and the formation of un-even phase (P11 in Figure 4.7i) identified as Al_2Ti according to EDS analysis. The formation of un-even Al_2Ti IMC at the weld toe region may give rise to stress concentration because of the huge discrepancies in Mg/Ti thermal expansion

coefficient and thermal conductivity, which could affect the joint mechanical performance and resulted in interfacial failure.

According to the result presented above, both AZ31/Ni-Cu/Ti64 and AZ31/Cu-Ni/Ti64 joints have similar interfacial reaction products at optimum heat input (1400 W). Therefore, to further verify the reaction products produced, XRD investigation of the AZ31/Cu-Ni/Ti64 joint was carried out. The XRD analysis shown in Figure 4.9 confirmed that the diffraction peaks of Ti_3Al, Ti_2Ni, and Mg_2Cu phases were detected, and this was in accordance with the EDS results presented in Table 4.3.
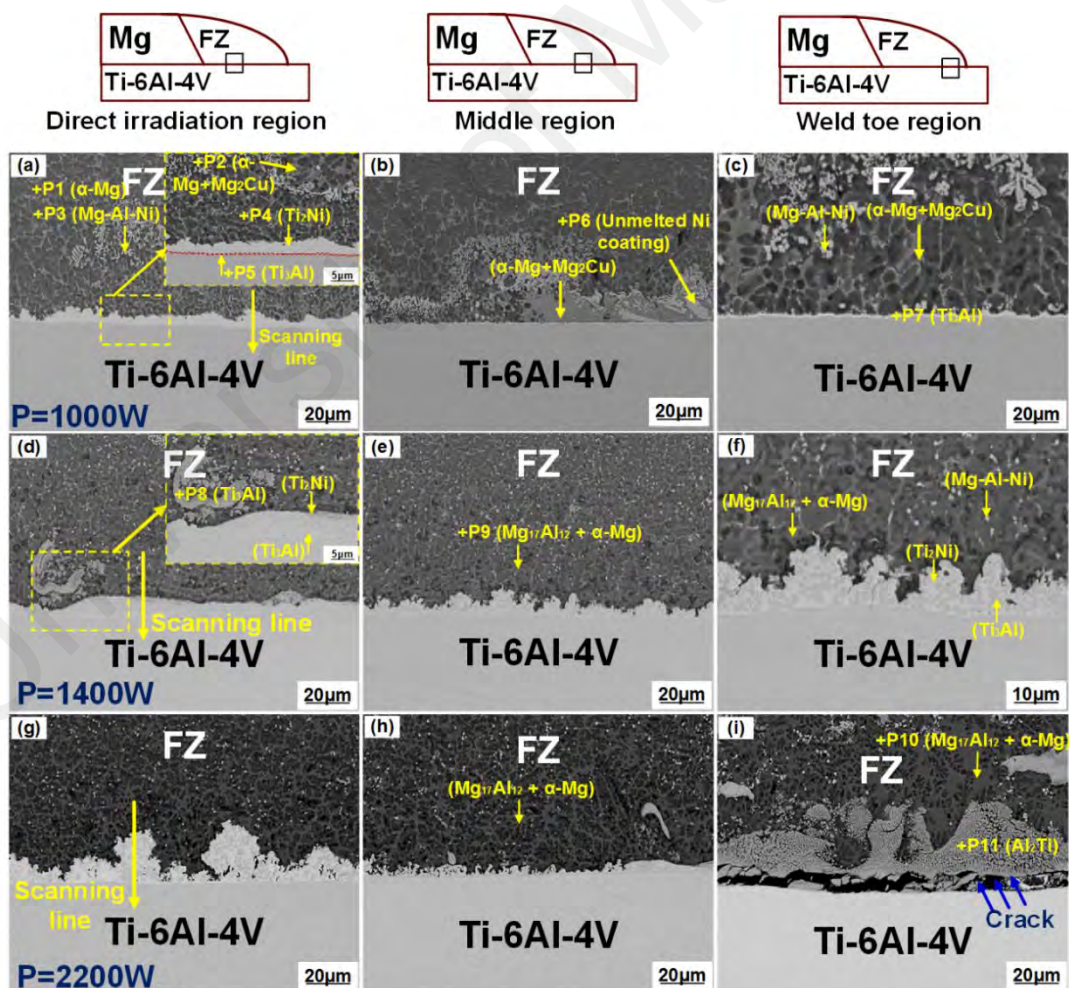
Figure 4.7: Microstructure of AZ31/Cu-Ni/Ti64 at different heat input: (a)-(c) 1000 W; (d)-(f) 1400 W and (g)-(i) 2200 W.

Table 4.3: EDS results of various points presented in Figure 4.7 (at.%).

Point	Mg	Al	Ti	Ni	Cu	Possible phases
P1	93.06	6.31	0.06	0.14	0.43	α-Mg
P2	80.84	10.79	0.07	0.25	8.05	α-Mg + Mg$_2$Cu
P3	21.06	44.08	0.22	32.90	1.74	Mg-Al-Ni
P4	0.49	23.17	49.76	24.77	1.81	Ti$_2$Ni
P5	---	21.62	68.97	7.23	2.18	Ti$_3$Al
P6	0.55	---	0.39	97.32	1.74	Un-melted Ni coating
P7	1.10	29.62	62.13	4.16	2.99	Ti$_3$Al
P8	0.43	21.08	71.18	6.23	1.08	Ti$_3$Al
P9	85.68	13.74	0.08	0.21	0.29	Mg$_{17}$Al$_{12}$ + α-Mg
P10	65.58	32.75	0.11	0.17	1.39	Mg$_{17}$Al$_{12}$ + α-Mg
P11	5.05	58.97	31.83	3.27	0.88	Al$_2$Ti
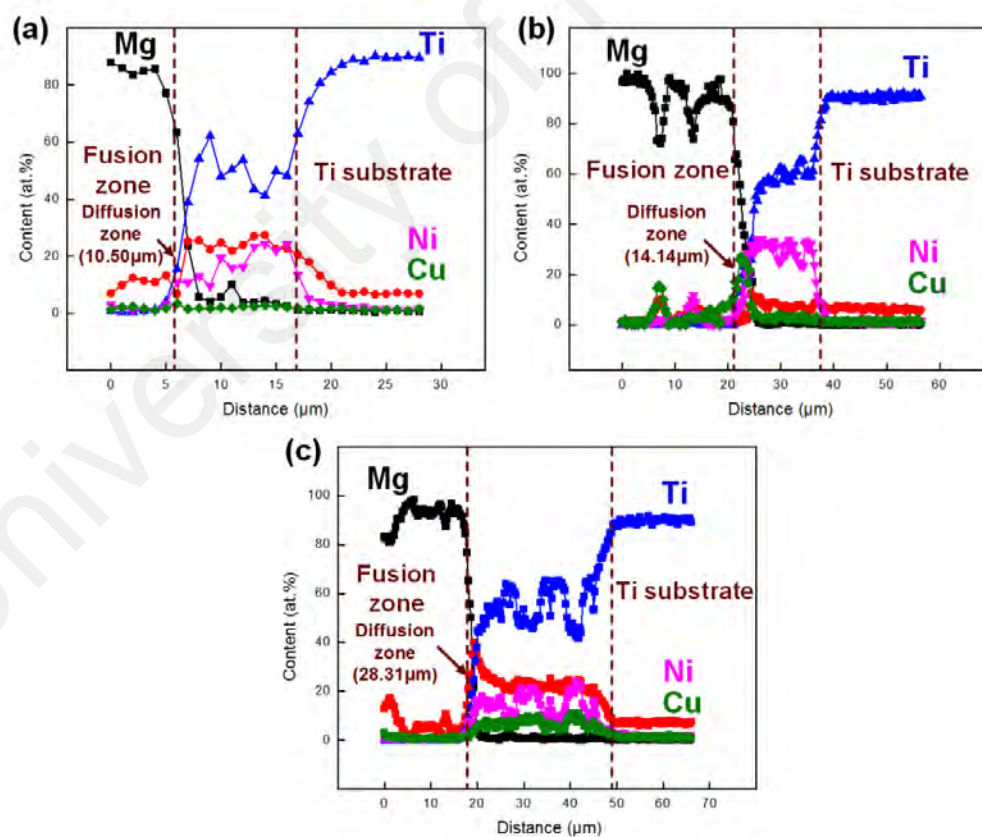
Figure 4.8: AZ31/Cu-Ni/Ti64 line scanning results at direct irradiation zone: (a) 1000 W, (b) 1400 W, and (c) 2200 W.
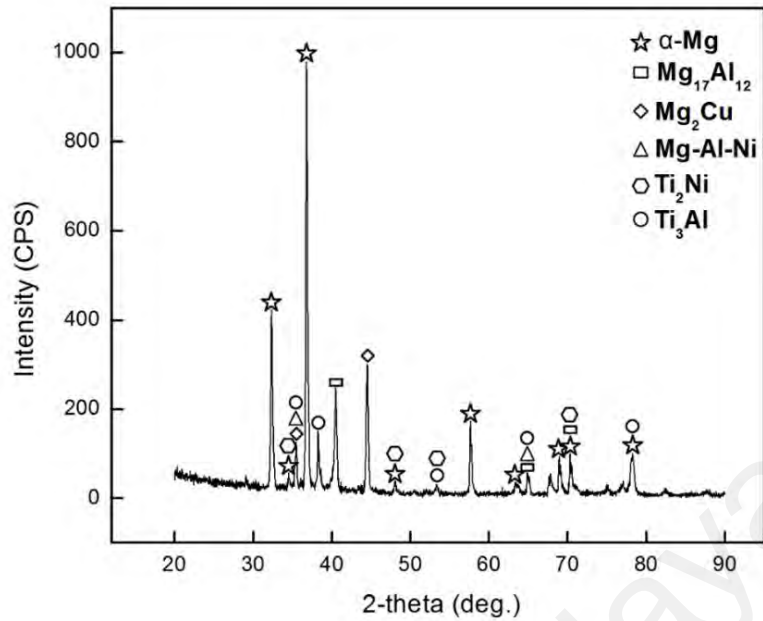
Figure 4.9: XRD result of AZ31/Cu-Ni/Ti64 joint at 1400 W.

4.1.4 Numerical analysis

MSC Marc was used to simulate the thermal cycles across the Mg/Ti brazed interface in order to clarify the phases formation. The model was validated using the fusion lines and temperature testing point comparison of the numerical and experimental results (Figure 4.10). The temperature measurement was carried out using thermocouple at a distance of 43 mm away from the temperature starting testing point and 7 mm far from the FZ center as shown by small black squares in the Figure 4.10(b). Similarly, the curve of temperature cycle was extracted at the same position of the finite element model and plotted as shown by the blue curve in Figure 4.10(b). Figure 4.10 shows that the fusion lines of the numerical and experimental values were found to be almost similar, suggesting that the simulated thermal cycles was in good agreement with experimental results.

The thermal cycle's curves at optimum heat input (1400 W) is plotted in Figure 4.11. The direct irradiation region sustained the highest peak temperature of 1416°C, followed

67

by 1310°C at the middle region and 1280°C at the weld toe region. Ti₃Al phase could be produced at 1180°C (Witusiewicz *et al.*, 2008) and Ti₂Ni (Lee & Nash, 1991) at 984°C in accordance with their binary phase diagrams. According to phase diagrams, the formation temperature of Mg-Al-Ni, Mg-Cu eutectic structure and Mg-Al eutectic were 700°C, 487°C and 325°C respectively. Thus, all the phases could be formed at the considered zones.
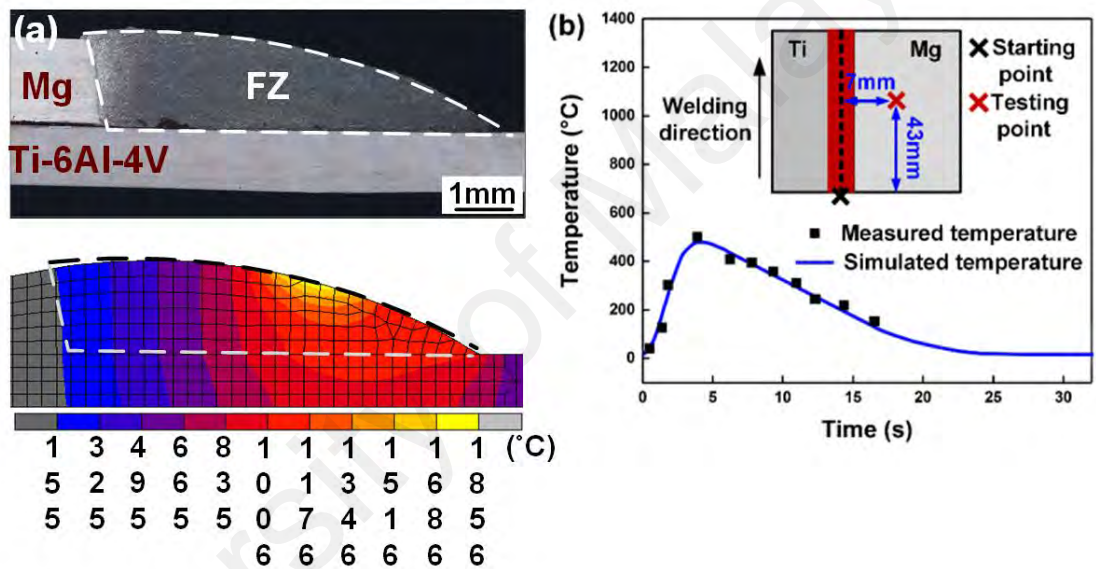
Figure 4.10: Numerical model validation of AZ31/Ti64 joint at 1400 W: (a) comparison of the fusion-line; and (b) experimental and simulated temperature testing point comparison.
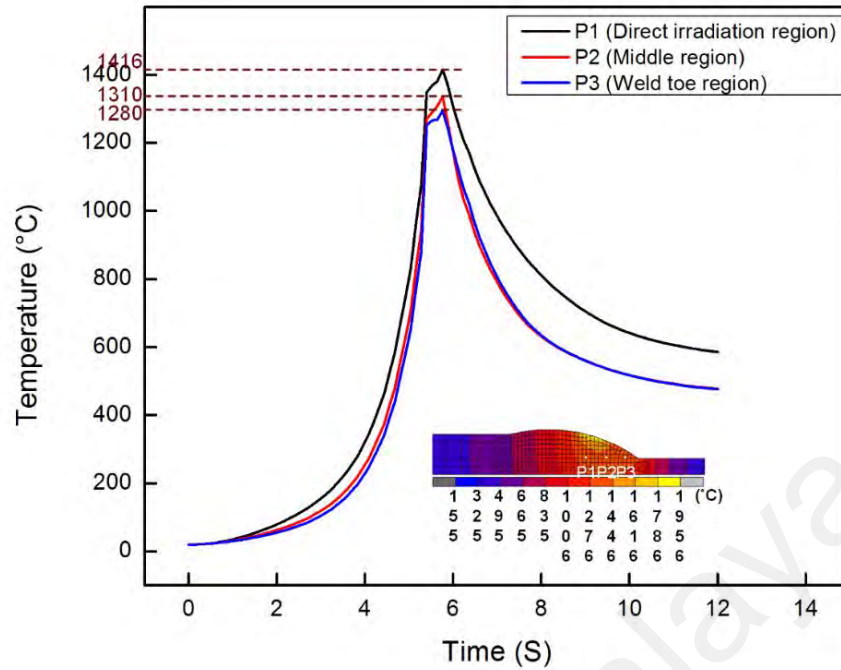
Figure 4.11: Simulation of thermal cycles at the various regions at 1400 W.

4.1.5 Bonding mechanism

According to the microstructural evolution (Figures 4.5 and 4.7), confirmation of the phases produced (Figure 4.9) and the numerical simulation of the thermal cycles (Figure 4.11), the bonding mechanism for the AZ31/Ni-Cu/Ti64 is thus proposed as schematically shown in Figure 4.12. According to this mechanism, during the heating stage, the laser beam irradiated on the Mg filler metal and it first melted. The molten Mg based filler then dropped on coating layer and spread out as illustrated on Figure 4.12(a). The thermal gradient at the interface resulted in varied reactions at different zones.

The increase in laser power or heat input caused the joint temperature to increase. In addition, the temperature of one joint decreased from direct irradiation to middle and finally the weld toe zones. At high temperature, Ti substrate became in-contact with liquid filler and part of it became active. The Ni, Cu and Al atoms in the molten pool would diffuse towards the Ti and interact with the Ti atoms as shown in Figures 4.12(c-e). Tan

et al. (2018a) demonstrated that aluminum diffused faster than Ni at low heat input. Moreover, Zhang et al. (2018c) reported that Cu could promote diffusion of Al and Ti atoms. At 1000 W, when the temperature dropped to 1180˚C, only thin Ti_3Al phase was produced along the brazed interface as shown in Figures 4.12(f-h) owing to the limited volume of activated Ti and low diffusion of Ni atoms at low heat input. With further increase of heat input (1400 W), the Ti_3Al phase along the entire brazed interface became thicker. When the temperature dropped to 984˚C or below, Ni atoms diffused towards the Ti dispersing about the Ti_3Al IMC, which resulted in the formation of Ti_2Ni as shown in Figures 4.12(j-k). The intense laser radiation caused the thickness of Ti-Ni and Ti-Al mixed interfacial reaction layer to increase when the laser power increased to 2200 W. Further decrease in temperature to about 700˚C, Mg-Al-Ni phase was formed as illustrated in Figs. 14(l-n) in accordance with Mg-Al-Ni phase diagram (Raghavan, 2009). At 487˚C, the diffused Cu atoms produced eutectic reaction with Mg atoms (α- $Mg+Mg_2Cu$). With further decreased in temperature, eutectic reaction occurred at 325˚C with newly formed (α-$Mg+Mg_{17}Al_{12}$) structure as schematically illustrated in Figures 4.12(o-q).
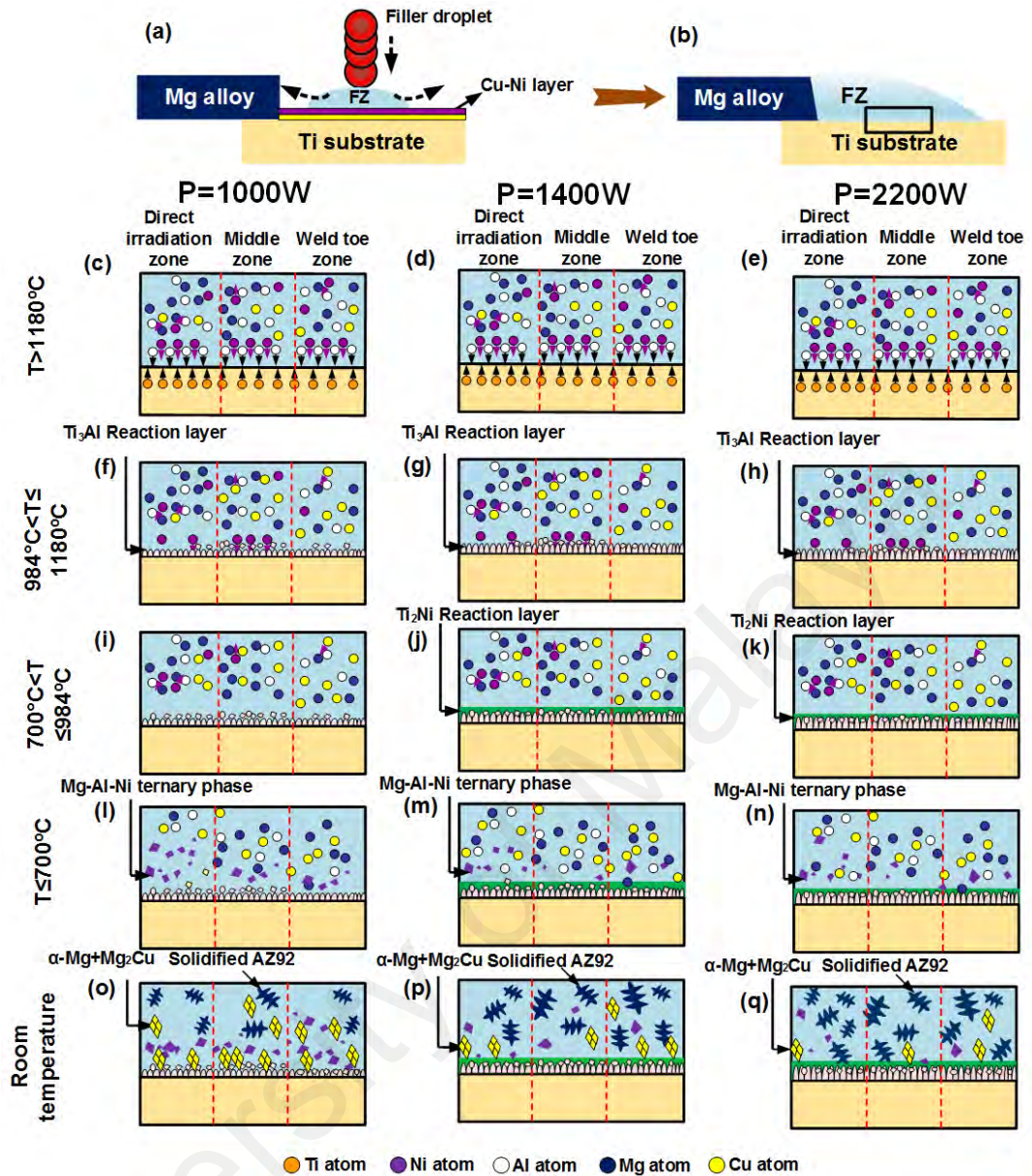
Figure 4.12: Schematic illustration of bonding mechanism for AZ31/Ni-Cu/Ti64 joint: (a)-(b) heating process; (c)-(e) atomic diffusion; (f)-(q) solidification behavior with the decrease in temperature.

4.1.6   Mechanical properties

4.1.6.1   Hardness evaluation

The hardness profiles across the joints at different laser power is presented in Figure 4.13. Both joints showed comparable hardness profiles. For AZ31/Ni-Cu/Ti64 joint, 82 HV average hardness value was observed at the FZ and 353 HV at the Ti substrate,

whereas, that of AZ31/Cu-Ni/Ti64 joint were 85 HV and 356 HV. A distinct increase in the hardness value was observed nearby the brazed interface for joints welded at 1000 W in both cases. This behavior could be associated with the formation of Mg-Al-Ni ternary phases nearby the interface at low heat input. Similar phenomenon was reported by Chatterjee et al. (2006) when welding Ti with Ni. Nevertheless, additional increase in laser power to 1200 W, resulted in a uniform hardness distribution because of the reduction in the Mg-Al-Ni ternary phase resulting from Al, Cu and Ni atoms diffusing to a large area with increasing heat input. This phenomenon was in accordance with the findings in Figures 4.5 and 4.7. Furthermore, the random distribution of the reaction products resulted in a considerable fluctuation in the hardness values. Atieh et al. (2013) reported similar fluctuation of hardness across the Mg/Ti joint.
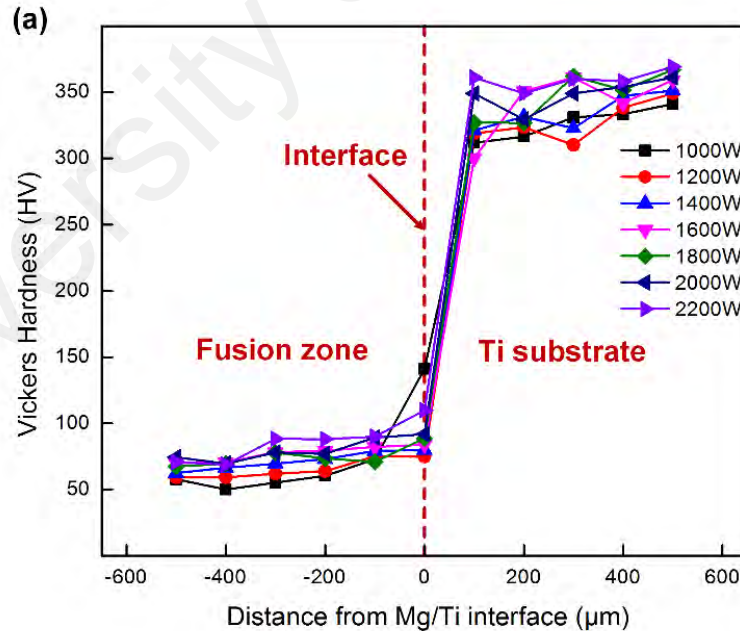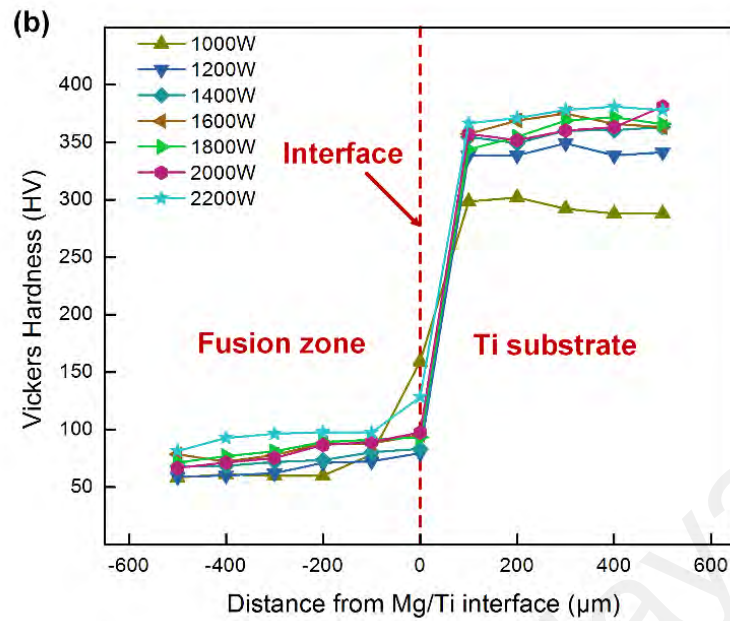
Figure 4.13: Comparison of hardness profiles across the joints at different heat input: (a) AZ31/Ni-Cu/Ti64 and (b) AZ31/Cu-Ni/Ti64.

4.1.6.2   Tensile-shear strength evaluation

Figure 4.14 compared the tensile-shear performance of AZ31/Ni-Cu/Ti64 and AZ31/Cu-Ni/Ti64 at different heat input. As could be noted in Figure 4.14, the tensile-shear performance initial increased when the laser power increased 1000-1400 W in both cases beyond which it continues to decrease. The low value of 989.5 N for AZ31/Cu-Ni/Ti64 and 1129.5 N for AZ31/Ni-Cu/Ti64 at a laser power of 1000 W was primarily associated with insufficient reaction at the interface coupled with formation of a great number of denser Mg-Cu eutectic structure in the fusion zone with network-like morphology. The maximum tensile shear fracture load reached 2016.5 N for AZ31/Ni-Cu/Ti64 and 2014.6 N for AZ31/Cu-Ni/Ti64 at 1400 W, demonstrating approximately 71% joint efficiency compared to AZ31. The increased in the fracture load from 1000 W to 1400 W could be associated with the Al, Cu and Ni atoms diffusing to a large area with increasing heat input, which limited the formation of denser Mg-Cu in both cases. Furthermore, the Ti-Ni and Ti-Al IMCs formation along the FZ-Ti brazed interface

hindered crack propagation and improved the interfacial bonding. Thus, appropriate heat input could increase weld penetration, joining area and spreadability of brazing alloy on the Ti64 in accordance with the results of seam width and contact angle presented in Figure 4.4. Moreover, at optimum heat input (1400 W), both AZ31/Ni-Cu/Ti64 and AZ31/Cu-Ni/Ti64 joints sustained comparable mechanical performance, which corresponded with microstructural analyses presented in Figures 4.5 and 4.7. However, further increased in the laser power deteriorated the joint strength, which was closely associated with excessive evaporation of the filler as shown in Figures 4.3(d) and (f). Furthermore, the diffusion zone increased with increasing heat input, resulting from more Cu, Ni and Al atoms diffused towards the Ti side. Thus, the mixed IMC thickness was significantly higher than the critical thickness of 10 μm (Laukant *et al.*, 2005), giving rise to weak interfacial bonding and lower joint strength. The formation of uneven Al_2Ti IMC at the weld toe area of AZ31/Cu-Ni/Ti64 joint at high heat input (Figure 4.7i) may cause stress concentration and crack because of the large differences in thermal expansion coefficient and thermal conductivity between the base materials. Thus, the joint performance of AZ31/Cu-Ni/Ti64 was weaker than the AZ31/Ni-Cu/Ti64 interlayer arrangement.
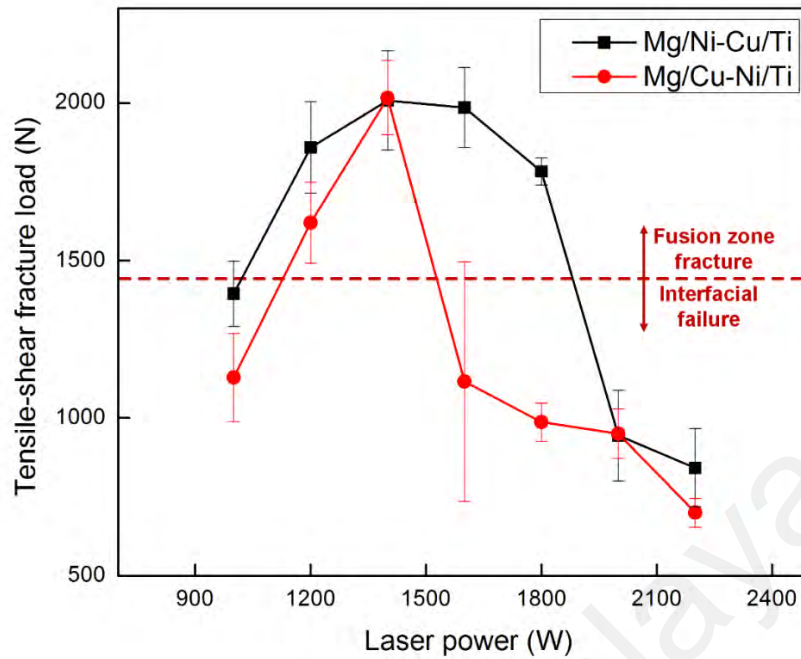
Figure 4.14: Comparison of tensile-shear performance between AZ31/Ni-Cu/Ti64 and AZ31/Cu-Ni/Ti64 at different heat input.

4.1.7 Fracture surface analysis

All the AZ31/Cu-Ni/Ti64 and AZ31/Ni-Cu/Ti64 joints were divided into either interfacial failure or FZ fracture as demonstrated in Figure 4.14. A typical SEM images of the two fracture patterns are shown in Figure 4.15. Furthermore, the relevant EDS analysis of the fracture surfaces are listed in Table 4.4. Tear ridge was formed at the fracture surface of joints that fractured at the interface (Figures 4.15b and d), indicating severe deformation occurred during tensile-shear testing. A number of particles (P2 in Figure 4.15c) mingled with residual Mg (P1 in Figure 4.15c) at the direct irradiation region. These particles contained 26.08 at.% Al and 65.71 at.% Ti, which were confirmed as Ti$_3$Al (Tan *et al.*, 2016b). Furthermore, towards the weld toe region, some dispersed particles (P3 in Figure 4.15e) at the Ti side was observed. This particles were also identified as Ti$_3$Al phase since it consisted of 22.72 at.% Al and 69.65 at.% Ti. On the other hand, for joints that fractured at the FZ, the crack extended along the interface at the

75

weld toe area and then transmitted to the FZ as indicated in Figure 4.15(f). Thus, the interfacial strength along the brazed interface was greater than that of the fusion zone. Dimple features were observed on the fracture surfaces shown in Figure 4.15(g) and (h).
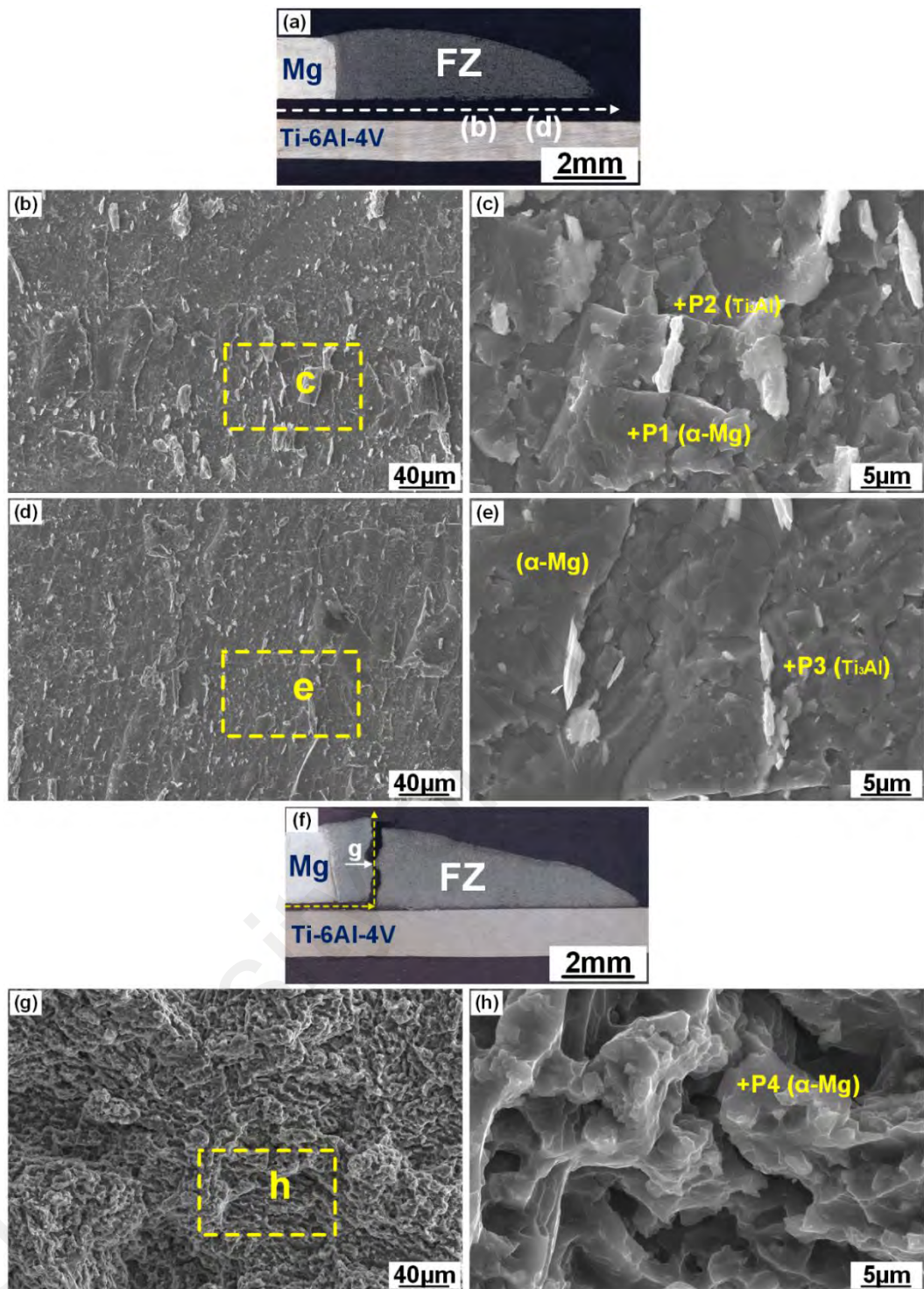
Figure 4.15: SEM micrograph of AZ31/Ti64 fracture surfaces: (a) interfacial failure fracture location; (b) laser irradiation area; (c) higher magnification of the zone shown in (b); (d) middle area; (e) higher magnification of the zone shown in (d); (f) FZ fracture location; (g) Mg side of (f); and (c) higher magnification of the zone shown in (g).

Table 4.4: EDS results of various points presented in Figure 4.15 (at.%).

Point	Mg	Al	Ti	Ni	Cu	Possible phases
P1	87.41	1.27	1.07	4.22	6.03	α-Mg
P2	8.21	26.08	65.71	---	---	Ti$_3$Al
P3	4.63	22.72	69.65	0.59	2.41	Ti$_3$Al
P4	91.24	4.25	1.16	2.03	1.34	α-Mg

4.2 Effect of Cu-Ni layer thickness on joint formation

In addition to the sequence of the metal layers and optimum laser welding-brazing parameters, the interlayer thickness could equally affect the dissimilar joints' microstructural evolution and mechanical properties. Thus, different thickness of the interlayer is expected to exert varied strengthening influence. Optimum welding parameters obtained in section 4.1 were adopted to investigate the effect of the interlayer elements contents. Hence the laser welding parameters of 1400 W, 0.3 m/min welding speed, +30 mm defocused distance and 20 L/min flow of the shielding gas were retained constant and the contents of the electrodeposited Cu and Ni interlayer were optimized. As a result, the influence of Cu and Ni contents on interfacial reaction and joint fracture load were analyzed. Based on which the joining mechanism of the Mg/Ti joints with varied Cu and Ni thicknesses was established.

4.2.1 Electrodeposition

According to the previous results, AZ31/Ni-Cu/Ti64 joints sustained the highest mechanical resistance. Therefore, the electrodeposition of the pure copper and nickel on the Ti64 started with Cu and then Ni (Cu-Ni). A DC power was used during the Cu-Ni electrodeposition process, with pH value of 5 at 35°C. Furthermore, the magnetic stirrer was kept at 200 rpm. In order to get a 20 μm thick uniform copper and nickel Ti substrate, different electrodeposition durations and current densities were tried. When the

electroplating was performed at a current density of 0.3 A/dm^2 for 60 min, an approximate 20 μm Cu and Ni layer on the Ti substrate of different metals layer contents were observed. For each coating condition, the average of at least five coating thicknesses was measured and listed in Table 4.5. The SEM cross sectional micrograph of various Cu-Ni coating thicknesses with uniform characteristics is shown in Figure 4.16. The influence of plating duration was established at constant deposition parameters as shown in Figure 4.16(f) to correlate the coating thickness with plating time. To confirm the defect free Cu-Ni formation on the Ti substrate, EDS mapping analysis was performed as typically shown in Figure 4.17.

Table 4.5: Electroplating time and corresponding coating thicknesses obtained in the electrodeposition process.

Joint	Electroplating time (min)		Coating thickness (μm)		Total
	Cu	Ni	Cu	Ni	
MT-0	0	0	0.00	0.00	0.00
MT-1	10	50	5.47	15.36	20.83
MT-2	20	40	8.41	12.07	20.48
MT-3	30	30	10.78	9.30	20.08
MT-4	40	20	14.49	6.97	21.46
MT-5	50	10	17.12	4.23	21.35
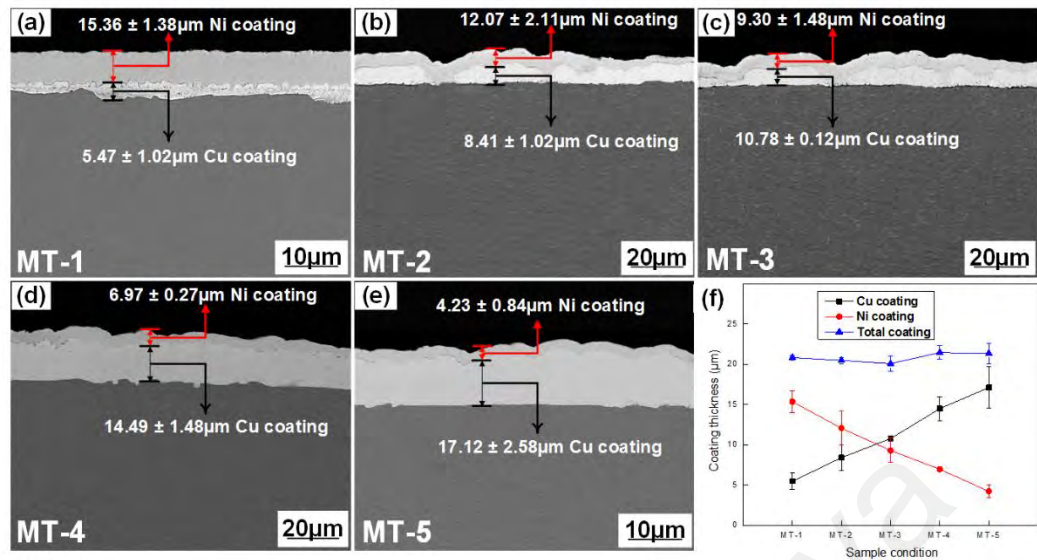
Figure 4.16: SEM cross-sectional micrograph of the Cu-Ni layer at different coating condition: (a) MT-1; (b) MT-2; (c) MT-3; (d) MT-4; (e) MT-5 and (f) Relationship between the coating thickness and sample coating condition.
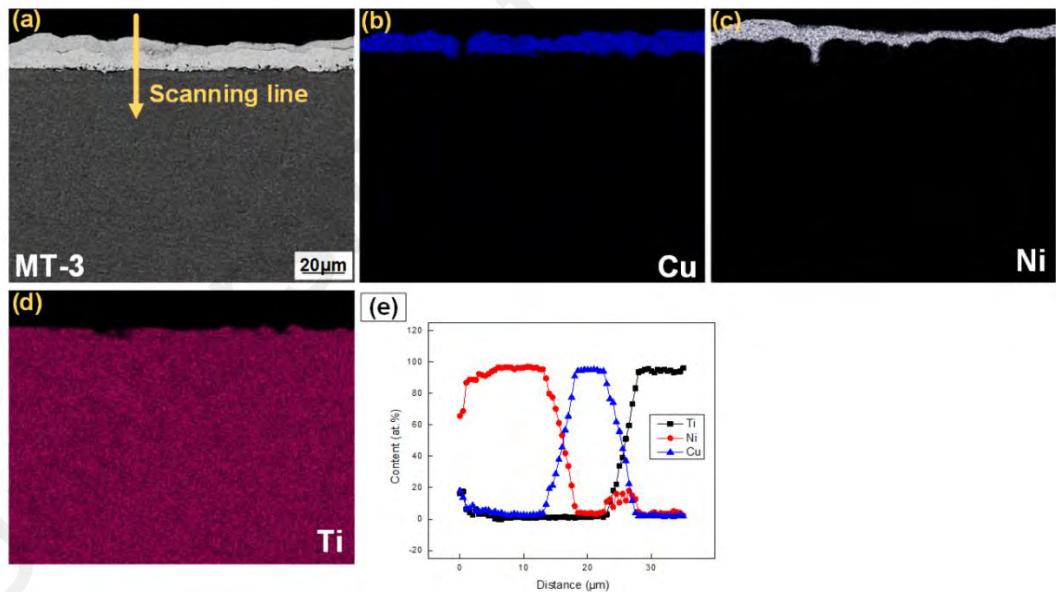
Figure 4.17: EDS mapping analysis of Cu-Ni layer for MT-3: (a) SEM image; (b)-(d) Cu, Ni, Ti; and (e) line scanning result.

4.2.2 Bead appearance and cross-sections

The typical weld appearances and cross sections of joints at various coating thicknesses is shown in Figure 4.18. Under the various coating thicknesses, smooth and uniform weld

surfaces were produced, suggesting the presence of metals layer enhanced the wettability of the liquid filler on the Ti surface. It can be observed from the corresponding joints cross-sections that between the filler and Mg, fusion was observed, whereas, brazing was formed between the FZ and Ti substrate. To further demonstrate the welding characteristics, Figure 4.18(a)-(e) show the fusion lines from the FZ at the Mg BM. However, flat Ti surfaces were observed, suggesting that the Ti base metal did not melt. This is attributed to the positive defocus distance adopted in this study.

To compare the wettability of the brazing alloy on Ti sheet in the various Cu-Ni coating conditions, seam width and contact angle were plotted in Figure 4.19. The contact angle of less than 35° and seam width of up to 6.47 mm were achieved. However, slight variation of the seam width and contact angle was observed at different coating conditions.
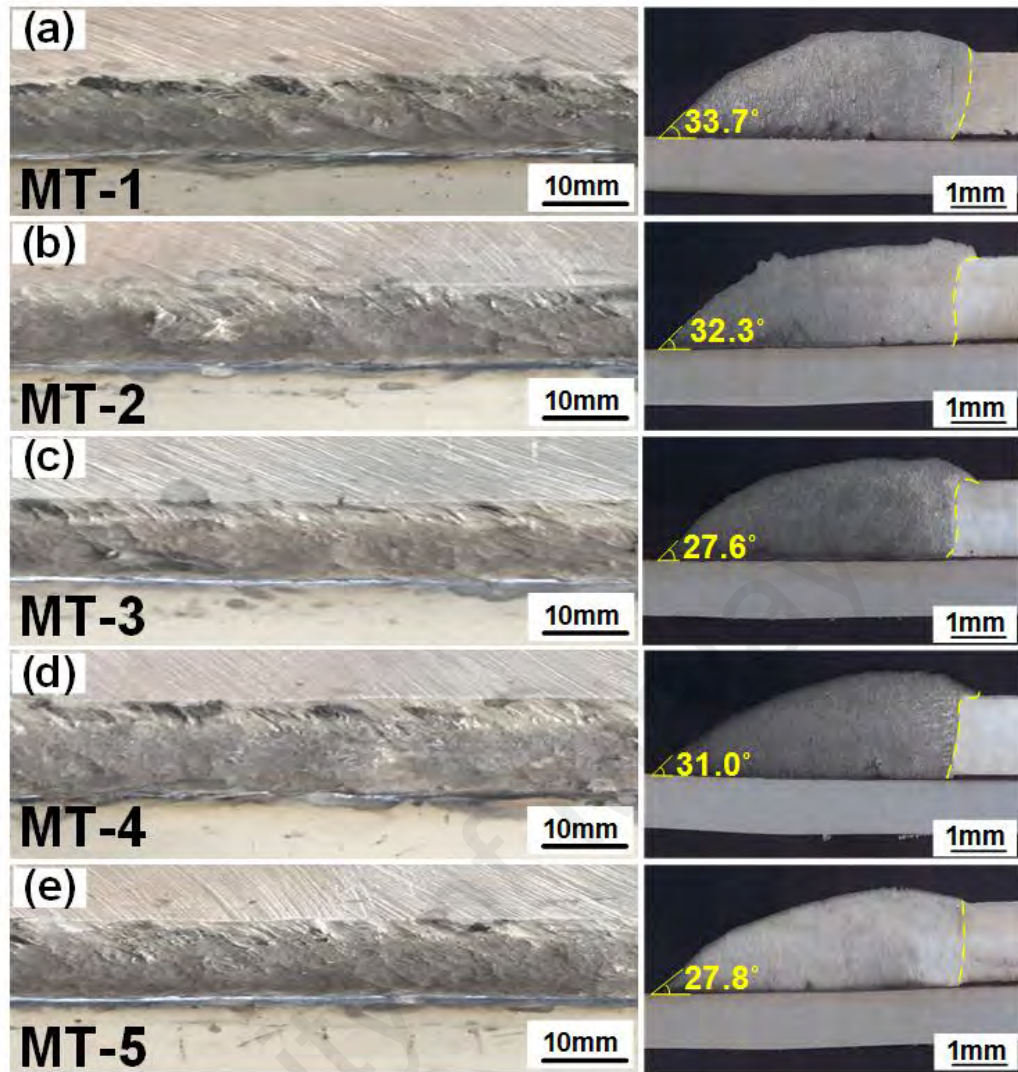
Figure 4.18: Mg/Cu-Ni coated Ti laser welded-brazed joints under various coating conditions: (a) MT-1; (b) MT-2; (c) MT-3; (d) MT-4; and (e) MT-5.
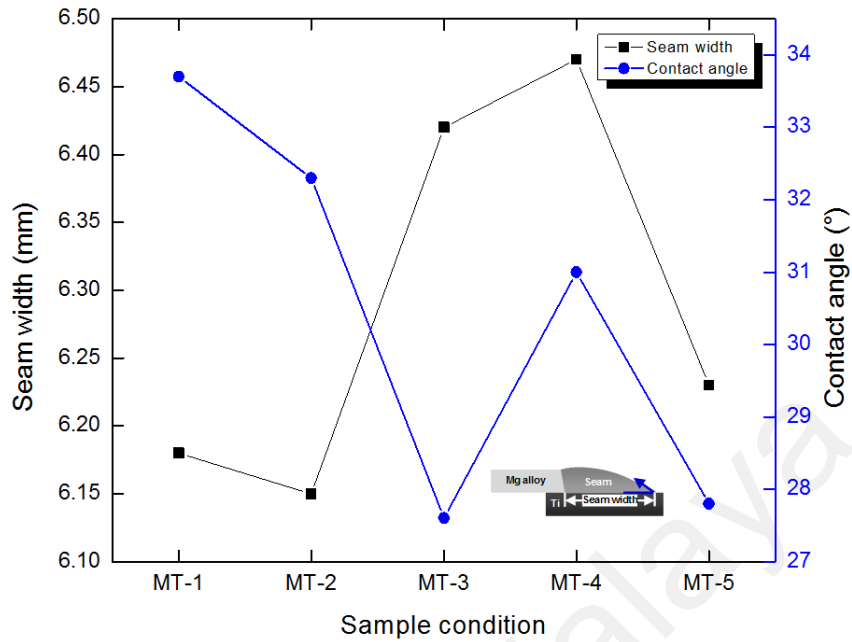
Figure 4.19: Comparison of contact angles and seam widths of the Cu-Ni coated joints under various coating conditions.

4.2.3 Interfacial microstructure

Figures 4.20-4.23 show the interfacial microstructure of the Mg/Ti under various coating conditions were studied under similar welding parameters. Despite the use of the two kind of coatings, the original coating layers were not visible after the LWB process, suggesting suitable heat input used in the current study. The high temperature gradient during LWB process caused the interfacial microstructure along the interface to vary as reported in previous study (Tan *et al.*, 2016c). Thus, the FZ-Ti brazed interface was divided into 3 parts namely: laser irradiation, middle and weld toe zones.

Figures 4.20(a)-(e) show the SEM images of MT-1 joint, i.e. Ni coating thicker than that of Cu (5.47 μm Cu-15.36 μm Ni). To further identify the phase components, EDS analyses were carried out as listed in Table 4.6. The phases formed at different zones were homogenous. At the FZ, the EDS analysis showed that the dark phase (Point P1 in Figure 4.20a) was α-Mg. Meanwhile, the secondary phases (P2 in Figure 4.20a) identified as

$Mg_{17}Al_{12}$ since it contained 27.30 at.% Al and 72.70 at.% Mg were also precipitated in the entire FZ. This precipitated phase was produced during eutectic reaction, which was also reported during TIG welding of Mg/Ti (Xu *et al.*, 2016). In addition, bulk phases (P3 in Figure 4.20b) aggregated in the FZ nearby the interface. These phases were characterized as Mg-Al-Ni phases (Tan *et al.*, 2017b). The generation of these bulk phases could be associated with melting and diffusion of Ni coating into the FZ. At the brazed interface, light gray (P4 in Figure 4.20b) and dark gray (P5 in Figure 4.20b) mixed reaction layer was observed. The light gray phase consisted of 33.07 at.% Al, 42.31 at.% Ti, 19.84 at.% Ni ad 4.39 at.% Cu, which was identified as Ti_2Ni IMC, whereas, the dark gray phase contained 29.66 at.% Al, 61.87 at.% Ti, 6.10 at.% Ni and 2.12 at.% Cu, suggesting it was Ti_3Al in accordance with Ti-Al binary diagram (Witusiewicz *et al.*, 2008). EDS line scanning was carried out across the middle zone as displayed in Figure 4.20(f). The results showed that the Ti content increased and Mg decreased with an apparent segregation of Ni and Al at the brazed interface, signifying the Ti-Ni and Ti-Al IMCs formation. Furthermore, no Cu segregation was noted, indicating that the Cu content was low and under the action of flow and vortex, the thin Cu layer dissolved into the liquid filler.
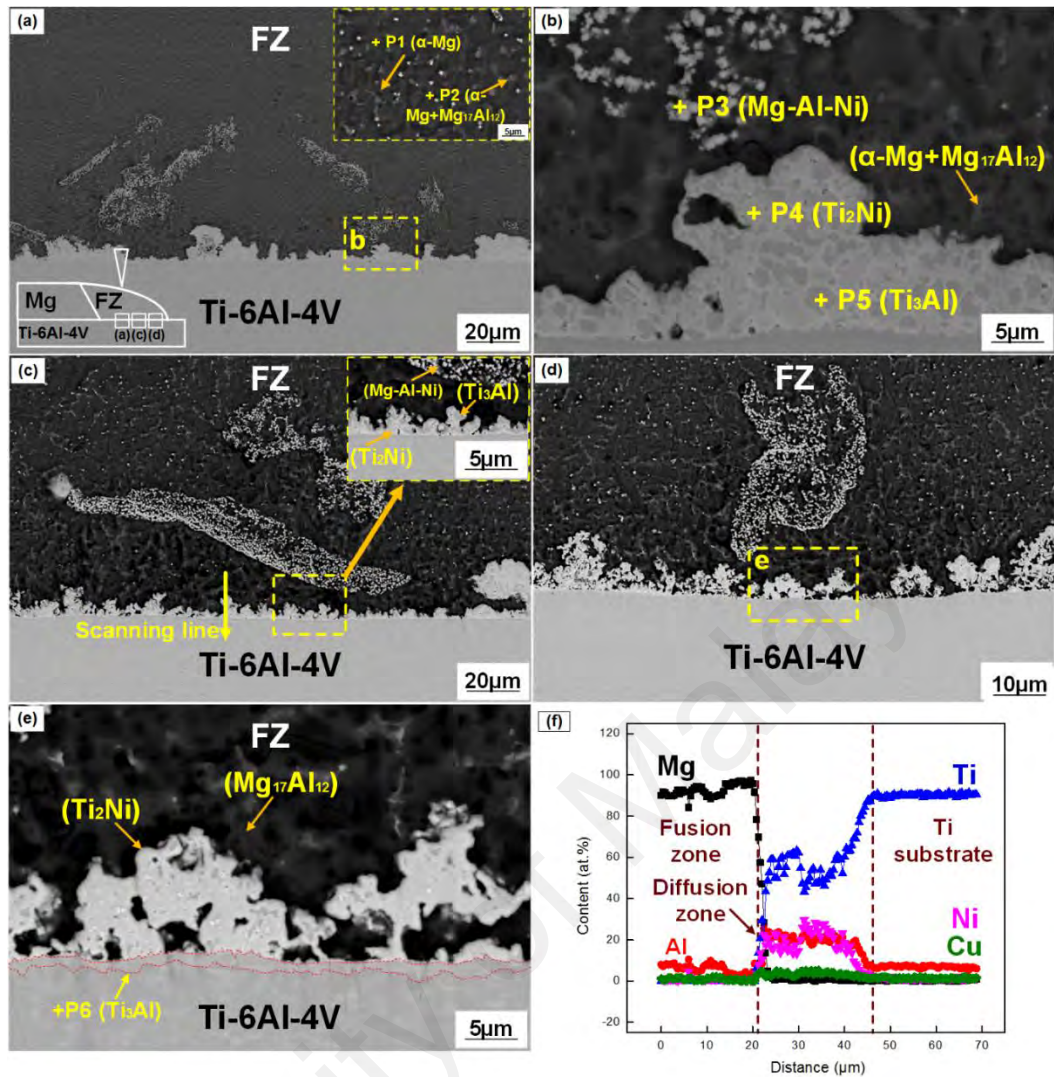
Figure 4.20: Interfacial microstructure morphologies of the MT-1 joint: (a) direct irradiation zone; (b) higher magnification of region b; (c) middle zone; (d) weld toe zone; (e) higher magnification of region e; (f) line scan result of c.

Figures 4.21(a)-(e) present the morphologies of MT-3 joint, i.e. comparable Ni and Cu coating thicknesses (10.78 μm Cu – 9.30 μm Ni). The phases formed at different zones were observed to be inhomogeneous. At the laser irradiation and middle zones adjacent to the brazed interface, some bulk phases (P7 in Figure 4.21a) identified as Mg-Al-Ni compounds were observed. However, compared with MT-1 joint (Figure 4.20), the distribution area of these bulk phases was small, due to the relatively limited Ni atoms. Furthermore, the Ti_3Al and Ti_2Ni mixed reaction layer was produced along the FZ-Ti

brazed interface. Noteworthy, the thickness of this mingle structure was also decrease compared to MT-1 joint. At the weld toe zone, the precipitation of second phase (P8 in Figure 4.21d) inside the FZ increased. These phases contained 13.57 at.% Al, 79.64 at.% Mg, 0.14 at.% Ti, 0.30 at.% Ni, 6.35 at.% Cu, which were ascertained as $Mg_{17}(Al,Cu)_{12}$ owing to the small Cu content. The formation of $Mg_{17}(Al,Cu)_{12}$ phase could be associated with replacement of Al atoms in $Mg_{17}Al_{12}$ by Cu atoms because of their similar atomic radius (Du, 2013). Some dendritic structures (P9 in Figure 4.21d) dispersed around the α-Mg solid-solution matrix with lamellar morphology were also observed nearby FZ-Ti brazed interface as shown in Figure 4.21(e). These dendritic phases consisted of 15.87 at.% Al, 67.62 at.% Mg, 4.20 at.% Ni, and 12.21 at.% Cu. Combined with our previous study (Zhang *et al.*, 2018c), these phases were confirmed as Mg-Cu (α-Mg+Mg_2Cu) (Wang *et al.*, 2016). EDS line scanning results (Figure 4.21f) across the weld toe zone of FZ-Ti brazed interface showed that the Ti content increased and Mg decreased with an apparent segregation of Ni and Al at the brazed interface, suggesting possible formation of Ti-Al and Ti-Ni intermetallic compounds. In contrast, the Cu concentration observed in Figure 4.21(f) due to the presence of Mg-Cu phase adhered to the brazed joint. EDS mapping analysis at the weld toe zone (Figure 4.22) showed that the Al and Ni contents concentrated at along the interface (Figure 4.22b), indicating possible formation of Ti_3Al and Ti_2Ni IMCs with thickness of approximately 5.34 μm. Figure 4.22(d) indicates that the Cu atoms diffused into the FZ to participate in microstructure development. The small Cu concentration observed along the FZ-Ti brazed interface could be associated with Mg-Cu phase adhered to the interface.
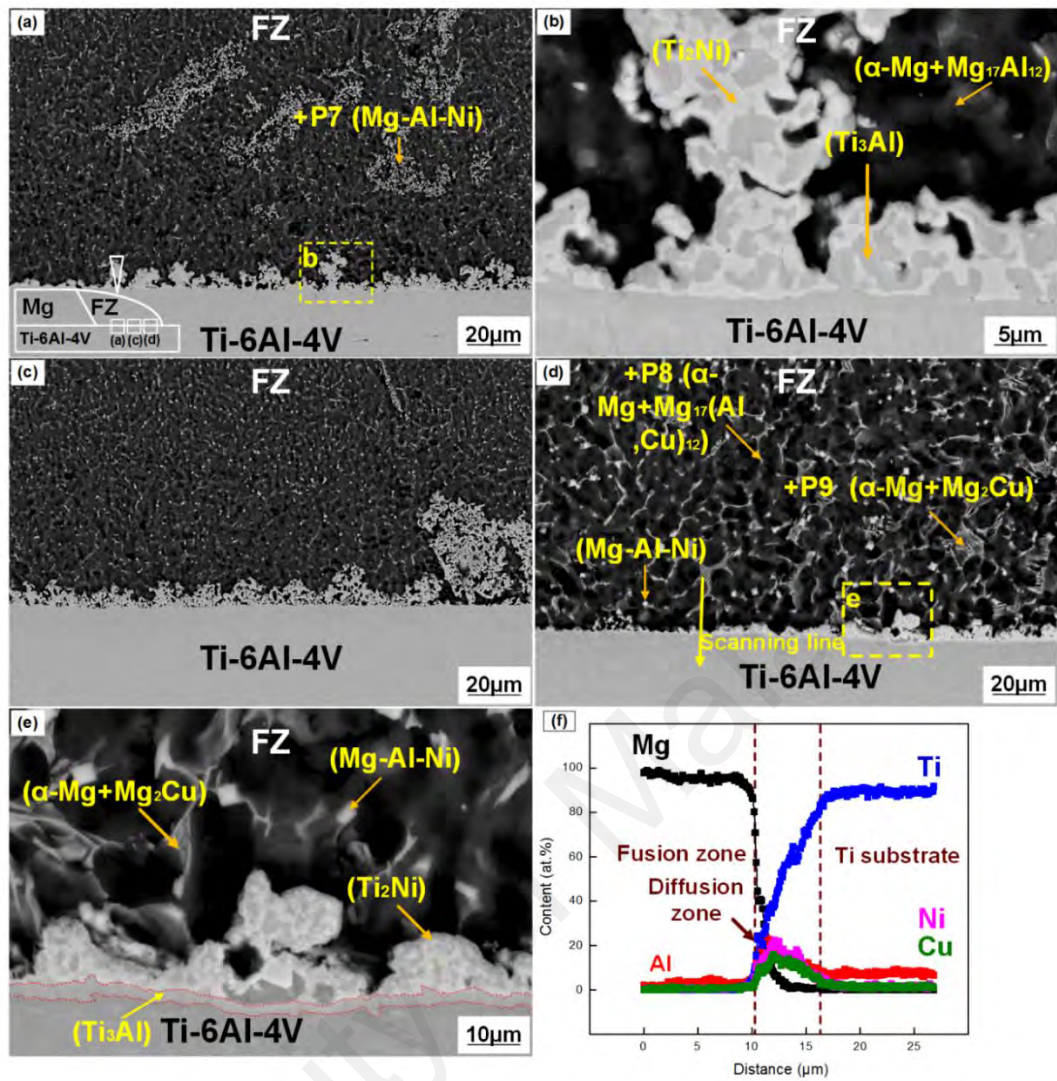
Figure 4.21: Interfacial microstructure morphologies of the MT-3 joint: (a) direct irradiation zone; (b) higher magnification of region b; (c) middle zone; (d) weld toe zone; (e) higher magnification of region e; (f) line scan of d.
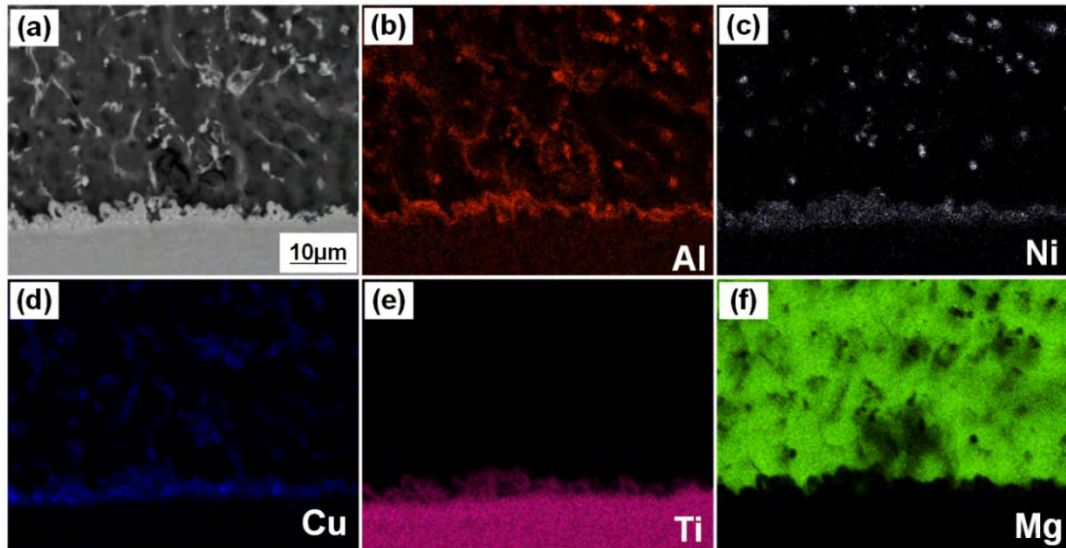
Figure 4.22: EDS mapping of MT-3 joint at the weld toe region: (a) corresponding SEM image; (b)-(f) Al, Ni, Cu, Ti, and Mg.

Figures 4.23(a)-(d) show the interfacial microstructure morphologies of MT-5 joint, where the Cu coating thickness is higher than that of Ni (17.12 μm Cu – 4.23 μm Ni). The phases formed at different zones were also observed to be inhomogeneous. At the laser irradiation zone, $Mg_{17}(Al,Cu)_{12}$ secondary particles precipitated in the entire FZ. At the joint brazed interface, an IMCs containing light gray (P10 in Figure 4.23a) with some dark gray phases (P11 in Figure 4.23a) were confirmed as Ti_2Ni and Ti_3Al, respectively. Owing to the limited Ni contents, only Ti_3Al (P12 in Figure 4.23b) formed at the middle zone, according to the compositions examination. Furthermore, limited content of Ni content coupled with strong stirring caused the Mg-Al-Ni bulk compounds to be concentrated at the FZ of weld toe zone. In addition, large amount of Mg-Cu dendritic structure with lamellar morphology dispersed around the α-Mg matrix as shown in Figure 4.23(d). Owing to the high Cu contents, the distributions of this denser eutectic structures was more than that of MT-3 joint. An uneven IMC layer (P13 in Figure 4.23d) was produced at the interface of the weld toe zone. This uneven layer contained 6.69 at.% Al, 62.52 at.% Ti, 4.38 at.% Ni and 26.11 at.% Cu, suggesting it was Ti_2Cu. IMCs containing

Ti-Al was not observed in this region due to insufficient Ti and Al diffusion force. EDS mapping was performed at the weld toe zone as shown in Figure 4.24. The distribution of the Cu along the FZ-Ti brazed interface was discontinuous (Figure 4.24d), suggesting possible formation of uneven Ti_2Cu phase. In comparison, no Al and Ni concentrated at the interface (Figure 4.24b and c), which corresponded to the analysis of microstructure morphology in Figure 4.23(d). To further confirm the phases observed, XRD analysis was carried out on MT-5 and the result is shown in Figure 4.25. Diffraction peaks belonging to Ti_3Al, Ti_2Ni, Ti_2Cu and Mg_2Cu were detected, thus verifying the result obtained in Figure 4.23.
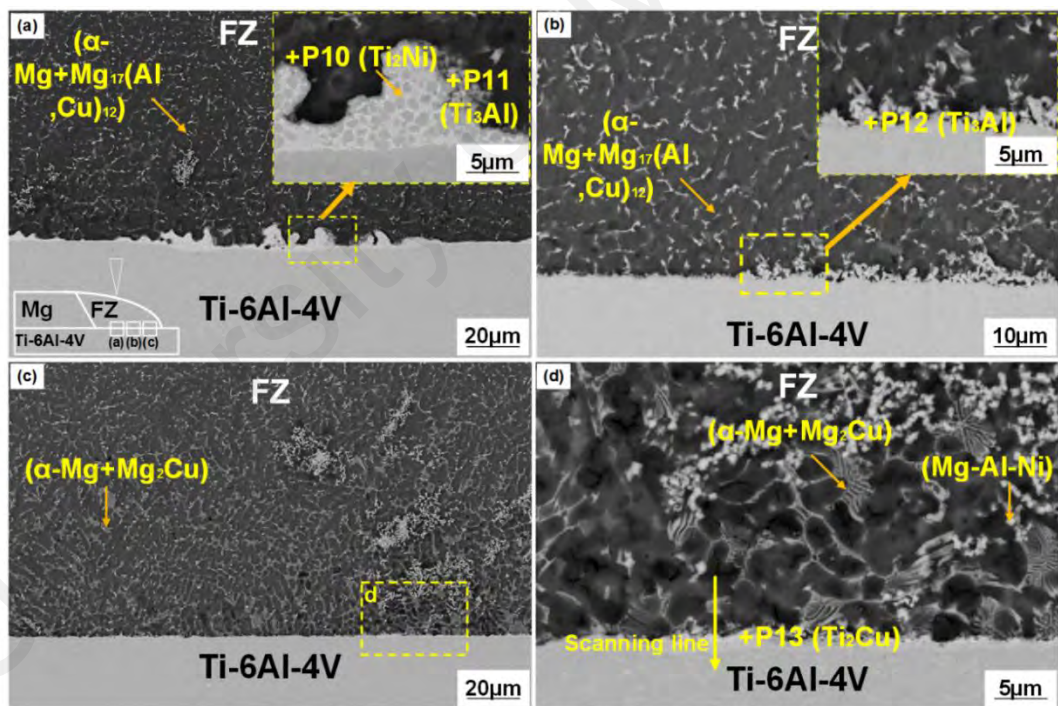
Figure 4.23: Interfacial microstructure morphologies of the MT-1 joint: (a) direct irradiation zone; (b) middle zone; (c) weld toe zone; and (d) higher magnification of region d.
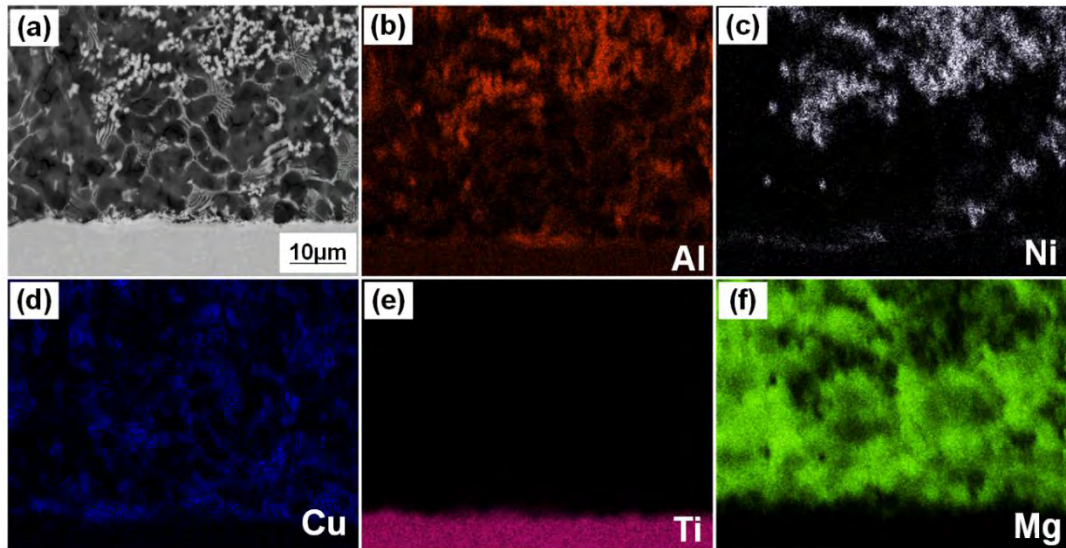
Figure 4.24: EDS mapping of MT-5 joint at the weld toe region: (a) corresponding SEM image; (b)-(f) Al, Ni, Cu, Ti, and Mg.
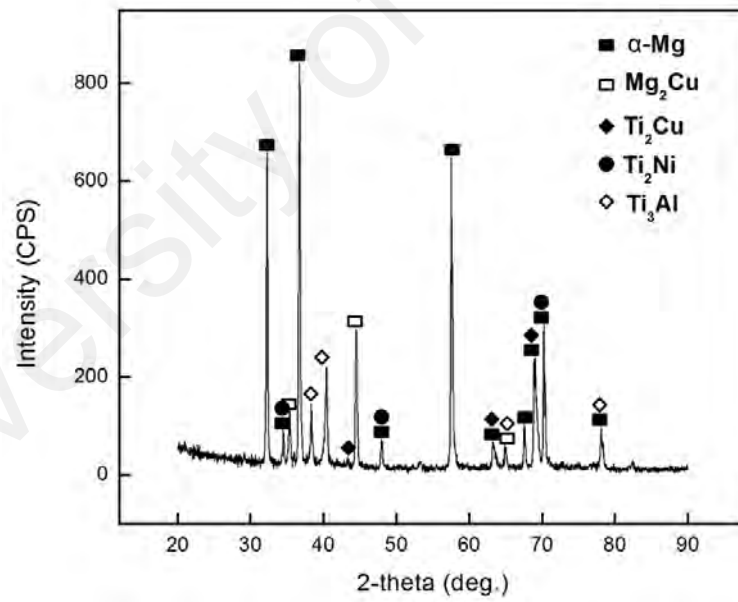
Figure 4.25: XRD analysis of the MT-5 joint.

Table 4.6: EDS results of various points presented in Figures 4.20, 4.21 and 4.23 (at.%).

Point	Mg	Al	Ti	Ni	Cu	Possible phases
P1	90.96	9.04	---	---	---	α-Mg
P2	72.70	27.30	---	---	---	$Mg_{17}Al_{12}$ + α-Mg
P3	42.60	39.62	---	17.78	---	Mg-Al-Ni
P4	0.40	33.07	42.35	19.39	4.79	Ti_2Ni
P5	0.25	29.66	61.87	6.10	2.12	Ti_3Al
P6	0.03	17.99	71.57	8.08	2.33	Ti_3Al
P7	42.53	29.75	0.90	25.32	1.50	Mg-Al-Ni
P8	79.64	13.57	0.14	0.30	6.35	$Mg_{17}(Al,Cu)_{12}$ + α-Mg
P9	67.62	15.87	0.10	4.20	12.21	α-Mg + Mg_2Cu
P10	0.72	12.69	59.00	22.12	5.47	Ti_2Ni
P11	6.84	20.70	60.89	6.45	5.12	Ti_3Al
P12	1.32	27.35	67.19	2.27	1.87	Ti_3Al
P13	0.30	6.69	62.52	4.38	26.11	Ti_2Cu

4.2.4 Joining mechanism

Based on the microstructure development, confirmation of the newly formed phases and the numerical simulation of temperature field (Figure 4.26), the bonding mechanism of the joint was proposed. Figure 4.27 presents the typical schematic illustrations of MT-5 joining mechanism. At the heating stage, the laser beam irradiated on the Mg filler metal and it first melted. The molten Mg based filler then dropped on Cu-Ni layer and spread out as illustrated on Figure 4.27(a). Owing to the violent stirring at the direct irradiation and middle zones, the Cu coating dissolved into the fusion zone and the melted Ni coating diffused into Ti and FZ. At high temperature, the Ti substrate become in-contact with liquid filler and part of it became active. As shown in Figure 4.27(c), the Ni, Cu and Al atoms in the molten pool diffused toward the Ti and interacted with Ti atoms, whereas,

part of Cu atoms being in direct contact with Ti adhered to the Ti substrate towards the weld toe zone due to weaker stirring.

According to the temperature field simulation analysis shown on Figure 4.26, at laser irradiation (P1) and middle (P2) zones, the maximum temperature was higher than the formation temperature of Ti_3Al phase (>1180˚C). Thus, when the temperature dropped to 1180˚C, Ti_3Al phase was the first to be precipitated in these regions (Figure 4.27d). Further decreased in temperature to 984˚C, the Ni atoms diffused toward the Ti side dispersing all over the precipitated Ti_3Al phase at the laser irradiation zone, which resulted in the formation of Ti_2Ni as schematically illustrated in Figure 4.27(e). When the temperature dropped below 980˚C or below, only Ti_2Cu phase was produced at the weld toe area (Figure 4.27f). The maximum temperature at the weld toe region (P3 in Figure 4.26) was 1069.39˚C, which was less than the formation temperature of Ti_3Al phase. This phenomenon could be associated with insufficient Al and Ti diffusion force in this region. Further decreased in temperature to about 700˚C, caused the Ni, Al and Mg to concentrate in the FZ of weld toe zone and Mg-Al-Ni phase was formed (Figure 4.27g) in accordance with Mg-Al-Ni ternary phase diagram (Raghavan, 2009). At 487˚C, the diffused Cu atoms formed eutectic reaction with Mg atoms (α-Mg+Mg_2Cu) at the weld toe zone. Lastly, $Mg_{17}(Al,Cu)_{12}$ was formed with further decreased in temperature at both laser irradiation and middle zones (Figure 4.27h).
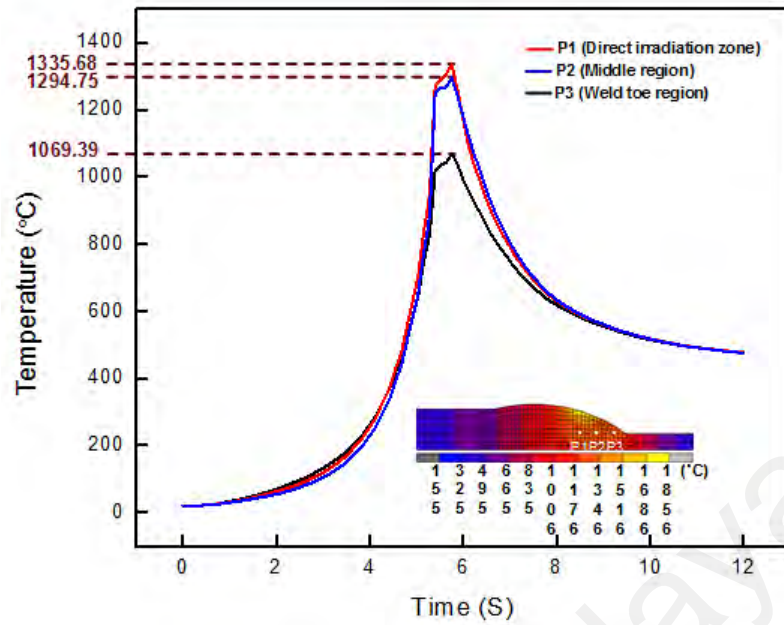
Figure 4.26: Simulation of thermal cycles of MT-5 joint at various zones.
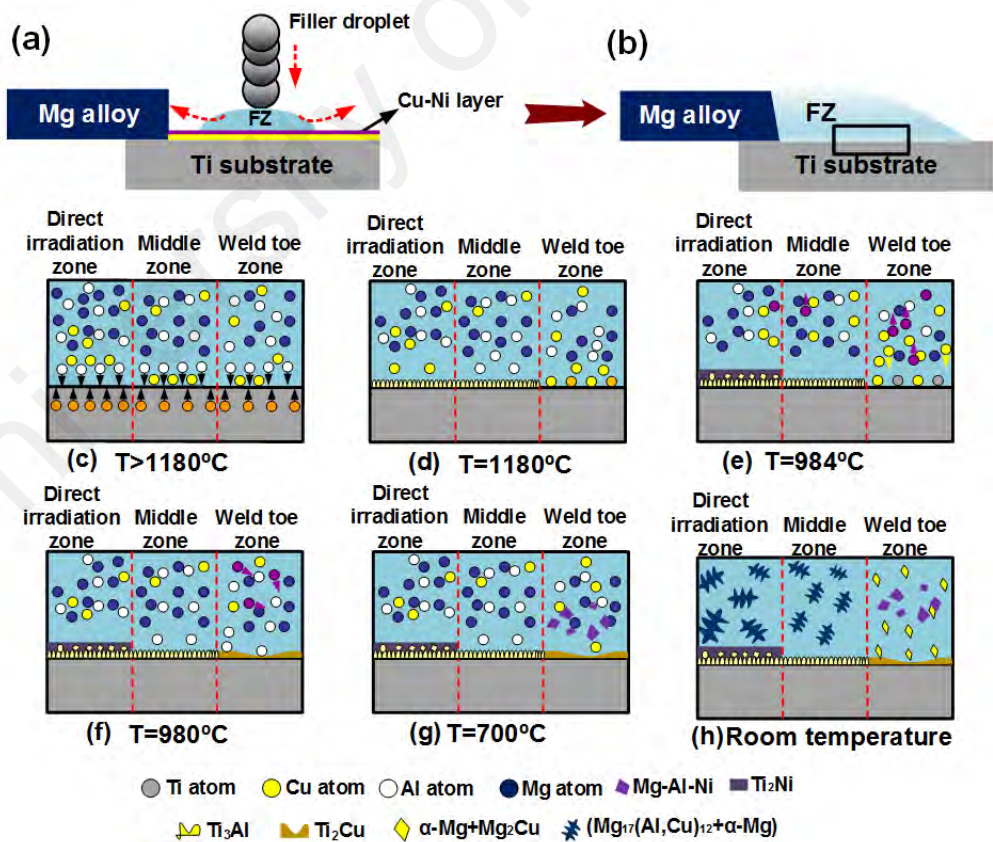
Figure 4.27: Schematic illustration of bonding mechanism of MT-5 joint: (a)-(b) heating process; (c) atomic diffusion; (d)-(h) solidification behavior with the decrease in temperature.

4.2.5   Tensile-shear performance

The tensile-shear performance of Mg/Ti joints with various Cu and Ni contents is shown in Figure 4.28. When the Ni coating was thicker than the Cu, referring to MT-1 and MT-2, the maximum tensile-shear load of 1713 N. The higher mechanical resistance observed was attributed to the Ti-Ni and Ti-Al IMCs formation along the FZ-Ti brazed interface, which hindered crack propagation and improved the interfacial bonding. Despite the limited Cu content, the Cu atoms enhanced mutual reaction between Ti and Al as demonstrated in previous study (Zhang *et al.*, 2018c), which could improve metallurgical bonding and increase the joint mechanical property. Nevertheless, the thickness of the IMC was greater than the critical value of 10 μm (Laukant *et al.*, 2005), which could adversely affect the joint strength. On the other hand, MT-3 and MT-4 joints presented the highest tensile shear fracture load. The higher joint strength obtained could be associated with formation of Ti-Al and Ti-Ni IMCs. Interestingly, the mixed reaction layer thickness was less than the critical value, which could enhanced the joint tensile strength. The tensile-shear load reached maximum value of 2020 N with MT-3 joint. For MT-5 joint, the thick Cu coating enhanced the Ti-Al reaction at the laser irradiation and middle zones and promoted the Ti-Cu IMC formation at the weld toe zone, which improved the joint mechanical resistance. The tensile shear fracture load attained maximum value of 1660 N, which is lower than the remaining coated joints. The declined in the joint performance was associated with the more formation of denser Mg-Cu with increasing Cu coating in the fusion zone with network-like morphology being formed as shown in Figure 4.23(d). The denser eutectic structure resulted in the decreased in the tensile-shear fracture load. Furthermore, Mg and Ti have huge discrepancies in their thermal expansion coefficient and thermal conductivity, which resulted in the generation of welding residual stress (Tan *et al.*, 2018b). Thus, the uneven Ti_2Cu IMC formed at the

weld toe region (Figure 4.23c) may cause stress concentration, which could further deteriorate the tensile shear load and resulted in interfacial failure (Zhang *et al.*, 2018c).
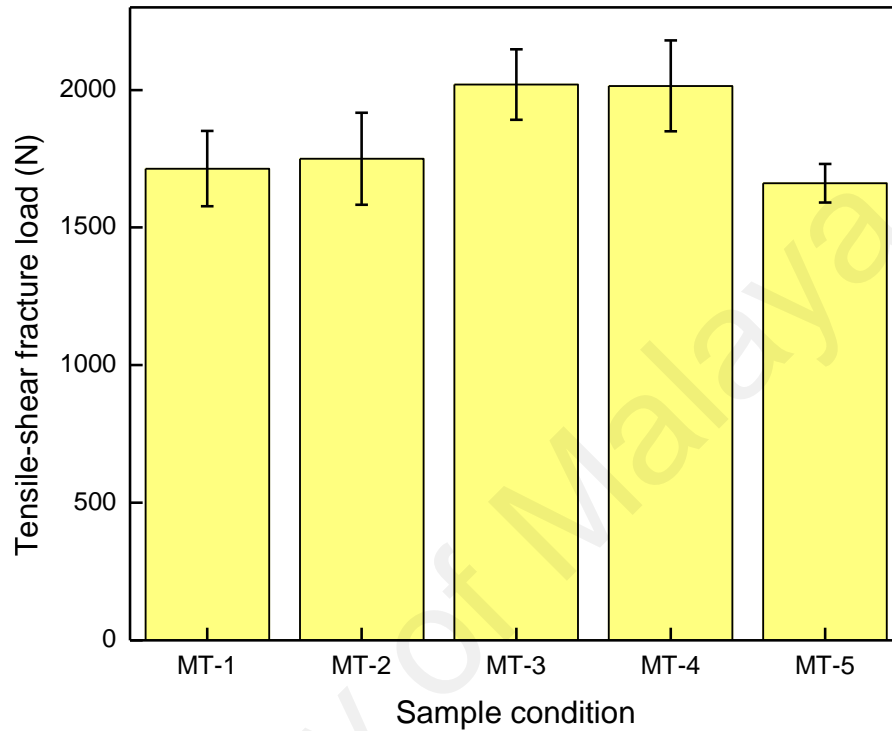
Figure 4.28: Mg/Ti joints tensile-shear fracture loads under various coating conditions.

4.2.6 Fracture surface analysis

With exception of MT-5 joint that fractured along the interface, all the coated joints fractured at fusion zone during the tensile shear testing. Figure 4.29 shows the SEM morphologies of the fracture surfaces in the two fracture patterns and the relevant EDS analysis are listed in Table 4.7. For joints that fractured at the fusion zone, the fracture surface exhibit a typical dimple feature as indicated in Figure 4.29(c). However, as for the joint with interfacial failure mode, tear ridge was observed as shown in Figure 4.29(e)-(g), indicating severe deformation occurred during tensile shear testing. A number of

particles (P3 in Figure 4.29e) mixed with residual Mg (P2 in Figure 4.29e). These particles contained 23.23 at.% Al and 63.84 at.% Ti, which were confirmed as Ti_3Al (Tan *et al.*, 2016b).
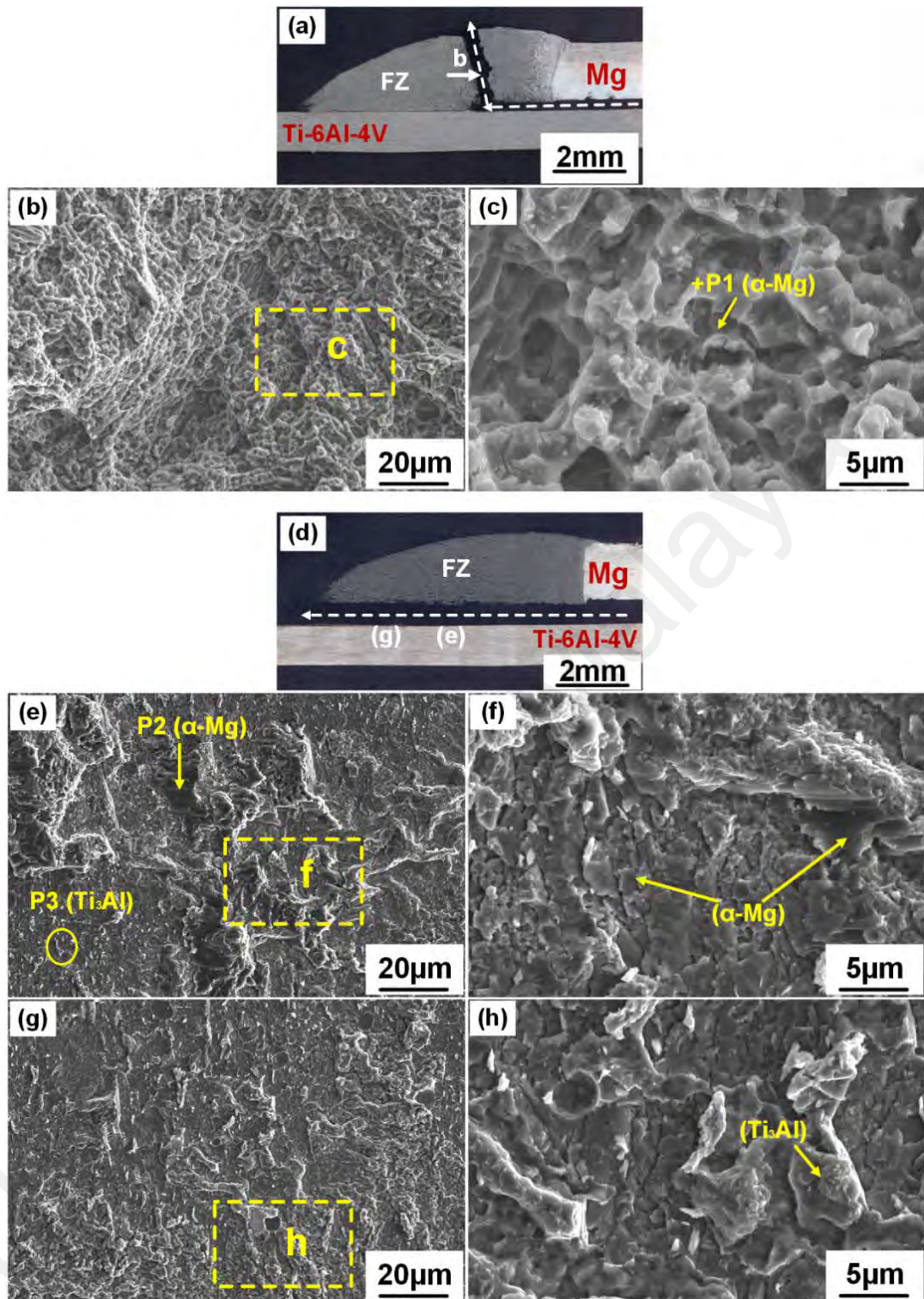
Figure 4.29: Mg/Cu-Ni/Ti fracture surface with various thicknesses at different fracture modes: (a) fracture location of MT-3 with FZ fracture; (b) Mg side of (a); (c) higher magnification of the zone shown in (b); (d) fracture location of MT-5 with interfacial failure; (e) laser irradiation zone; (f) higher magnification of zone shown in (e); (g) middle zone; and (h) higher magnification of the zone shown in (g).

Table 4.7: EDS results of various points presented in Figure 4.29 (at.%).

Point	Mg	Al	Ti	Ni	Cu	Possible phases
P1	94.82	4.65	0.08	0.21	0.24	α-Mg
P2	94.63	4.36	0.76	0.11	0.14	α-Mg
P3	5.96	23.23	63.84	3.63	3.34	Ti$_3$Al

4.3   Comparison of joint performance with and without coatings

To further clarify the role of the Cu and Ni in the bond formation between the Mg/Ti systems, the application of Ni coating, Cu coating and Cu-Ni coatings were comparatively studied and their compatibility to join AZ31B to Ti-6Al-4V is examined under similar experimental condition. In contrast, laser welding-brazing of the direct joint (with no coating) was also conducted under similar welding parameters. The relationships between interface characteristics, joint formation mechanism and mechanical properties were established.

4.3.1   Electrodeposition

Table 3.3 and Table 3.4 show the composition of electroplating solution used for electrodeposition of pure Cu and Ni on the Ti surface, respectively. The electroplating parameters adopted in both cases are given in Table 4.8. Similarly, the electrodeposition of Cu followed by Ni layer on the Ti substrate were also carried out. The electroplating conditions used for the Cu-Ni layer are similar to those for Cu coating and Ni coating. However, during the Cu-Ni electrodeposition, the electroplating time was 0.40 h for Cu and 0.20 h Ni depositions. Cross sectional SEM micrograph of the various coatings on the Ti surface is shown in Figure 4.30. To confirm the defect free coating layer formation on the Ti substrate, EDS mapping was carried out as typically shown in Figure 4.31.
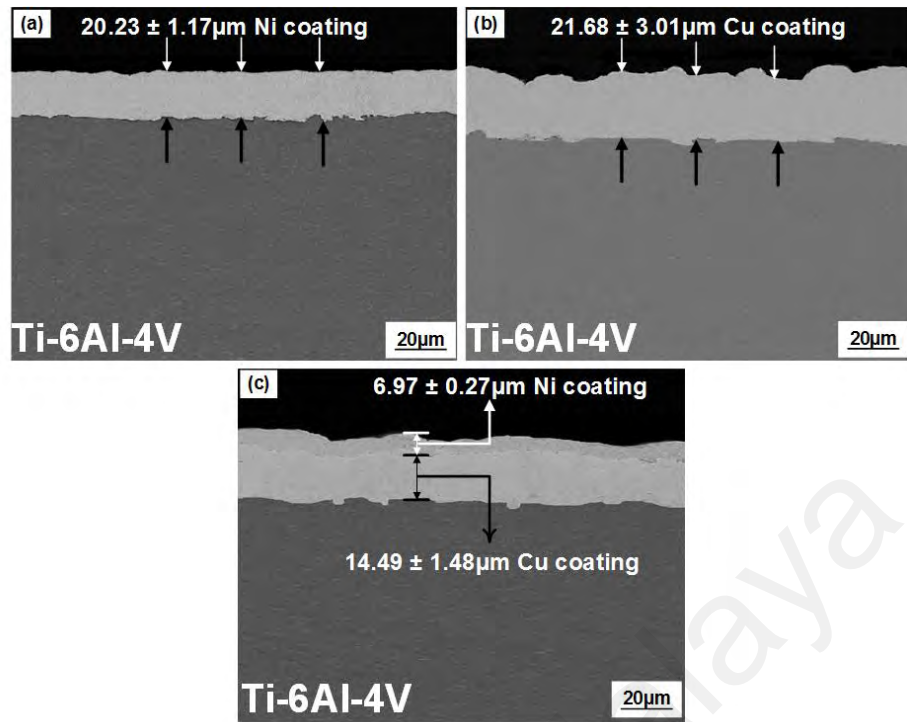
Figure 4.30: SEM micrograph of the various coatings on Ti64 substrate (a) Ni coating, (b) Cu coating and (c) Cu-Ni coating.
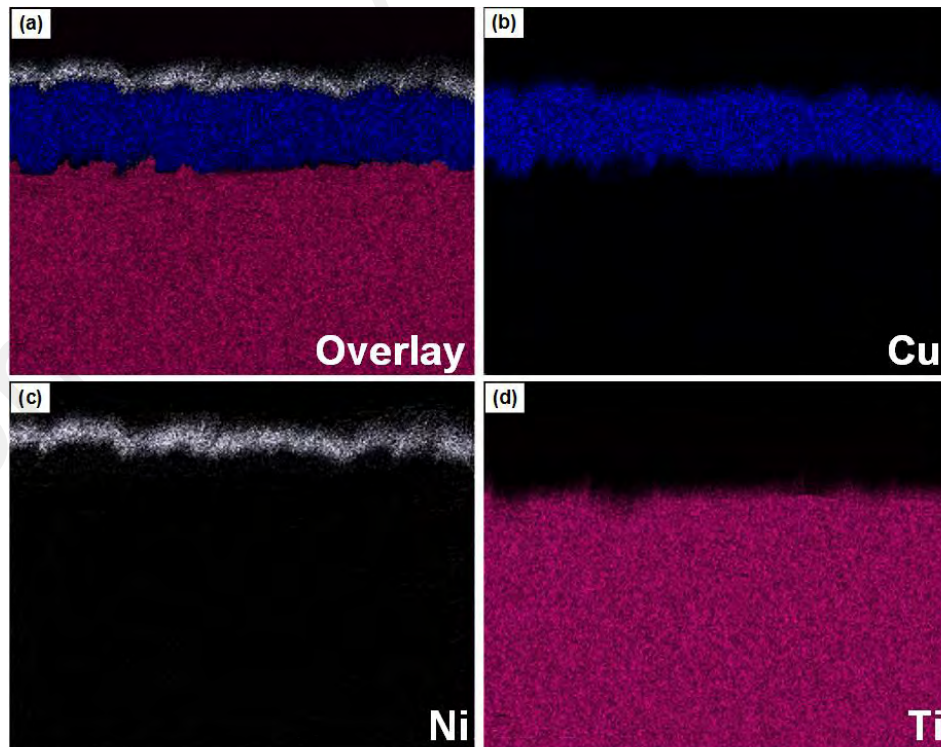
Figure 4.31: EDS mapping analysis of Cu-Ni layer: (a) Overlay image, (b)-(d) Cu, Ni, Ti.

Table 4.8: Electro-plating parameters used in this study.

Parameters	Value
Temperature (˚C)	35
Plating time (h)	1.0
pH	5
Stirrer speed (rpm)	200
Electric current (A)	0.3

4.3.2 Joint appearance and cross-sections

The typical joints appearances obtained with various coatings under similar welding condition is shown in Figure 4.32. For the direct joint (without any coating) large contact angle was observed resulting from the un-wetted filler on the Ti surface as shown in Figure 4.32(a). This behavior was associated with poor affinity of the Mg and Ti. In comparison, for Cu, Ni and Cu-Ni coated joints, significant increase in the joint widths and spreading areas were observed. To further demonstrate the welding characteristics, Figure 4.32(a)-(d) show the fusion lines from the FZ at the Mg BM. In contrast, flat Ti surfaces were observed, suggesting that the Ti did not melt. This is attributed to the positive defocus distance adopted in this study.

To further compare the wettability of molten filler on Ti surface in the uncoated, Ni coating, Cu coating and Cu-Ni coating processing conditions, seam width and contact angle were plotted in Figure 4.33. The uncoated joint presented a seam width of 5.42 mm and contact angle of 50.8˚. For Ni, Cu and Cu-Ni coatings, the contact angle decreased to 33˚, 31.6˚ and 31˚, respectively. Interestingly, the seam width increased to 6.37 mm for Ni coated, 6.21 mm for Cu coated and 6.23 mm for Cu-Ni coated joint, confirming that the presence of the coating improved the wetting and spreading of the liquid filler on Ti sheet (Nasiri *et al.*, 2013a; Tan *et al.*, 2017a).
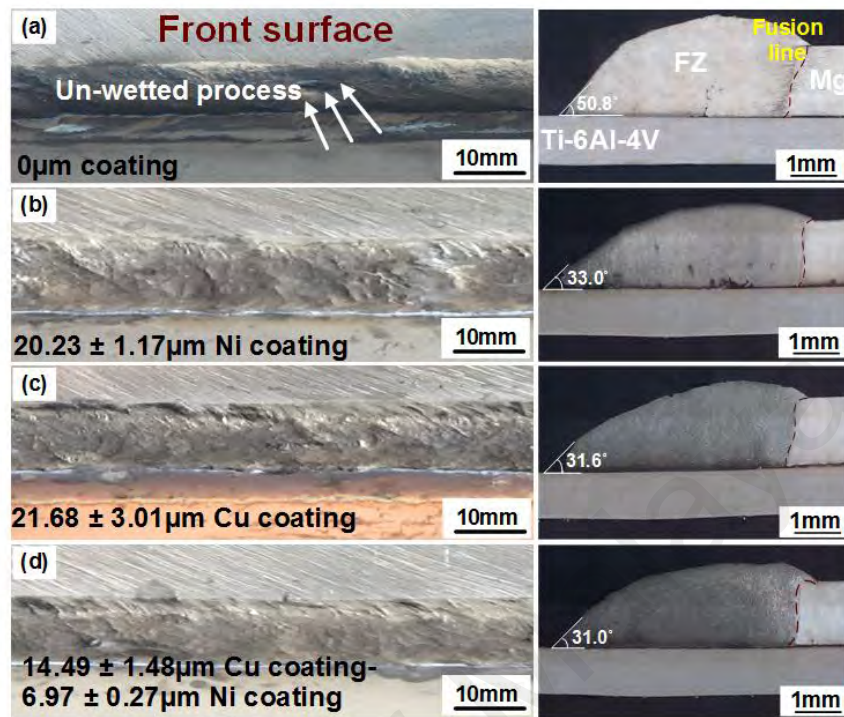
Figure 4.32: Laser welded-brazed Mg/Ti bead appearance and cross sections: (a) Uncoated, (b) Cu coated, (c) Ni coated and (d) Cu-Ni coated.
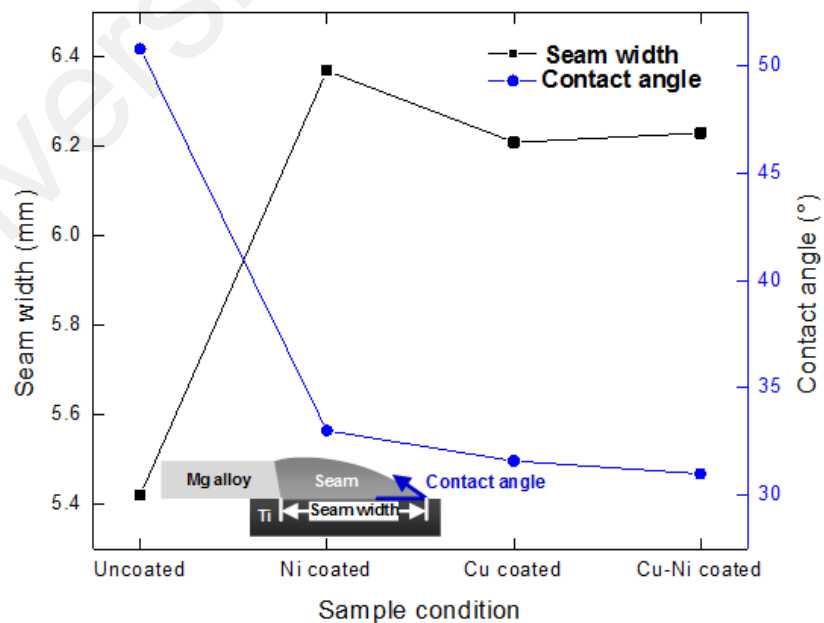
Figure 4.33: Variation of contact angles and seam widths with different coating condition.

4.3.3   Joint interface characteristics

4.3.3.1   Uncoated joint

The interfacial microstructure morphology of the uncoated joint is shown in Figure 4.34. To further confirm the newly formed reaction products, EDS analyses were carried out as listed in Table 4.9. Tan et al. (2016a) demonstrated that for laser welded-brazed joints, high thermal gradient caused varied phases to evolve at different regions along the braze interface. Therefore, the joint interface was divided into three zones as shown in Figure 4.34. Smooth characteristics was observed at the interface of both direct irradiation and middle regions, suggesting no obvious IMC layer formation. To further quantify the element fluctuation in these regions EDS line scan was done and the corresponding result was plotted in Figure 4.34(d). It was found that the Ti content increased and Mg decreased from the FZ to the Ti substrate with an apparent segregation of Al at the interface. The Al atoms and Ti atoms reacted and produced Ti-Al IMCs. According to the outcome of the previous study (Tan *et al.*, 2016a) and the atoms ratios in Figure 4.34(d), the Ti-Al IMC was identified as Ti_3Al. Meanwhile, an obvious discontinuous Ti_3Al IMC (Point P3 in Figure 4.34c) was produced at the weld toe region. Generally, atomic diffusion which depended on the Al atoms diffusing from the FZ determined the precipitation and growth of the Ti_3Al interfacial reaction layer. With maximum of only 9 wt.% Al content in the filler, the diffusion controlled growth of Ti_3Al layer was limited. Thus, smooth brazed interface was mainly observed. In addition, the characteristics of fast heating and cooling rate also restricted the interfacial reaction during the LWB process. Similar phenomenon was observed when LWB of immiscible Mg alloy to stainless steel (Tan *et al.*, 2014).

The dark structure evolved throughout the FZ (P1 in Figure 4.34a) contained 94.49 at.% Mg, 5.51 at.% Al, signifying it was α-Mg. According the EDS results, the gray phase P2 in Figure 4.34(a) around the α-Mg solid-solution was $Mg_{17}Al_{12}$. This precipitated

phase was produced during eutectic reaction. Gao et al. (2011; 2012) also reported the formation Mg$_{17}$Al$_{12}$ eutectic structure during keyhole laser welding of Mg/Ti joints.

Figure 4.34: SEM morphologies of the uncoated joint: (a) direct irradiation zone; (b) middle zone; (c) weld toe zone; and (d) line scan of a.

Table 4.9: EDS results of various points presented in Figure 4.34 (at.%).

Point	Mg	Al	Ti	Possible phases
P1	94.49	5.51	---	α-Mg
P2	79.73	20.27	---	Mg$_{17}$Al$_{12}$ + α-Mg
P3	---	13.13	86.87	Ti$_3$Al + α-Ti

4.3.3.2 Ni coated joint

The interfacial microstructure morphology of the Ni coated joint is shown in Figure 4.35. To further identify the different reaction products formed, EDS analyses were carried out as presented in Table 4.10. After joining, no visible deposited Ni was observed, indicating the total melting of the coated layer. Homogeneous IMCs were observed across the brazed interface. In the FZ, bulk phases (P1 in Figure 4.35a) aggregated near the interface. These phases contained 36.19 at.% Al, 33.19 at.% Mg and 30.41 at.% Ni. Combined with previous study (Tan *et al.*, 2017b), these phases were ascertained as Mg-Al-Ni phases. On the other hand, gray phases (P2 in Figure 4.35a) consisting of 18.27 at.% Al and 81.26 at.% Mg were also precipitated in the entire α-Mg solid-solution, which were confirmed as $Mg_{17}Al_{12}$. This precipitated phase was produced during eutectic reaction, which was also observed during TIG welding of Mg/Ti (Xu *et al.*, 2016). At the interface, mingled discontinuous IMCs containing light gray (P3 in Figure 4.35b) with some dark gray phases (P4 in Figure 4.35b) were observed. According to the EDS results, the light gray was identified as Ti_2Ni. Meanwhile, the dark gray contained 28.77 at.% Al, 63.27 at.% Ti, and 7.10 at.% Ni, thus characterized as Ti_3Al (Witusiewicz *et al.*, 2008). Ni and Al have comparable promoting influence on the Mg/Ti. EDS line scan was performed as shown in Figure 4.35(f). Thick mixed reaction layer was observed, owing to enough Al and Ni atoms, which diffused into the Ti. Thus, wider diffusion zone (38.95 μm) was produced. It can also be inferred from Figure 4.35(f) that Al and Ni segregated at the fusion zone-Ti brazed interface, suggesting the formation Ti-Ni and Ti-Al IMCs.

Furthermore, XRD analysis was performed to verify the newly formed phases and the result is shown in Figure 4.36. Ti_3Al and Ti_2Ni diffraction peaks were observed, which corresponded with the result obtained in Table 4.10.
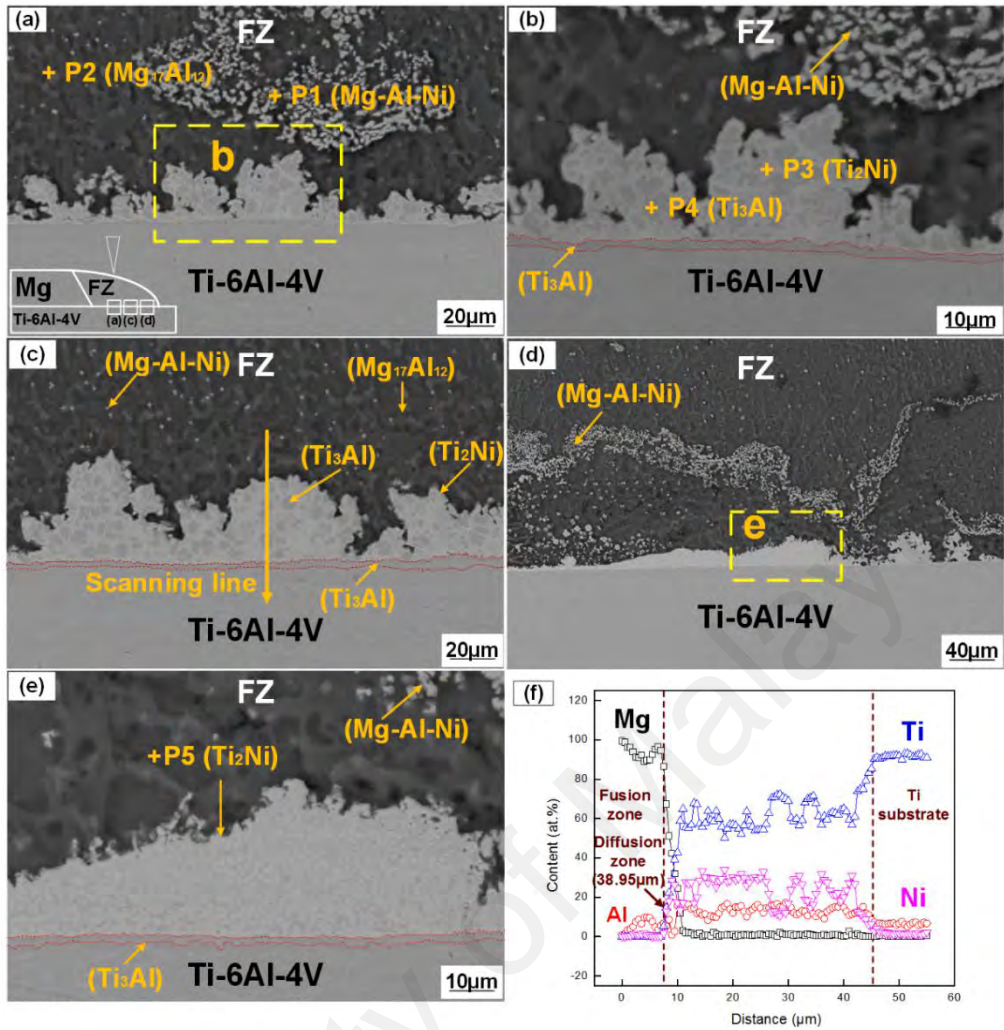
Figure 4.35: Interfacial microstructure morphologies of the Ni added joint: (a) direct irradiation area; (b) higher magnification of zone b; (c) middle area; (d) weld toe area; (e) higher magnification of zone e; (f) line scan of c.

Table 4.10: EDS results of various points presented in Figure 4.35 (at.%).

Point	Mg	Al	Ti	Ni	Possible phases
P1	33.19	36.19	0.21	30.41	Mg-Al-Ni
P2	81.26	18.27	0.23	0.24	$Mg_{17}Al_{12}$ + αMg
P3	0.03	19.70	55.68	24.59	Ti_2Ni
P4	0.86	28.77	63.27	7.10	Ti_3Al
P5	---	11.96	61.91	26.13	Ti_2Ni
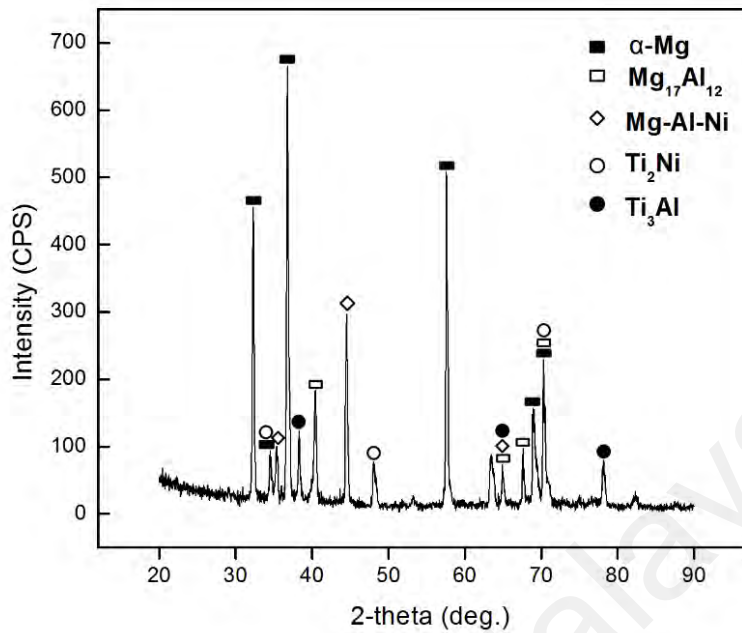
Figure 4.36: XRD result of the Ni added joint.

4.3.3.3 Cu coated joint

Figures 4.37(a)-(c) shows the SEM images of Mg/Cu coated Ti laser welded-brazed joint. To further identify the phase's components, EDS analyses were carried out as presented in Table 4.11. No visible deposited Cu was observed after the welding, suggesting complete melting of the coated layer. Smooth surface was observed at the interface of both direct irradiation and middle regions, suggesting no obvious IMC layer formed. EDS line scan was carried out at the middle region as shown in Figure 4.37(d). The Ti content increased and Mg decreased from the FZ to the Ti substrate with an apparent segregation of Al at the interface. According to the atoms ratios in Figure 4.37(d), the Ti-Al IMC was identified as Ti₃Al, which was similar to the former observation for the uncoated joint. In contrast, Cu segregation in Figure 4.37(d) associated with the presence of Mg-Cu eutectic structure, which adhered to the FZ-Ti brazed interface. Under the action of flow and vortex, most of the Cu atoms dissolved into the

106

molten pool to participate in microstructure development. To verify the formation of these phases, EDS mapping was performed at the middle region as shown in Figure 4.38. The distribution of Cu atoms was discontinuous since most of the Cu atoms dissolved into the molten pool (Figure 4.38c). In comparison, uniform Al concentration at the brazed interface was observed, suggesting possible formation of Ti-Al IMC. At the weld toe region, discontinuous reaction layer (P4 in Figure 4.37c) was produced. This discontinuous layer contained 9.10 at.% Al, 19.23 at.% Cu, 71.67 at.% Ti. Combined with the findings of the previous work (Zhang *et al.*, 2018c), formation of Ti_2Cu IMC was confirmed. Furthermore, XRD analysis was performed to verify the newly formed reaction products and the result is shown in Figure 4.39. Ti_3Al, Ti_2Cu and Mg_2Cu diffraction peaks were detected, which is in accordance with the result presented in Table 4.11.

In the FZ far away from the interface, gray phases (P1 in Figure 4.37a) was $Mg_{17}Al_{12}$, whereas, near the interface, precipitation of the second phase (P2 in Figure 4.37a) increase. This phase was identified as $Mg_{17}(Al,Cu)_{12}$. The formation of $Mg_{17}(Al,Cu)_{12}$ phase could be associated with replacement of Al atoms in $Mg_{17}Al_{12}$ by Cu atoms because of their similar atomic radius (Du, 2013). In addition, dendritic structures (P3 in Figure 4.37c) was also observed in the FZ. This dendritic structure contained 15.87 at.% Al, 71.82 at.% Mg, 12.21 at.% Cu, which was identified as the Mg-Cu (α-Mg+Mg_2Cu) (Tan *et al.*, 2015).

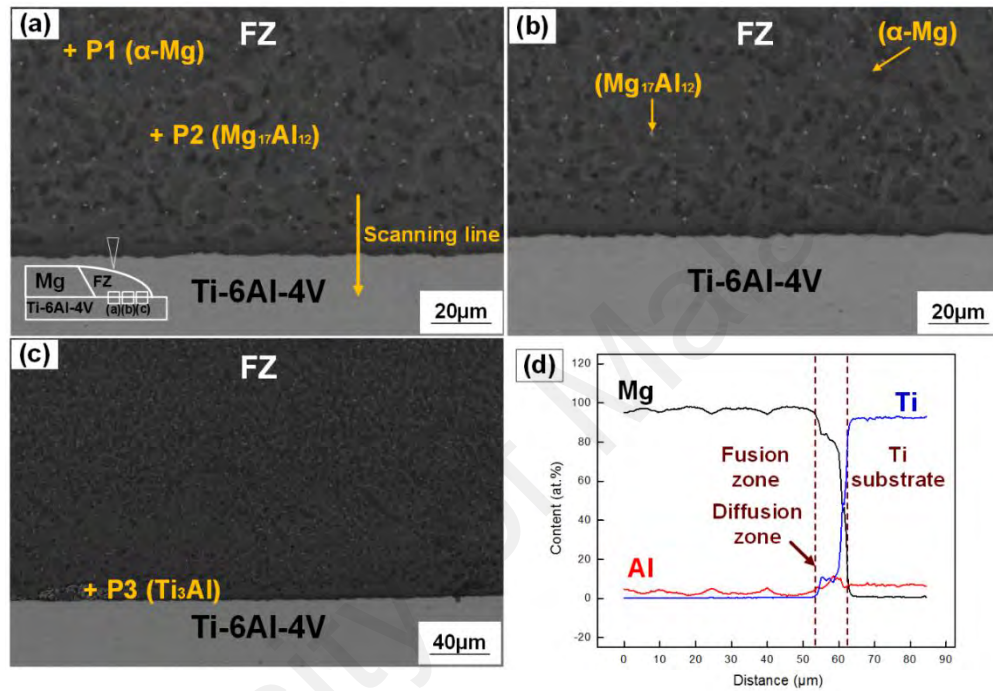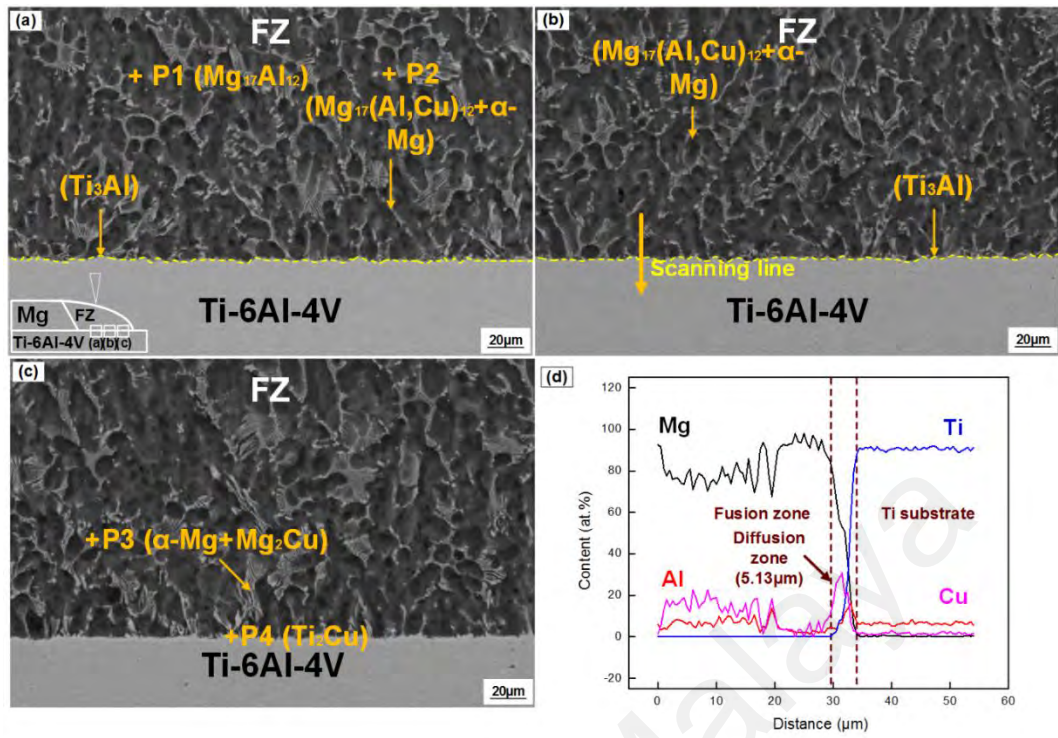**Figure 4.37: SEM morphologies of the Cu added joint: (a) direct irradiation area; (b) middle area; (c) weld toe area; (d) line scan of b.**
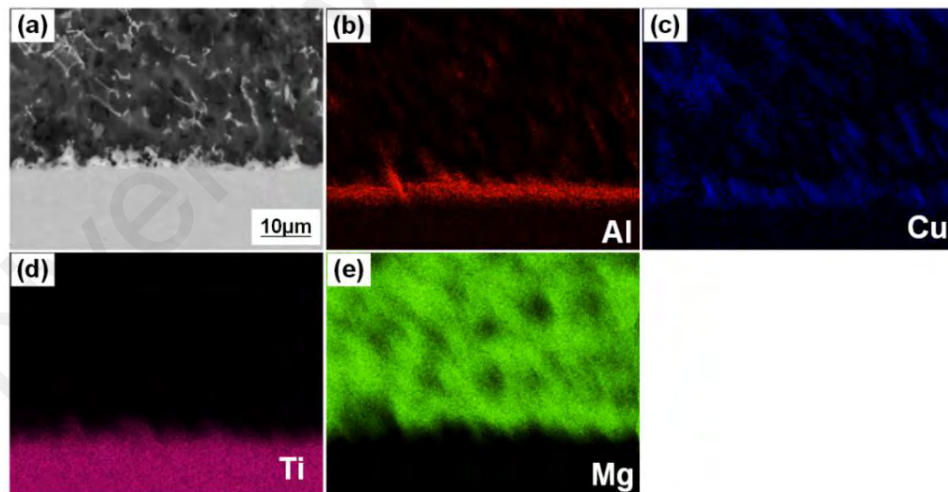
Figure 4.38: EDS mapping of Cu added joint at the middle area: (a) corresponding SEM image, (b)-(e) Al, Cu, Ti, Mg.

Table 4.11: EDS results of various points presented in Figure 4.37 (at.%).

Point	Mg	Al	Ti	Cu	Possible phases
1	89.42	10.58	---	---	$Mg_{17}Al_{12} + \alpha\text{-}Mg$
2	73.77	16.77	0.17	9.29	$\alpha\text{-}Mg + Mg_{17}(Al,Cu)_{12}$
3	71.82	15.87	0.10	12.21	$\alpha\text{-}Mg + Mg_2Cu$
4	---	15.21	52.92	31.87	Ti_2Cu
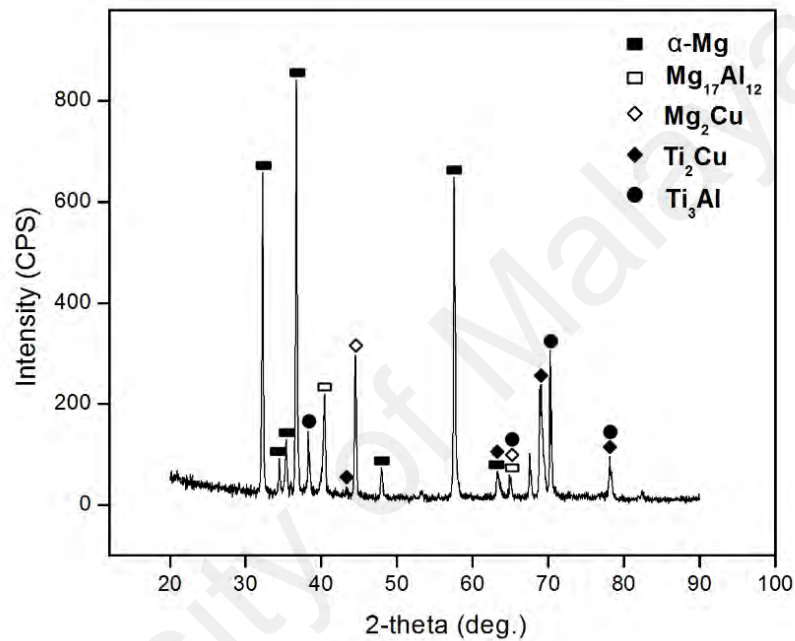
Figure 4.39: XRD analysis of the Cu added joint.

4.3.3.4 Cu-Ni coated joint

According to the results presented above, it was noted that Cu coated joint had relatively smooth interface, whereas Ni coated joint had thick interfacial reaction layer. Thus, to obtain interfacial reaction between Mg and Ti and also to minimize the thickness of the IMCs layer, which was crucial in realizing joint with best mechanical resistance, the benefit of using Cu-Ni layer was explored. Figure 4.40 shows the SEM images of Cu-Ni added joint. An EDS analyses were also performed and the results are presented in

Table 4.12. Despite the used of the two kind of coatings, the deposited layers were not visible after the LWB process, suggesting suitable heat input used in the current study.

At the FZ far from the interface of direct irradiation region gray phases (P1 in Figure 4.40a) was $Mg_{17}Al_{12}$. Along the entire brazed interface, mingled IMCs containing light gray (P2 in Figure 4.40a) with some dark gray phases (P3 in Figure 4.40a) were observed. According to the EDS results, the light gray was characterized as Ti_2Ni. Meanwhile, the dark gray consisted of 29.66 at.% Al, 61.87 at.% Ti, 6.10 at.% Ni, 2.12 at.% Cu, which were identified as Ti_3Al based on the previous analysis. However, compared with Ni coated joint, the thickness of this mingle structure was thinner. EDS line scanning was performed at the direct irradiation region as shown in Figure 4.40(e). Al and Ni elements gathered at the interface, suggesting the Ti-Ni and Ti-Al IMCs formation, whereas, the small Cu segregation could be associated with Mg-Cu phase adhered to the fusion zone-Ti brazed interface. Zhang et al. (2018c) demonstrated that Cu element could promote Al and Ti atoms mutual diffusion. Thus, the Ti_3Al interfacial reaction layer dominated the mingle structure (Ti_2Ni and Ti_3Al). Interestingly, compared to Ni coated joint with diffusion zone of 38.95 μm, the diffusion zone of Cu-Ni joint was reduced to 9.14 μm, which was beneficial to the joint mechanical resistance. At the FZ of the middle region, precipitation of second phase (P4) increased. This phase was identified as $Mg_{17}(Al,Cu)_{12}$ owing to the limited Cu content (Du, 2013). The microstructure of the weld toe region contained some bulk phases (P5 in Fig. 14c) in the FZ. This phases contained 49.73 at.% Al, 19.45 at.% Mg, 27.24 at.% Ni, 3.45 at.% Cu, which were ascertained as Mg-Al-Ni phases. Nearby the interface, dendritic structures (P6 in Figure 4.40d) distributed around the α-Mg sold-solution as shown in the high magnification image Figure 4.40(d). The dendritic structures contained 16.11 at.% Al, 71.00 at.% Mg and 11.99 at.% Cu which was identified as α-Mg+Mg_2Cu. This phenomenon was also reported by Wang et al. (2016) for MIG welded Mg/steel using copper interlayer. As shown in Figure 4.40(d),

continuous Ti$_3$Al formed below the mingle structure was observed. The EDS mapping results (Figure 4.41) of Ti, Ni, Cu, Mg and Al at the weld toe region verified this assertions.

To further verify the reaction products produced along the interface, XRD analysis was conducted. The result shown in Figure 4.42 confirmed that diffraction peaks of Ti$_3$Al, Ti$_2$Ni, and Mg$_2$Cu phases were detected, which was in agreement with the EDS analysis given in Table 4.12.
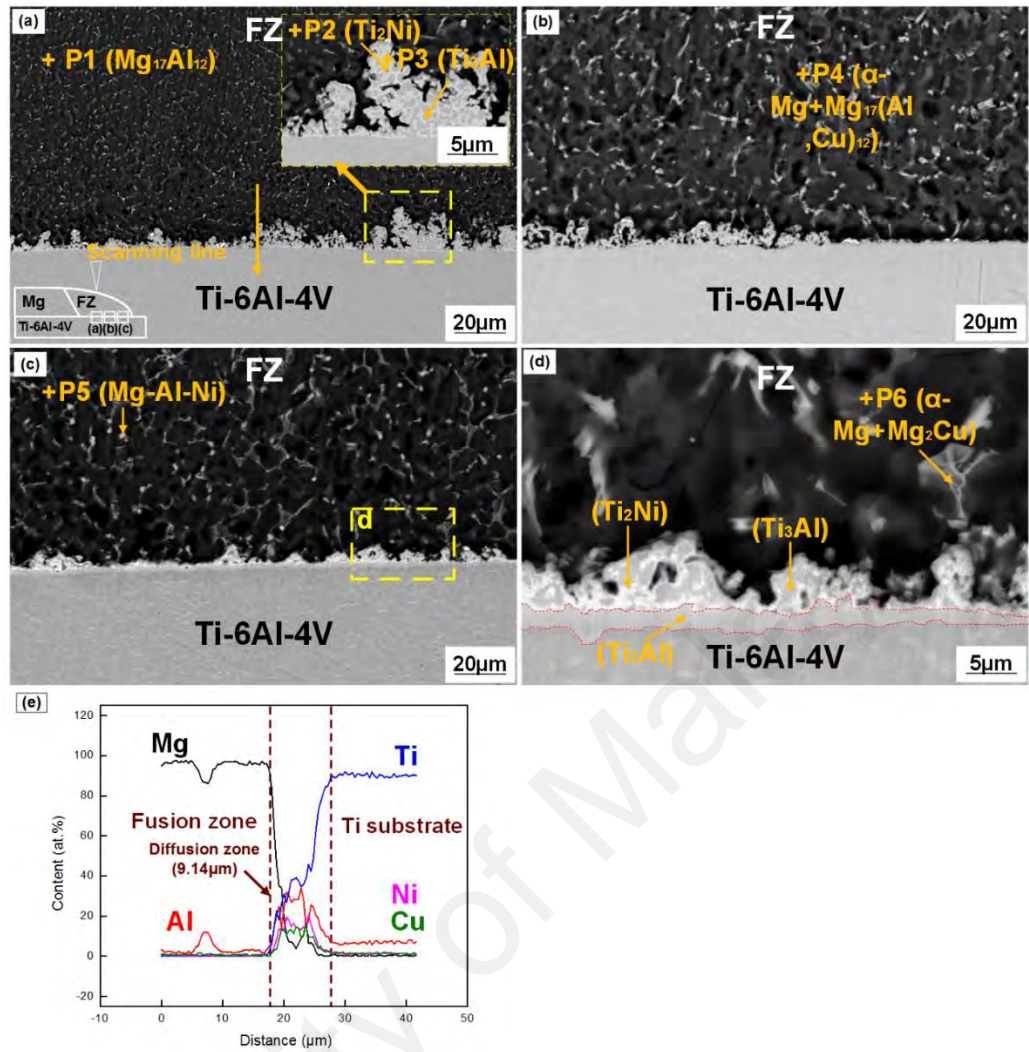
Figure 4.40: Interfacial microstructure morphologies of the Cu-Ni added joint: (a) direct irradiation area; (b) middle area; (c) seam toe area; (d) higher magnification of region d; (e) line scan of a.

Table 4.12: EDS results of various points presented in Figure 4.40 (at.%).

Point	Mg	Al	Ti	Ni	Cu	Possible phases
P1	68.56	29.06	---	0.39	1.99	$Mg_{17}Al_{12}$ + α-Mg
P2	0.40	33.07	42.31	19.84	4.38	Ti_2Ni
P3	0.25	29.66	61.87	6.10	2.12	Ti_3Al
P4	79.64	13.57	0.14	0.30	6.35	$Mg_{17}(Al,Cu)_{12}$ + α-Mg
P5	19.45	49.73	0.13	27.24	3.45	Mg-Al-Ni
P6	71.00	16.11	0.90	---	11.99	α-Mg + Mg_2Cu
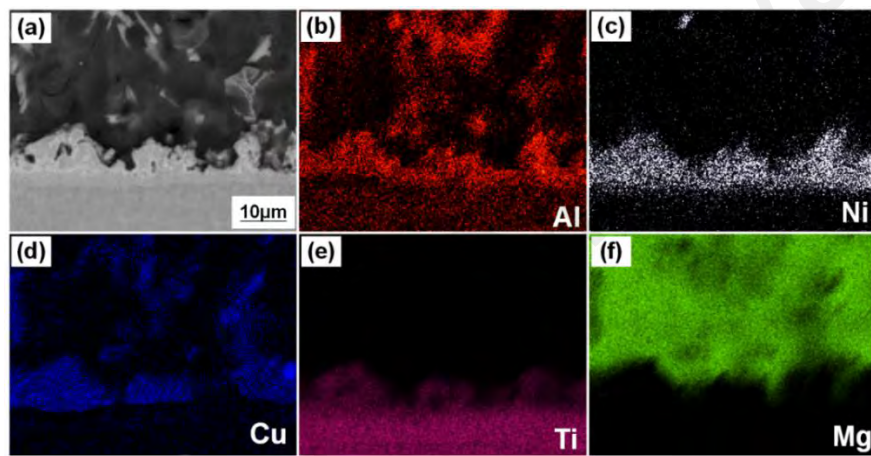
Figure 4.41: EDS mapping of Cu-Ni added joint at the weld toe area: (a) corresponding SEM image, (b)-(f) Al, Ni, Cu, Ti and Mg.
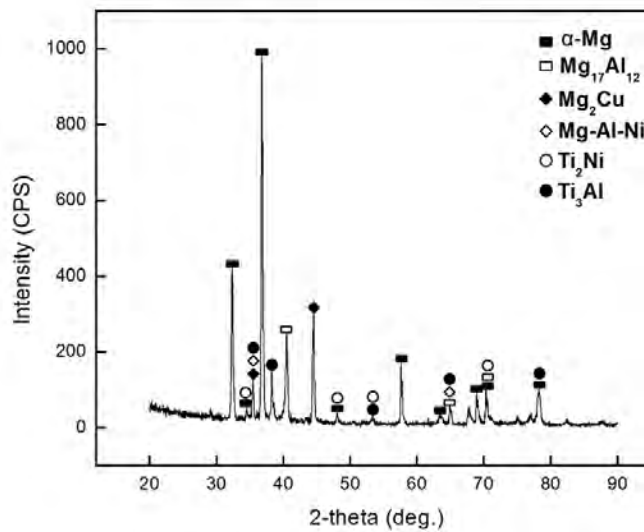
Figure 4.42: XRD results of Cu-Ni added joint.

4.3.4   Joining mechanisms

4.3.4.1 Uncoated joints

Based on the microstructural analyses in Figure 4.34, the joining mechanism of uncoated joint was established as illustrated in Figure 4.43. During heating stage, the filler and Ti sheet were irradiated by the laser beam. At high temperature, the filler melted, while the Ti atoms was activated and dissolved into the filler as demonstrated in Figure 4.43(a). The effect of chemical potential caused the Al atoms from the filler to diffuse toward the interface and reacted with Ti atoms as demonstrated in Figure 4.43(c). The dissolution of the Ti into the filler could increase the Ti molar fraction adjacent to the interface and decrease the Al chemical potential, which accelerated the diffusion of Al into the interface (Chen *et al.*, 2010).

Upon cooling, Ti_3Al interfacial reaction layer formed when the temperature dropped to 1180˚C as schematically shown in Figure 4.43(d). At 650˚C the filler began to solidify and eutectic reaction occurred at 325˚C with newly formed (α-Mg+$Mg_{17}Al_{12}$) structure (Figure 4.43e).
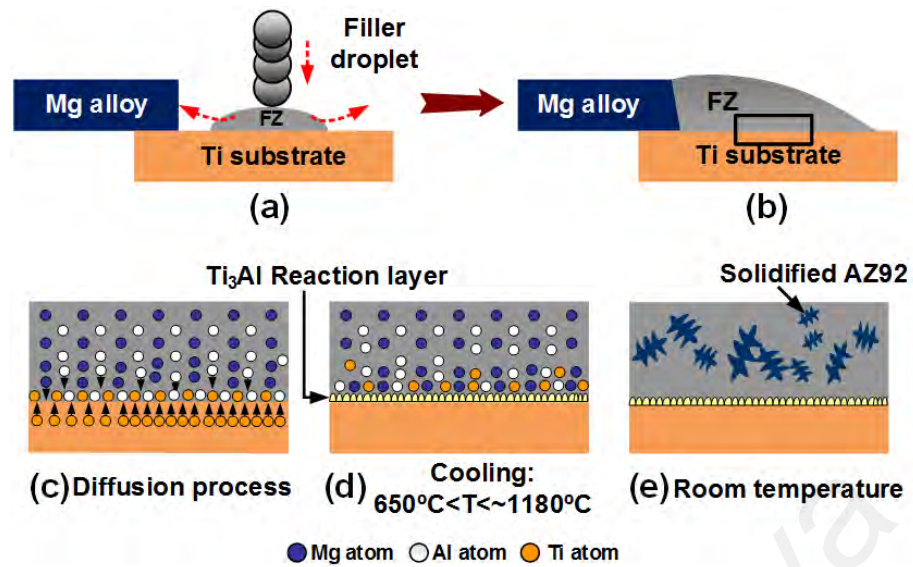
Figure 4.43: Schematic illustrations of bonding mechanism of the uncoated joint: (a)-(b) heating process, (c) atomic diffusion, (d)-(e) solidification behavior with the decrease in temperature.

4.3.4.2 Ni coated joints

According to the microstructural analyses in Figure 4.35, the joining mechanism of Ni coated joint was established as illustrated in Figure 4.44. During heating stage, the Ni coated layer melted and wetted the surface of the Ti substrate, which resulted in improving the wettability of the liquid filler as illustrated in Figure 4.44(a). At high temperature, Ti surface came in contact with molten filler and part of it became active (Figure 4.44b), the Al and Ni atoms in the FZ diffused into Ti substrate and reacted with Ti atoms.

Upon cooling, Ti_3Al interfacial reaction layer formed when the temperature dropped to 1180˚C as shown in Figure 4.44(c). As the temperature dropped to 984˚C, Ni atoms diffused into Ti substrate continuously dispersing around the Ti_3Al IMC, which resulted in the formation of Ti_2Ni as illustrated in Figure 4.44(d). Further decrease of temperature to about 700˚C, caused the Mg, Al and Ni atoms to concentrate in the FZ and Mg-Al-Ni phase was produced (Raghavan, 2009). With further decrease in temperature, at 650˚C

the filler began to solidify and eutectic reaction occurred at 325°C with newly formed (α-Mg+Mg$_{17}$Al$_{12}$) structure as shown in Figure 4.44(e).

Figure 4.44: Schematic illustration of bonding mechanism of Ni coated joint: (a) heating process; (b) atomic diffusion; (c)-(e) solidification behavior with the decrease in temperature.

4.3.4.3 Cu coated joints

According to the microstructural analyses in Figure 4.37, the bonding mechanism of laser welded-brazed Mg/Cu coated Ti was established as illustrated in Figure 4.45. At the heating stage, the laser beam irradiated on the Mg filler metal and it first melted. The molten Mg based filler then dropped on Cu coating layer and spread out as illustrated in Figure 4.45(a). The violent stirring caused the Cu coating to dissolved completely into the liquid filler at both direct irradiation and middle regions, whereas, the Cu atoms at the

weld toe region melted slowly, due to lower temperature and weak stirring. As the welding continued, the Ti surface was indirect contact with liquid filler at direct irradiation and middle regions. The Al atoms in the molten filler dissolved into the Ti substrate. Furthermore, at high temperature, part of the Ti atoms became active and diffused into the molten pool (Figure 4.45b).

During cooling, Ti_3Al was firstly precipitated along the interface at both direct and middle regions as the temperature dropped to 1180˚C as illustrated in Figure 4.45(c) in accordance with Ti-Al binary phase diagram. At the weld toe region, only Ti_2Cu IMC was formed as the temperature dropped below 980˚C (Massalski *et al.*, 1986), owing to the insufficient Al and Ti diffusion force (Figure 4.45d). At 487˚C, the diffused Cu atoms formed eutectic reaction with Mg atoms (α-Mg+Mg_2Cu). Lastly, $Mg_{17}(Al,Cu)_{12}$ was formed with further decreased in temperature (Figure 4.45e).
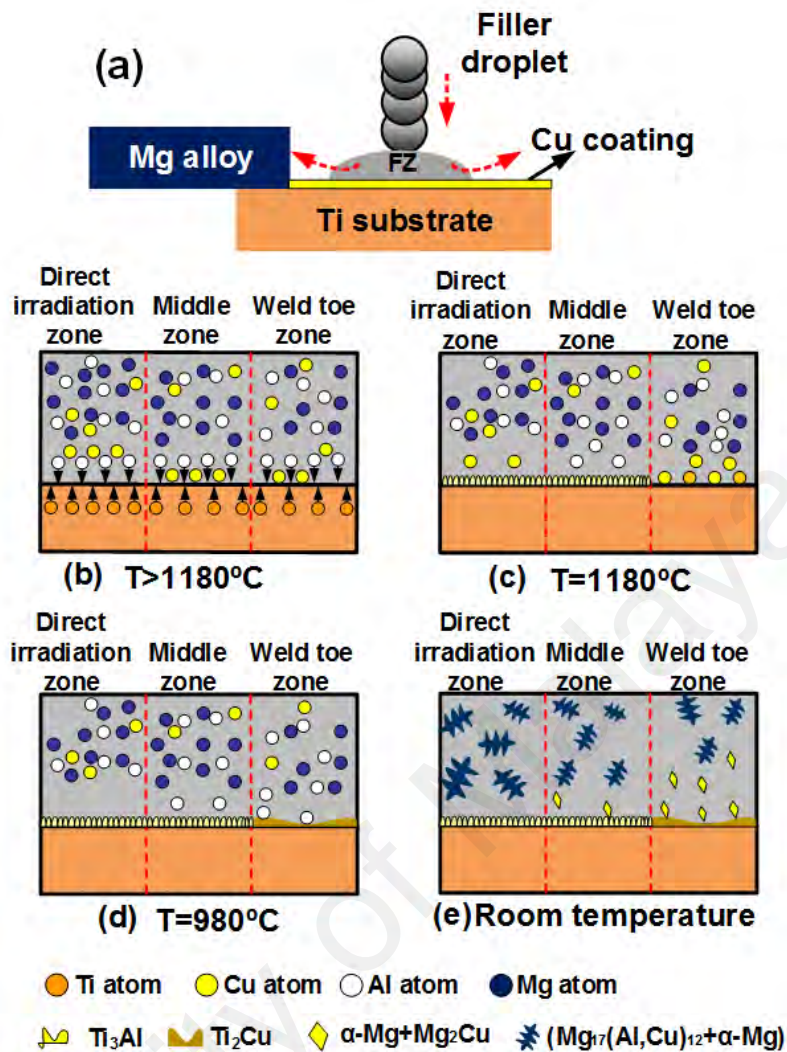
Figure 4.45: Schematic illustrations of joining mechanism of the Cu added joint: (a) heating process; (b) atomic diffusion; (c)-(e) solidification behavior with the decrease in temperature.

4.3.4.4 Cu-Ni coated joints

Based on the microstructural analyses in Figure 4.40, the bonding mechanism of Cu-Ni coated joint is proposed as schematically illustrated in Figure 4.46. During heating stage, the filler melted and the Cu-Ni layer melted and wetted the surface of the Ti substrate (Figure 4.46a). The violent stirring caused the Cu-Ni layer dissolved into the molten pool. At high temperature, the Ti surface was in-contact with liquid filler and part of it became active. Thus, the Al, Cu and Ni atoms in the FZ diffused to Ti substrate and reacted with Ti atoms.

Upon cooling, Ti_3Al interfacial reaction layer formed when the temperature dropped to 1180°C as shown in Figure 4.46(c). At low heat input (<1500W), Al diffused faster than Ni atoms (Tan *et al.*, 2018a). Thus, continuous Ti_3Al IMCs evolved across the brazed interface. As the temperature dropped to 984°C or below, Ni atoms diffused into Ti substrate continuously dispersing around the Ti_3Al IMC, which resulted in the formation of Ti_2Ni as shown in Figure 4.46(d). Further decreased in temperature to about 700°C, caused the Mg, Al and Ni atoms to concentrate in the FZ and Mg-Al-Ni phase was formed (Figure 4.46e) in accordance with Al-Mg-Ni ternary phase diagram (Raghavan, 2009). At 487°C, the diffused Cu atoms formed eutectic reaction with Mg atoms (α-Mg+Mg_2Cu), whereas, $Mg_{17}(Al,Cu)_{12}$ was formed with further decrease in temperature (Figure 4.46f).

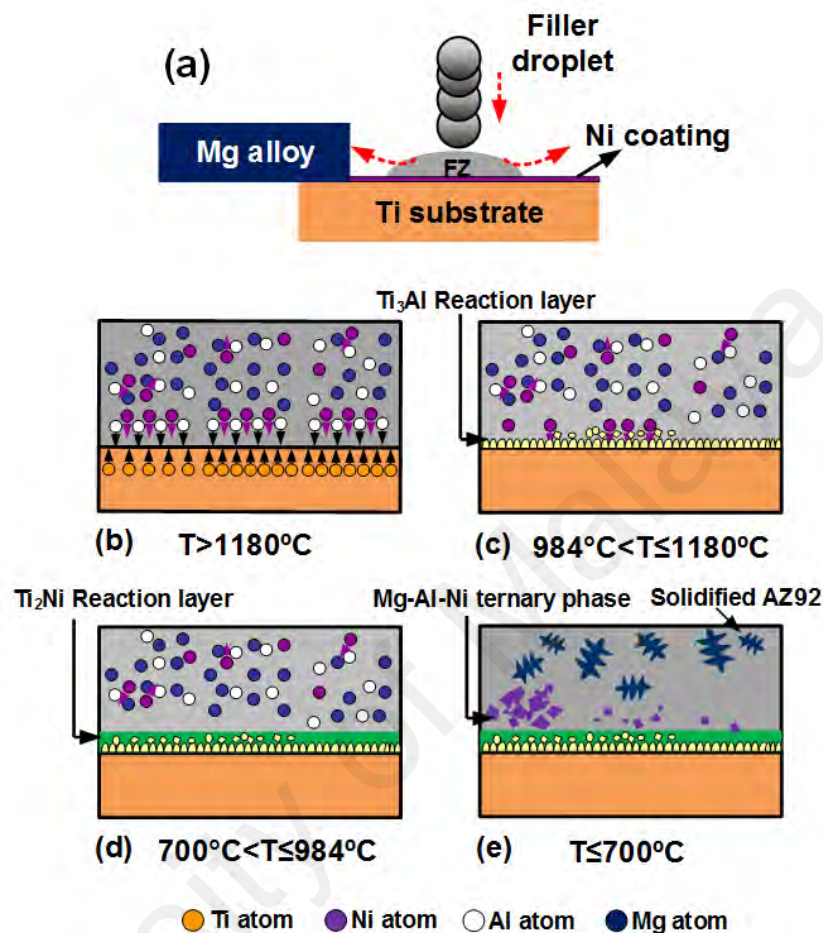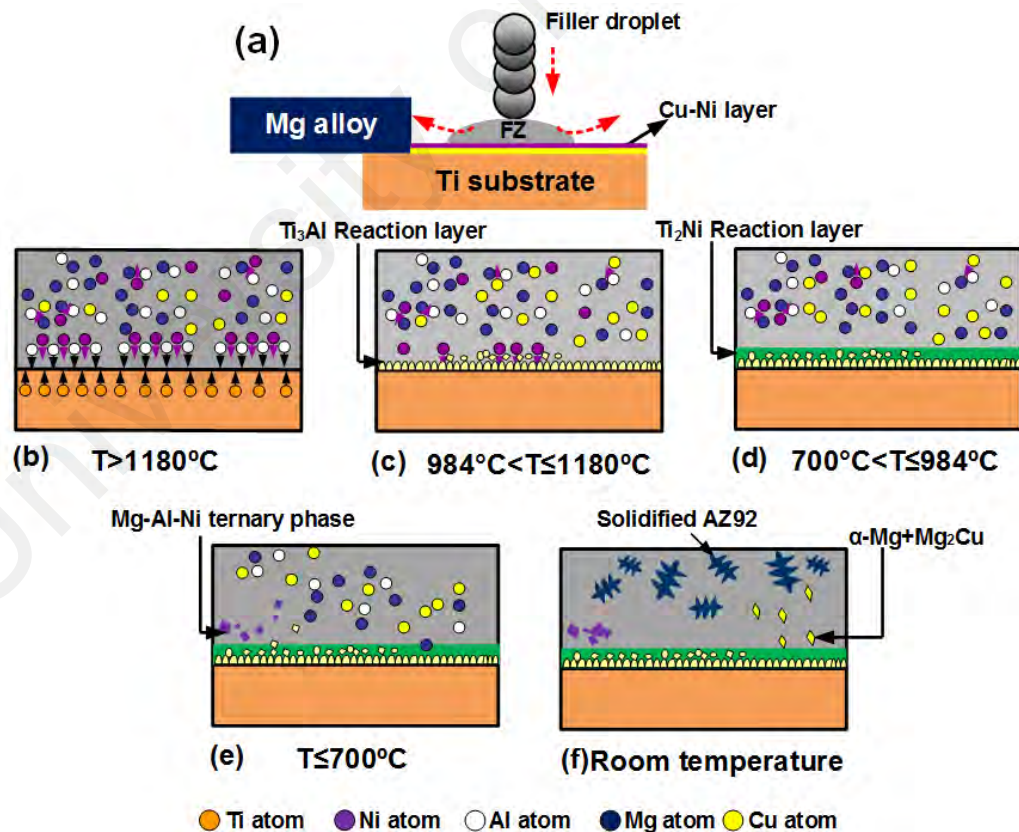**Figure 4.46: Schematic illustration of bonding mechanism of Cu-Ni coated joint: (a) heating process; (b) atomic diffusion; (c)-(f) solidification behavior with the decrease in temperature.**

4.3.5   The function of intermediate elements

According to the results presented, Al in the Mg-Al brazing alloy has great influence on the Mg/Ti joint formation. For instance, Al has a low melting point of 660˚C, suggesting that it could be melted at low heat input and mitigated the severe vaporization of the filler alloy (Tan *et al.*, 2013). In addition, interfacial reaction between the Ti and Al could interact easily to produce Ti-Al phase at the interface. Furthermore, because of the large solid-solubility of Al in Mg, it could be added into the filler in the same manner to Al based filler (Song *et al.*, 2009). Based on the thermodynamic theory, the driving force for Al atoms diffusion from the braze alloy to the interface was the chemical potential gradient and hence induced the chemical reaction (Tan *et al.*, 2018a). It has been demonstrated in this study that the presence of alloying elements such as Cu and Ni influenced the interfacial reaction of Ti/Al. For instance, Ni and Al was observed to have similar promoting effect on the Mg-Ti system, whereas, Cu addition promoted the mutual diffusion between the Ti and Al atoms. Thus, the interfacial bonding of Mg/Ti could be transformed by controlling mutual diffusion process, which could be achieve by controlling the heat input of welding parameter and the content of the interlayer elements (Chen & Nakata, 2009).

4.3.6   Hardness characteristics

The hardness distribution of Mg/Ti joints welded with different coatings is presented in Figure 4.47. The hardness distribution is in good agreement with the microstructure variations presented in section 4.3.4 for the various joints. The results showed that the average hardness of the FZ and Ti substrate was 70 HV and 328 HV, respectively for coated joints compared to 58 HV and 316 HV for uncoated joint. Furthermore, the presence of Mg-Al-Ni ternary phase near the interface of both Ni coated and Cu-Ni coated joints caused the hardness value to slightly increase. Similar phenomenon was reported

by Chatterjee et al. (2006) when welding Ti with Ni. In contrast, the formation of thin Ti₃Al IMC resulted in no obvious increased in hardness near the interface for both the uncoated and Cu coated joints.
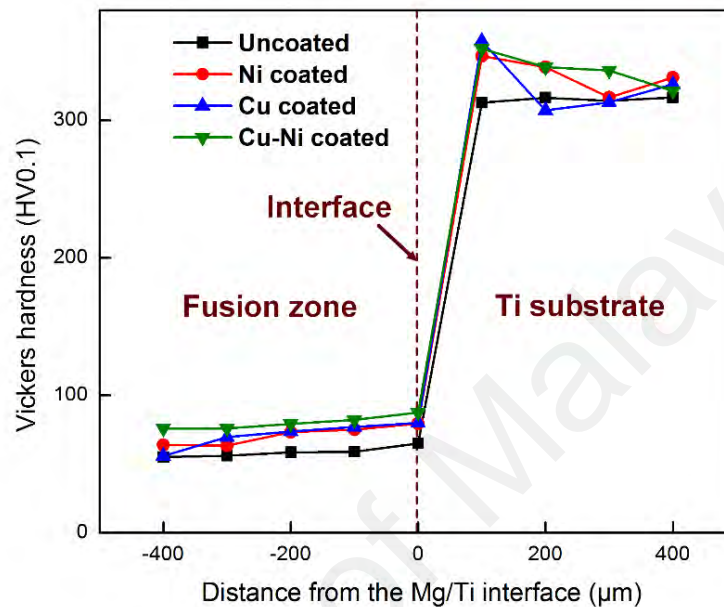
Figure 4.47: Comparison of hardness profiles across the laser welded-brazed Mg/Ti at various coating conditions.

4.3.7 Tensile-shear performance

The fracture loads and fracture location of the joints for different coating type is shown in Figure 4.48. Compared with uncoated joint, the fracture load of the various coatings was higher. For instance, the tensile shear fracture load of Cu coated joint attained 1680 N, about 70% higher than that of uncoated joint. The higher joint strength obtained could be associated with enhancement of Al and Ti atoms mutual diffusion by the Cu atoms and the formation of Ti₂Cu IMC at the interface. Nevertheless, Mg and Ti have huge discrepancies in their thermal expansion coefficient and thermal conductivity, which resulted in easy generation of welding residual stress as reported in previous study (Zhang

et al., 2018c). Thus, the non-uniform and non-continuous Ti_2Cu IMC formed along the weld toe region (Figure 4.37c) may cause stress concentration, which deteriorated the tensile shear load and resulted in interfacial failure. Thus, the Mg/Cu coated Ti joint performance was lower compared to Ni and Cu-Ni coated joint. In comparison, the Ni coated joint has an average tensile shear fracture load of 1795 N, approximately 82% higher than the uncoated joint. The higher mechanical resistance obtained was attributed to the formation of Ti-Al and Ti-Ni IMCs across the brazed interface, which hindered crack propagation and improved the interfacial bonding. However, the thickness of the mingle structure (Ti_3Al and Ti_2Ni) was more than critical value of 10 µm (Laukant et al., 2005), thus adversely affected the joint performance. In contrast, Cu-Ni coated joint presented the highest tensile shear fracture load. The higher joint strength obtained could be associated with enhancement of Al and Ti atoms mutual diffusion by the Cu atoms and the formation Ti-Ni IMC at the interface. Moreover, as shown in Figure 4.40(e) the thickness of this mixed IMC layer was less than the critical value (Laukant et al., 2005), which could enhance the joint tensile strength. The tensile shear performance attained a maximum value of 2014 N, i.e. about 100% higher than the fracture load of the uncoated joint.
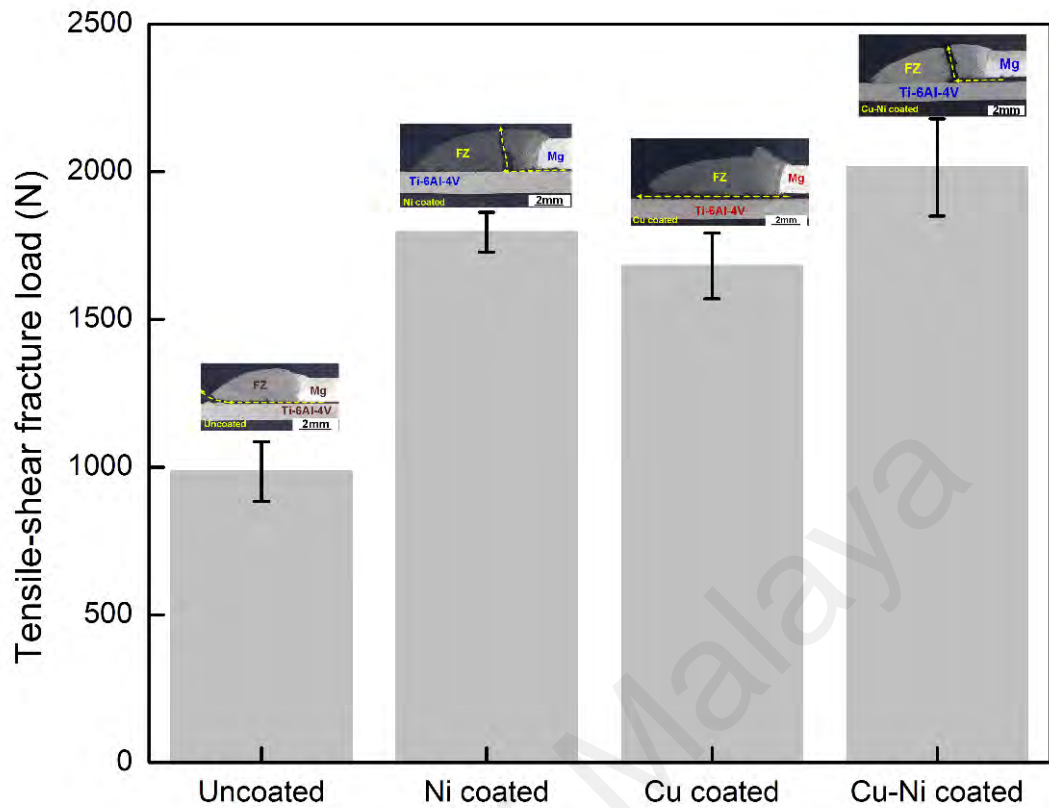
Figure 4.48: Tensile-shear fracture loads and fracture location of Mg/Ti under various coating conditions.

4.3.8 Fracture surface analysis

The fracture surfaces of the various joints after tensile testing is shown in Figure 4.49. The uncoated and Cu coated joints fractured at the interface as presented in Figure 4.48. However, the feature of fracture surface of the uncoated joint at the Ti side was characterized by fine particles attached with few residual Mg as shown in Figure 4.49(a). These fine particles consisted of mainly 28.49 at.% Al, 71.51 at.% Ti, confirming the formation of Ti$_3$Al. In contrast, the Mg/Cu coated Ti fracture surfaces characteristic exhibited tear ridges (Figure 4.49c), demonstrating severe deformation happened during tensile-testing. Ti$_3$Al particles were distributed in the residual α-Mg as confirmed by EDS result, which was beneficial for preventing fracture (Tan *et al.*, 2018a). On the hand, as

for the Ni and Cu-Ni coated joints that fractured at the FZ, the fracture surface exhibited a typical dimple feature as indicated in Figure 4.49(b and d).
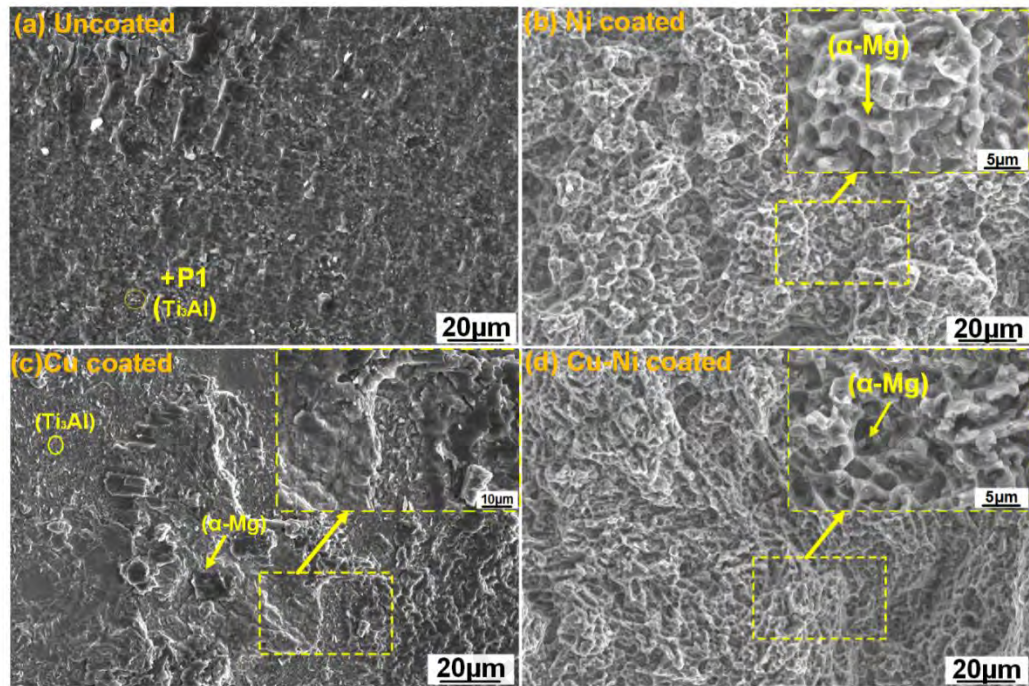
Figure 4.49: SEM morphologies of fracture surfaces of the various joints: (a) Uncoated; (b) Ni coated; (c) Cu coated and (d) Cu-Ni sandwich coated.

CHAPTER 5: CONCLUSIONS

5.1   Conclusions

A fiber laser welding-brazing method has been developed for welding AZ31/Ti64 via electrodeposited Cu-Ni layer. The interfacial microstructure morphologies were characterized and identified. Numerical simulation of the temperature field was performed to assist in analyzing the phase evolution during the LWB process. The mechanical properties of the joints were evaluated. The bonding mechanism was also discussed. The major conclusions of this study can be summarized as follows:

1. The effect of copper-nickel interlayer arrangements on laser welded-brazed AZ31/Ti64 lap joints showed that successful joints were achieved in both cases. Increasing heat input contributed to the enhancement of the wetting of the filler on the Ti sheet. When the laser power was in the range of 1200-1600 W, 0.3 m/min welding speed, +30 mm defocused distance and 20 L/min flow rate of Ar shielding gas, an excellent wetting with uniform brazed area of the base metals was achieved.

2. Depending on the interlayer arrangements chosen, different reactions layers formed inside the joint region. Nevertheless, at optimum heat input (1400 W), the dissolution of the coating layer resulted in the formation of new Ti_2Ni mingled with Ti_3Al interfacial reaction products along the fusion zone (FZ)-Ti brazed interface in both interlayer arrangements.

3. The formation of the Ti_2Ni and Ti_3Al mixed IMC layer at the brazed interface resulted from the inter-diffusion between Al/Ti and Ti/Ni during the LWB process was responsible for the formation of metallurgical bond. In addition, the Cu coating on the Ti sheet does not appear at the brazed interface of the titanium and the AZ92 filler alloy. Instead, its primary role is to prevent oxidation of the Ti surface until the filler can come into direct contact with the

titanium surface and also promote mutual diffusion between Ti and Al. Thus, metallurgical bonding rather than mechanical bonding was achieved at the Mg/Ti interface. Therefore, using Cu-Ni layer is recommended for dissimilar joining of Mg/Ti sheet.

4. A temperature field numerical analysis using MSC Marc software was used to investigate the phase evolution between the Cu-Ni coated Ti and the AZ92 Mg alloy during the LWB process. The calculations were made at optimum heat input at direct irradiation, middle and weld toe regions of the joint. The formation of Ti_3Al, Ti_2Ni, Mg-Al-Ni ternary phase, Mg-Cu eutectic structure and Mg-Al eutectic were confirmed at the three calculated regions, which was in accordance with experimental results. However, the actual IMCs products were limited by other conditions, such as welding method and alloying element content.

5. The average fracture load of 10 mm wide transverse tensile-shear specimens taken from the joints reached 2016.5 N for AZ31/Ni-Cu/Ti64 and 2014.6 N for AZ31/Cu-Ni/Ti64 at laser power of 1400 W, demonstrating joint efficiency of 71% compared to AZ31 alloy. Depending on the heat input, two fracture modes were observed. At the optimum heat input, the joint failed at the fusion zone of magnesium base metal, whereas, interfacial failure was observed at lower/higher heat input. For joints fractured at the interface, tear ridge was seen at fracture surface whereas dimple-like features were observed at the FZ fracture surfaces.

6. The effect of the electrodeposited Cu and Ni contents on microstructure development and joint fracture load were also analyzed. The reaction products were influenced by the interlayer elements contents. For the joint in which the Ni coating (15.36 μm) was thicker than the Cu coating (5.47 μm), thick Ti_3Al

and Ti_2Ni mixed interfacial reaction products were produced along the entire brazed interface. Similarly, Ti_2Ni mingled with Ti_3Al interfacial reaction products also evolved from the direct irradiation zone to the weld toe zone of the joint with comparable Ni and Cu coating thicknesses (10.78 μm Cu-9.30 μm Ni). In this case, the thickness of this mixed layer was less than the critical thickness of 10 μm. For the joint in which the Cu coating is much higher than the Ni coating thickness (17.12 μm Cu-4.23 μm Ni), Ti_3Al and Ti_2Ni was formed at the brazed joint interface of direct irradiation zone, whereas, only Ti_3Al was formed at the middle zone. At the weld toe zone, Ti_2Cu uneven interfacial reaction layer was observed.

7. The maximum tensile-shear fracture load attained 2020 N for the joint with comparable Cu and Ni thicknesses. The tensile-shear investigation further revealed that the joint would fracture at the fusion zone when the coating thickness of Ni was comparable or higher than Cu. In contrast, interfacial failure was observed when the thickness of Cu was much higher than the Ni.

8. The effect of the Cu, Ni and Cu-Ni coatings on the Mg/Ti lap joints formation were studied under similar welding and electrodeposition conditions. It was found that compared with uncoated joint, better joints appearances were observed with additions of various coatings, suggesting that the presence of coating could improve the wettability of the liquid filler on the Ti substrate.

9. The different coating condition resulted in the obvious differences in the brazed side of the joint. The interfacial microstructural evolution showed that for the uncoated joint, only Ti_3Al phase formed along the entire brazed interface. In comparison, Ti_3Al phase was observed at direct irradiation and middle regions, whereas, Ti_2Cu phase was produced at the weld toe region of Cu added joint. For Ni and Cu-Ni added joints, Ti_2Ni mingled with Ti_3Al interfacial reaction

products evolved from the direct irradiation region to the weld toe region. Interestingly, the thickness of the mixed reaction layer for Cu-Ni added joint was less than the critical thickness of 10 μm.

10. The Cu-Ni added joint sustained the highest tensile-shear fracture load of 2014 N (representing 100% higher than that of the uncoated joint), followed by the Ni added and Cu added joint joints with 1795 N and 1680 N, respectively. The fracture mode of the uncoated and Cu added joints was interfacial failure, whereas, FZ fracture with typical dimple feature was observed for both Ni and Ni-Cu added joints.

5.2   Suggestions for further work

This research has demonstrated that metallurgical bonding with superior mechanical resistance between Mg/Ti could be achieved using LWB technique with addition of electrodeposited Cu-Ni layer. However, further work needs to be conducted for the technique to be fully implemented in actual production line for joining Mg/Ti hybrid structures. The following suggestions are made:

1. Using appropriate surface treatments of the T64 in order to achieve the composite coatings will enhance the adhesion at the Ti64/Cu-Ni interface before the LWB process. Therefore, the feasibility of using different advanced coating techniques such as vapor phase coating which can improve the interfacial bonding on the Ti substrate is suggested. To further enhance the diffusion at Ti-interlayer and easily control the interlayer thickness.

2. Thermodynamic analysis should be conducted to provide better understanding of the interfacial reaction products formed and the diffusion behavior during LWB process.

3. The study should be extended to examine the effect of the Cu-Ni coating layer on different magnesium alloys to other types of the titanium alloys or immiscible systems such as Mg alloys to various grades of steels that's required in the industry in order to develop functionally graded materials that can be used in a variety of engineering applications.

4. Additional mechanical assessment methods such as corrosion, impact and fatigue tests should be carried out. In order to provide a comprehensive understanding of the reliability of the joint and develop adequate protection measures.

REFERENCES

Aghion, E., & Bronfin, B. (2000). *Magnesium alloys development towards the 21st century.* Paper presented at the Materials Science Forum.

Ahn, J., Chen, L., Davies, C., & Dear, J. (2016). Parametric optimisation and microstructural analysis on high power Yb-fibre laser welding of Ti–6Al–4V. *Optics and Lasers in Engineering, 86*, 156-171.

Amaya, J. S., Titania, E. Y., & BOTANA, F. (2013). Laser welding of light metal alloys: aluminium and titanium alloys. *Handbook of Laser Welding Technologies*, 215-254.

Amer, A. E., Koo, M. Y., Lee, K. H., Kim, S. H., & Hong, S. H. (2010). Effect of welding heat input on microstructure and mechanical properties of simulated HAZ in Cu containing microalloyed steel. *Journal of Materials Science, 45*(5), 1248-1254.

Aonuma, M., & Nakata, K. (2009). Effect of alloying elements on interface microstructure of Mg–Al–Zn magnesium alloys and titanium joint by friction stir welding. *Materials Science and Engineering: B, 161*(1), 46-49.

Aonuma, M., & Nakata, K. (2010). Effect of calcium on intermetallic compound layer at interface of calcium added magnesium–aluminum alloy and titanium joint by friction stir welding. *Materials Science and Engineering: B, 173*(1), 135-138.

Aonuma, M., & Nakata, K. (2012). Dissimilar metal joining of ZK60 magnesium alloy and titanium by friction stir welding. *Materials Science and Engineering: B, 177*(7), 543-548.

Atieh, A. M. (2013). Transient Liquid Phase Diffusion Bonding of Magnesium Alloy (Mg-AZ31) to Titanium Alloy (Ti-6Al-4V).

Atieh, A. M., & Khan, T. I. (2013). Effect of process parameters on semi-solid TLP bonding of Ti–6Al–4V to Mg–AZ31. *Journal of Materials Science, 48*(19), 6737-6745.

Atieh, A. M., & Khan, T. I. (2014a). Application of Ni and Cu nanoparticles in transient liquid phase (TLP) bonding of Ti-6Al-4V and Mg-AZ31 alloys. *Journal of Materials Science, 49*(22), 7648-7658.

Atieh, A. M., & Khan, T. I. (2014b). Effect of interlayer thickness on joint formation between Ti-6Al-4V and Mg-AZ31 alloys. *Journal of Materials Engineering and Performance, 23*(11), 4042-4054.

Atieh, A. M., & Khan, T. I. (2014c). TLP bonding of Ti-6Al-4V and Mg-AZ31 alloys using pure Ni electro-deposited coats. *Journal of Materials Processing Technology, 214*(12), 3158-3168.

Atieh, A. M., & Khan, T. I. (2014d). Transient liquid phase (TLP) brazing of Mg–AZ31 and Ti–6Al–4V using Ni and Cu sandwich foils. *Science and Technology of Welding and Joining, 19*(4), 333-342.

Baeslack, W., & Banas, C. (1981). A comparative evaluation of laser and gas tungsten arc weldments in high-temperature titanium alloys. *Welding Journal, 60*(7), 121.

Baqer, Y. M., Ramesh, S., Yusof, F., & Manladan, S. (2018). Challenges and advances in laser welding of dissimilar light alloys: Al/Mg, Al/Ti, and Mg/Ti alloys. *The International Journal of Advanced Manufacturing Technology*, 1-17.

Blawert, C., Hort, N., & Kainer, K. (2004). Automotive applications of magnesium and its alloys. *Trans. Indian Inst. Met, 57*(4), 397-408.

Boyer, R. R. (1985). Titanium and titanium alloys. *ASM International, ASM Handbook., 9*, 458-475.

Brown, S., & Song, H. (1992). Finite element simulation of welding of large structures. *Journal of engineering for industry, 114*(4), 441-451.

Brunette, D. M., Tengvall, P., Textor, M., & Thomsen, P. (2012). *Titanium in medicine: material science, surface science, engineering, biological responses and medical applications*: Springer Science & Business Media.

Caiazzo, F., Alfieri, V., Corrado, G., Cardaropoli, F., & Sergi, V. (2013). Investigation and Optimization of Laser Welding of Ti-6Al-4 V Titanium Alloy Plates. *Journal of Manufacturing Science and Engineering-Transactions of the Asme, 135*(6).

Caiazzo, F., Alfieri, V., Fierro, I., & Sergi, V. (2014). Investigation and Optimization of Disk-Laser Welding of 1 Mm Thick Ti-6al-4v Titanium Alloy Sheets. *Proceedings of the Asme 9th International Manufacturing Science and Engineering Conference, 2014, Vol 2*.

Campanelli, S. L., Casalino, G., Mortello, M., Angelastro, A., & Ludovico, A. D. (2015). Microstructural characteristics and mechanical properties of Ti6Al4V alloy fiber laser welds. *Procedia CIRP, 33*, 428-433.

Cao, R., Wang, T., Wang, C., Feng, Z., Lin, Q., & Chen, J. H. (2014). Cold metal transfer welding-brazing of pure titanium TA2 to magnesium alloy AZ31B. *Journal of Alloys and Compounds, 605*, 12-20.

Cao, R., Zhu, H., Wang, Q., Dong, C., Lin, Q., & Chen, J. (2016). Effects of zinc coating on magnesium alloy–steel joints produced by cold metal transfer method. *Materials Science and Technology, 32*(18), 1805-1817.

Cao, X., Jahazi, M., Immarigeon, J., & Wallace, W. (2006). A review of laser welding techniques for magnesium alloys. *Journal of Materials Processing Technology, 171*(2), 188-204.

Cao, X., Wallace, W., Poon, C., & Immarigeon, J.-P. (2003). Research and progress in laser welding of wrought aluminum alloys. I. Laser welding processes. *Materials and Manufacturing Processes, 18*(1), 1-22.

Chatterjee, S., Abinandanan, T., & Chattopadhyay, K. (2006). Microstructure development during dissimilar welding: Case of laser welding of Ti with Ni

involving intermetallic phase formation. *Journal of Materials Science, 41*(3), 643-652.

Chen, S.-h., Li, L.-q., Chen, Y.-b., & Liu, D.-j. (2010). Si diffusion behavior during laser welding-brazing of Al alloy and Ti alloy with Al-12Si filler wire. *Transactions of Nonferrous Metals Society of China, 20*(1), 64-70.

Chen, S., Li, L., Chen, Y., Dai, J., & Huang, J. (2011). Improving interfacial reaction nonhomogeneity during laser welding–brazing aluminum to titanium. *Materials & Design, 32*(8-9), 4408-4416.

Chen, Y., & Nakata, K. (2010). Effect of surface states of steel on microstructure and mechanical properties of lap joints of magnesium alloy and steel by friction stir welding. *Science and Technology of Welding and Joining, 15*(4), 293-298.

Chen, Y. C., & Nakata, K. (2009). Effect of tool geometry on microstructure and mechanical properties of friction stir lap welded magnesium alloy and steel. *Materials & Design, 30*(9), 3913-3919.

Clarke, J. (2001). Aluminum tailor-welded blanks for automotive applications. *Minerals, Metals and Materials Society/AIME, Aluminum 2001(USA)*, 117-128.

Cole, G. S. (2003). *Issues that influence magnesium's use in the automotive industry.* Paper presented at the Materials Science Forum.

Cole, G. S. (2016). Summary of "Magnesium vision 2020: A North American automotive strategic vision for magnesium". In *Essential Readings in Magnesium Technology* (pp. 35-40): Springer.

Cook, G. O., & Sorensen, C. D. (2011). Overview of transient liquid phase and partial transient liquid phase bonding. *Journal of Materials Science, 46*(16), 5305-5323.

Costa, A., Miranda, R., Quintino, L., & Yapp, D. (2007). Analysis of beam material interaction in welding of titanium with fiber lasers. *Materials and Manufacturing Processes, 22*(7-8), 798-803.

Davies, G. (2003). Magnesium. Materials for automotive bodies. *vol, 91*, 1327.

Davis, J. (1997). Heat-Resistant Materials,(an ASM Specialty Handbook) ASM International. *Materials Park, OH*.

Destefani, J. D. (1992). *Introduction to titanium and titanium alloys: Properties and selection nonferrous alloys and special purpose materials.* Materials Park, OH: ASM International.

Dilthey, U., Brandenburg, A., Trager, G., Haferkamp, H., & Niemeyer, M. (1999). Laser- and electron beam welding of magnesium alloys. *Materialwissenschaft Und Werkstofftechnik, 30*(11), 682-692.

Du, S., Liu, G., Wang, M. (2013). Microstructure and properties of transient liquid-phase diffusion bonded joint of AZ31B/Cu dissimilar metal. *Chin. J. Nonferrous (In Chinese) Met., 5*, 1255–1261.

Elthalabawy, W. M. (2010). *Diffusion bonding behavior and characterization of joints made between 316L stainless steel alloy and AZ31 magnesium alloy*.

Evtihiev, N. N., Grezev, N. V., Markushov, Y. V., & Murzakov, M. A. (2016). Fiber Lasers Application for Welding of Titanium Alloys With 16 mm Thickness. *Ii Conference on Plasma & Laser Research and Technologies, 747*.

Freer, R. (1982). Solid state diffusion. Some recent developments. *Physics Bulletin, 33*, 367-370.

Frewin, M., & Scott, D. (1999). Finite element model of pulsed laser welding. *WELDING JOURNAL-NEW YORK-, 78*, 15-s.

Froes, F., Eliezer, D., & Aghion, E. (1998). The science, technology, and applications of magnesium. *Jom, 50*(9), 30-34.

Fujii, H., Takahashi, K., & Yamashita, Y. (2003). Application of titanium and its alloys for automobile parts. *Shinnittetsu giho*, 62-67.

Fujii, S., Takahashi, N., Sakai, S., Nakabayashi, T., & Muro, M. (2000). *Develoment of 2D simulation model for laser welding*. Paper presented at the High-Power Lasers in Manufacturing.

Fukumoto, M., Tsubaki, M., Shimoda, Y., & Yasui, T. (2004). Welding between ADC12 and SS400 by means of friction stirring. *WELDING RESEARCH ABROAD, 50*, 50-50.

Gao, M., Wang, Z., Yan, J., & Zeng, X. (2011). Dissimilar Ti/Mg alloy butt welding by fibre laser with Mg filler wire–preliminary study. *Science and Technology of Welding and Joining, 16*(6), 488-496.

Gao, M., Wang, Z. M., Li, X. Y., & Zeng, X. Y. (2012). Laser Keyhole Welding of Dissimilar Ti-6Al-4V Titanium Alloy to AZ31B Magnesium Alloy. *Metallurgical and Materials Transactions a-Physical Metallurgy and Materials Science, 43a*(1), 163-172.

Gao, M., Zeng, X., Tan, B., & Feng, J. (2009). Study of laser MIG hybrid welded AZ31 magnesium alloy. *Science and Technology of Welding and Joining, 14*(4), 274-281.

Gao, X. L., Zhang, L. J., Liu, J., & Zhang, J. X. (2013). A comparative study of pulsed Nd:YAG laser welding and TIG welding of thin Ti6Al4V titanium alloy plate. *Materials Science and Engineering a-Structural Materials Properties Microstructure and Processing, 559*, 14-21.

Haferkamp, H., Niemeyer, M., Schmid, C., Kaese, V., & Cordini, P. (2000). *Laser welding of magnesium alloys–cooling conditions and resulting metallurgical properties magnesium 2000*. Paper presented at the Second International Conference On Magnesium Science and Technology, Dead Sea, Israel.

Handbook, A. (1990). Nonferrous Alloys and Special-purpose Materials, vol. 2. *ASM International, OH*.

Handbook, M. (1982). Vol. 5: Surface Cleaning, Finishing, and Coating. *American Soc. for Metals*, 412-416.

Jiangtao, X., Fusheng, Z., Jinglong, L., & Weidong, H. (2006). Transient liquid phase bonding of magnesium alloy (AZ31b) and titanium alloy (Ti6Al4V) using aluminium interlayer. *Rare Metal Materials and Engineering, 35*(10), 1677.

Kabir, A., Cao, X., Medraj, M., Wanjara, P., Cuddy, J., & Birur, A. (2010). *Effect of welding speed and defocusing distance on the quality of laser welded Ti–6Al–4V.* Paper presented at the Proceedings of the Materials Science and Technology (MS&T) 2010 Conference, Houston, TX.

Kainer, K., & Von Buch, F. (2003). The current state of technology and potential for further development of magnesium applications. *Magnesium-Alloys and Technology*, 1-22.

Karlsson, R., & Josefson, B. (1990). Three-dimensional finite element analysis of temperatures and stresses in a single-pass butt-welded pipe. *Journal of pressure vessel technology, 112*(1), 76-84.

Kawalla, R., Oswald, M., Schmidt, C., Ullmann, M., Vogt, H.-P., & Cuong, N. (2008). New technology for the production of magnesium strips and sheets. *Metalurgija, 47*(3), 195-198.

Kochan, A. (2001). Laser welding adapts to non-linear tailored blanks. *Assembly Automation, 21*(1), 48-51.

Kreimeyer, M., Wagner, F., & Vollertsen, F. (2005). Laser processing of aluminum–titanium-tailored blanks. *Optics and Lasers in Engineering, 43*(9), 1021-1035.

Kuhn, H., & Medlin, D. (2000). ASM Handbook. Volume 8: Mechanical Testing and Evaluation. *ASM International, Member/Customer Service Center, Materials Park, OH 44073-0002, USA, 2000. 998.*

Kulekci, M. K. (2008). Magnesium and its alloys applications in automotive industry. *The International Journal of Advanced Manufacturing Technology, 39*(9-10), 851-865.

Kulkarni, N. (2015). *Study of the Mechanical Performance of Similar and Dissimilar Titanium Alloy Joints Formed by Diffusion Bonding and Friction Stir Welding.*

Kumar, C., Das, M., & Biswas, P. (2015a). A 3-D Finite Element Analysis of Transient Temperature Profile of Laser Welded Ti-6Al-4V Alloy. *Lasers Based Manufacturing*, 421-440.

Kumar, C., Das, M., Paul, C. P., & Singh, B. (2017). Experimental investigation and metallographic characterization of fiber laser beam welding of Ti-6Al-4V alloy using response surface method. *Optics and Lasers in Engineering, 95*, 52-68.

Kumar, D. S., Sasanka, C. T., Ravindra, K., & Suman, K. (2015b). Magnesium and its alloys in automotive applications–a review. *American Journal of Materials Science and Technology, 4*(1), 12-30.

Lakshminarayanan, A., Saranarayanan, R., Srinivas, V. K., & Venkatraman, B. (2015). Characteristics of friction welded AZ31B magnesium–commercial pure titanium dissimilar joints. *Journal of Magnesium and Alloys, 3*(4), 315-321.

Laukant, H., Wallmann, C., Müller, M., Korte, M., Stirn, B., Haldenwanger, H.-G.*, et al.* (2005). Fluxless laser beam joining of aluminium with zinc coated steel. *Science and Technology of Welding and Joining, 10*(2), 219-226.

Lee, K., & Nash, P. (1991). The Al-Ni-Ti system (Aluminum-Nickel-Titanium). *Journal of phase equilibria, 12*(5), 551-562.

Leyens, C., & Peters, M. (2003). *Titanium and titanium alloys: fundamentals and applications*: John Wiley & Sons.

Li, L., Tan, C., Chen, Y., Guo, W., & Mei, C. (2013). CO2 laser welding–brazing characteristics of dissimilar metals AZ31B Mg alloy to Zn coated dual phase steel with Mg based filler. *Journal of Materials Processing Technology, 213*(3), 361-375.

Li, L., Xia, H., Tan, C., & Ma, N. (2018). Influence of laser power on interfacial microstructure and mechanical properties of laser welded-brazed Al/steel dissimilar butted joint. *Journal of Manufacturing Processes, 32*, 160-174.

LI, R.-d., LI, J.-l., XIONG, J.-t., ZHANG, F.-s., Ke, Z., & JI, C.-z. (2012). Friction heat production and atom diffusion behaviors during Mg-Ti rotating friction welding process. *Transactions of Nonferrous Metals Society of China, 22*(11), 2665-2671.

Liu, L. (2010). *Welding and joining of magnesium alloys*: Elsevier.

Luo, A. A. (2002). Magnesium: Current and potential automotive applications. *Jom, 54*(2), 42-48.

Lütjering, G., & Williams, J. C. (2007). Introduction. *Titanium*, 1-14.

Mackerle, J. (2002). Finite element analysis and simulation of welding-an addendum: a bibliography (1996-2001). *Modelling and Simulation in Materials Science and Engineering, 10*(3), 295.

Maldonado-Zepeda, C. (2001). *The effect of interlayers on dissimilar friction weld properties*. National Library of Canada= Bibliothèque nationale du Canada,

Manabe, A. (1999). Weight Reduction of Vehicles and Light Metals. *Zairyo-to-Kankyo, 48*(8), 463-468.

Manladan, S., Yusof, F., Ramesh, S., & Fadzil, M. (2016). A review on resistance spot welding of magnesium alloys. *The International Journal of Advanced Manufacturing Technology, 86*(5-8), 1805-1825.

Marya, M., Edwards, G., Marya, S., & Olson, D. (2001). *Fundamentals in the fusion welding of magnesium and its alloys*. Paper presented at the Proceedings of the seventh JWS international symposium, Kobe.

Massalski, T. B., Murray, J., Bennett, L., & Baker, H. (1986). Binary Alloy Phase Diagrams. Vol. I and II. *American Society for Metals, 1986*, 2224.

Migiakis, K., & Papadimitriou, G. (2009). Effect of nitrogen and nickel on the microstructure and mechanical properties of plasma welded UNS S32760 super-duplex stainless steels. *Journal of Materials Science, 44*(23), 6372-6383.

Mordike, B., & Ebert, T. (2001). Magnesium: properties—applications—potential. *Materials Science and Engineering: A, 302*(1), 37-45.

Naeem, M. (1999). Welding of aluminum alloys with continuous wave Nd: YAG laser up to 5kW. *Proc. of ICALEO 1999*, 15-18.

Nasiri, A., Li, L., Kim, S., Zhou, Y., Weckman, D., & Nguyen, T. (2011). Microstructure and properties of laser brazed magnesium to coated steel. *Welding Journal, 90*(11).

Nasiri, A., Weckman, D., & Zhou, Y. (2013a). Interfacial microstructure of diode laser brazed AZ31B magnesium to steel sheet using a nickel interlayer. *Welding Journal, 92*(1), 1-10.

Nasiri, A. M. (2013). Laser Brazing of Magnesium to Steel Sheet.

Nasiri, A. M., Chartrand, P., Weckman, D. C., & Zhou, N. Y. (2013b). Thermochemical analysis of phases formed at the interface of a Mg alloy-Ni-plated steel joint during laser brazing. *Metallurgical and Materials Transactions A, 44*(4), 1937-1946.

Otto, A., & Schmidt, M. (2010). Towards a universal numerical simulation model for laser material processing. *Physics Procedia, 5*, 35-46.

Polmear, I. (1995). Light alloys-Metallurgy of the light metals, Edward Arnold. In: London.

Quintino, L., Costa, A., Miranda, R., Yapp, D., Kumar, V., & Kong, C. (2007). Welding with high power fiber lasers–a preliminary study. *Materials & Design, 28*(4), 1231-1237.

Raghavan, V. (2009). Al-Mg-Ni (Aluminum-Magnesium-Nickel). *Journal of Phase Equilibria and Diffusion, 30*(3), 274-275.

Ren, D., Zhao, K., Pan, M., Chang, Y., Gang, S., & Zhao, D. (2017). Ultrasonic spot welding of magnesium alloy to titanium alloy. *Scripta Materialia, 126*, 58-62.

Sakkinen, D. (1995). Magnesium alloy metallurgy. *Advanced Materials & Processes, 5*, 26-27.

Schubert, E., Klassen, M., Zerner, I., Walz, C., & Sepold, G. (2001). Light-weight structures produced by laser beam joining for future applications in automobile and aerospace industry. *Journal of Materials Processing Technology, 115*(1), 2-8.

Schutz, R., & Watkins, H. (1998). Recent developments in titanium alloy application in the energy industry. *Materials Science and Engineering: A, 243*(1-2), 305-315.

Song, J., Lin, S., Yang, C., & Fan, C. (2009). Effects of Si additions on intermetallic compound layer of aluminum–steel TIG welding–brazing joint. *Journal of Alloys and Compounds, 488*(1), 217-222.

Squillace, A., Prisco, U., Ciliberto, S., & Astarita, A. (2012). Effect of welding parameters on morphology and mechanical properties of Ti–6Al–4V laser beam welded butt joints. *Journal of Materials Processing Technology, 212*(2), 427-436.

Standard, A. (2001). E3, Standard guide for preparation of metallographic specimens. *West Conshohecken, PA: ASTM International*.

Sun, Z., & Karppi, R. (1996). The application of electron beam welding for the joining of dissimilar metals: an overview. *Journal of Materials Processing Technology, 59*(3), 257-267.

Takemoto, T., Kimura, S., Kawahito, Y., Nishikawa, H., & Katayama, S. (2009). Fluxless joining of aluminium alloy to steel by laser irradiation method. *Welding International, 23*(5), 316-322.

Tan, C., Chen, B., Meng, S., Zhang, K., Song, X., Zhou, L*., et al.* (2016a). Microstructure and mechanical properties of laser welded-brazed Mg/Ti joints with AZ91 Mg based filler. *Materials & Design, 99*, 127-134.

Tan, C., Chen, Y., Li, L., & Guo, W. (2013). Comparative study of microstructure and mechanical properties of laser welded–brazed Mg/steel joints with four different coating surfaces. *Science and Technology of Welding and Joining, 18*(6), 466-472.

Tan, C., He, W., Gong, X., Li, L., & Feng, J. (2015). Influence of laser power on microstructure and mechanical properties of fiber laser-tungsten inert gas hybrid welded Mg/Cu dissimilar joints. *Materials & Design, 78*, 51-62.

Tan, C., Li, L., Chen, Y., Nasiri, A., & Zhou, Y. (2014). Microstructural characteristics and mechanical properties of fiber laser welded-brazed Mg alloy-stainless steel joint. *Welding Journal, 93*(10), 399-409.

Tan, C., Song, X., Chen, B., Li, L., & Feng, J. (2016b). Enhanced interfacial reaction and mechanical properties of laser welded-brazed Mg/Ti joints with Al element from filler. *Materials Letters, 167*, 38-42.

Tan, C., Song, X., Meng, S., Chen, B., Li, L., & Feng, J. (2016c). Laser welding-brazing of Mg to stainless steel: joining characteristics, interfacial microstructure, and mechanical properties. *The International Journal of Advanced Manufacturing Technology, 86*(1-4), 203-213.

Tan, C., Xiao, L., Liu, F., Chen, B., Song, X., Li, L*., et al.* (2017a). Influence of Laser Power on the Microstructure and Mechanical Properties of a Laser Welded-Brazed Mg Alloy/Ni-Coated Steel Dissimilar Joint. *Journal of Materials Engineering and Performance*, 1-15.

Tan, C., Yang, J., Zhao, X., Zhang, K., Song, X., Chen, B*., et al.* (2018a). Influence of Ni coating on interfacial reactions and mechanical properties in laser welding-brazing of Mg/Ti butt joint. *Journal of Alloys and Compounds, 764*, 186-201.

Tan, C., Zang, C., Zhao, X., Xia, H., Lu, Q., Song, X*., et al.* (2018b). Influence of Ni-coating thickness on laser lap welding-brazing of Mg/Ti. *Optics & Laser Technology, 108*, 378-391.

Tan, C. W., Lu, Q. S., Chen, B., Song, X. G., Li, L. Q., Feng, J. C*., et al.* (2017b). Influence of laser power on microstructure and mechanical properties of laser welded-brazed Mg to Ni coated Ti alloys. *Optics and Laser Technology, 89*, 156-167.

Tanabe, H., & Watanabe, T. (2008). Friction stir welding between CPTi and AZ31B magnesium alloy: effect of rotating tools on the welding strength of the joint. *Welding International, 22*(9), 588-596.

Tanigawa, Y., Akai, T., Kawamura, R., & Oka, N. (1996). Transient heat conduction and thermal stress problems of a nonhomogeneous plate with temperature-dependent material properties. *Journal of Thermal Stresses, 19*(1), 77-102.

Tsirkas, S., Papanikos, P., & Kermanidis, T. (2003). Numerical simulation of the laser welding process in butt-joint specimens. *Journal of Materials Processing Technology, 134*(1), 59-69.

Villars, P., Prince, A., & Okamoto, H. (1995). *Handbook of ternary alloy phase diagrams*: Asm Intl.

Wang, X. Y., Sun, D. Q., & Sun, Y. (2016). Influence of Cu-Interlayer Thickness on Microstructures and Mechanical Properties of MIG-Welded Mg-Steel Joints. *Journal of Materials Engineering and Performance, 25*(3), 910-920.

Watanabe, T., Takayama, H., Yanagisawa, A., & Konuma, S. (2005). Observation of the Solid State Welded Interface between Steel and Aluminum Alloy Using a Rotating Pin-Solid State Welding of Dissimilar Metals Using a Rotating Pin(Report 2). *QUARTERLY JOURNAL OF THE JAPAN WELDING SOCIETY, 23*(4), 603-607.

Weisheit, A., Galun, R., & Mordike, B. L. (1998). CO2 laser beam welding of magnesium-based alloys. *Welding Journal, 77*(4), 149s-154s.

Williams, J. C., & Belov, A. (1982). Titanium and titanium alloys: Scientific and technological aspects. *New York, Plenum Press, 1982., 1*.

Witusiewicz, V. T., Bondar, A. A., Hecht, U., Rex, S., & Velikanova, T. Y. (2008). The Al–B–Nb–Ti system: III. Thermodynamic re-evaluation of the constituent binary system Al–Ti. *Journal of Alloys and Compounds, 465*(1), 64-77.

Xu, C., Sheng, G., Deng, Y., Yuan, X., & Tang, K. (2014a). Microstructure and mechanical properties of tungsten inert gas welded–brazed Mg/Ti lap joints. *Science and Technology of Welding and Joining, 19*(5), 443-450.

Xu, C., Sheng, G., Sun, Y., Yuan, X., & Jiao, Y. (2017). Microstructure and mechanical properties of high-energy shot-peened Mg/Ti weldments. *Science and Technology of Welding and Joining*, 1-7.

Xu, C., Sheng, G., Wang, H., & Yuan, X. (2014b). Reinforcement of Mg/Ti joints using ultrasonic assisted tungsten inert gas welding–brazing technology. *Science and Technology of Welding and Joining, 19*(8), 703-707.

Xu, C., Sheng, G. M., Wang, H., Feng, K., & Yuan, X. J. (2016). Tungsten Inert Gas Welding-Brazing of AZ31B Magnesium Alloy to TC4 Titanium Alloy. *Journal of Materials Science & Technology, 32*(2), 167-171.

Yamamoto, A., Terashita, M., & Tsubakino, H. (2007). Textures in AMCa602 and AZ31B magnesium alloys formed by wavy bend pressing. *Keikinzoku/Journal of Japan Institute of Light Metals, 57*(3), 99-104.

Yang, J., Sun, S., Brandt, M., & Yan, W. (2010). Experimental investigation and 3D finite element prediction of the heat affected zone during laser assisted machining of Ti6Al4V alloy. *Journal of Materials Processing Technology, 210*(15), 2215-2222.

Yang, L., & Xiao, Z. (1995). Elastic-plastic modelling of the residual stress caused by welding. *Journal of Materials Processing Technology, 48*(1-4), 589-601.

Yue, T., Li, T., & Lin, X. (2010). Microstructure and phase evolution in laser cladding of Ni/Cu/Al multilayer on magnesium substrates. *Metallurgical and Materials Transactions A, 41*(1), 212.

Zang, C., Liu, J., Tan, C., Zhang, K., Song, X., Chen, B., *et al.* (2018). Laser conduction welding characteristics of dissimilar metals Mg/Ti with Al interlayer. *Journal of Manufacturing Processes, 32*, 595-605.

Zhang, K., Liu, J., Tan, C., Wang, G., Song, X., Chen, B., *et al.* (2018a). Dissimilar joining of AZ31B Mg alloy to Ni-coated Ti-6Al-4V by laser heat-conduction welding process. *Journal of Manufacturing Processes, 34, Part A*, 148-157.

Zhang, L., Gao, X., Sun, M., & Zhang, J. (2014). Weld outline comparison between various pulsed Nd: YAG laser welding and pulsed Nd: YAG laser–TIG arc welding. *The International Journal of Advanced Manufacturing Technology, 75*(1-4), 153-160.

Zhang, Z.-M., & Xu, H.-Y. (2008). Corrosion and mechanical properties of hot-extruded AZ31 magnesium alloys. *Transactions of Nonferrous Metals Society of China, 18*, s140-s144.

Zhang, Z., Tan, C., Wang, G., Chen, B., Song, X., Zhao, H., *et al.* (2018b). Laser Welding-Brazing of Immiscible AZ31B Mg and Ti-6Al-4V Alloys Using an Electrodeposited Cu Interlayer. *Journal of Materials Engineering and Performance*, 1-13.

Zhang, Z., Tan, C., Zhao, X., Chen, B., Song, X., & Zhao, H. (2018c). Influence of Cu coating thickness on interfacial reactions in laser welding-brazing of Mg to Ti. *Journal of Materials Processing Technology, 261*, 61-73.

Zhao, D., Zhao, K., Ren, D., & Guo, X. (2017). Ultrasonic Welding of Magnesium–Titanium Dissimilar Metals: A Study on Influences of Welding Parameters on Mechanical Property by Experimentation and Artificial Neural Network. *Journal of Manufacturing Science and Engineering, 139*(3), 031019.

Zhecheva, A., Sha, W., Malinov, S., & Long, A. (2005). Enhancing the microstructure and properties of titanium alloys through nitriding and other surface engineering methods. *Surface and Coatings technology, 200*(7), 2192-2207.

Ziegelheim, J., Hiraki, S., & Ohsawa, H. (2007). Diffusion bondability of similar/dissimilar light metal sheets. *Journal of Materials Processing Technology, 186*(1-3), 87-93.

LIST OF PUBLICATIONS AND PAPERS PRESENTED

Auwal, S. T., Ramesh, S., Yusof, F., & Manladan, S. M. (2018). **A review on laser beam welding of copper alloys**. *The International Journal of Advanced Manufacturing Technology, 96*(1-4), 475-490.

Auwal, S. T., Ramesh, S., Yusof, F., & Manladan, S. M. (2018). **A review on laser welding of titanium alloys**. *The International Journal of Advanced Manufacturing Technology, 97*(1), 1071-1098.

Auwal, S. T., Ramesh, S., Yusof, F., Zhang, Z., Zhao, X.Y., & Manladan, S. M. (2018). **Comperative study on characteristies of laser welded-brazed AZ31/Ti-6Al-4V lap joints with and without coatings**. *The International Journal of Advanced Manufacturing Technology,* doi: 10.1007/s00170-018-2903-z.

Auwal, S. T., Ramesh, S., Zhang, Z., Liu, J., Tan, C.W., Manladan, S. M., Yusof, F., & Tarlochan, F. (2018). **Influence of electrodepsoted Cu-Ni layer on interfacial reaction and mechanical properties of laser welded-brazed Mg/Ti lap joints**. *Journal of Manufacturing Processes, 37* (2019), 251-265.

Auwal, S. T., Ramesh, S., Zhang, Z., Yusof, F., Tan, C.W., Liu, J., Manladan, S. M. & Tarlochan, F. (2018). **Effect of copper-nickel interlayer thickness on laser welding-brazing of Mg/Ti alloy**. *Optics & Laser Technology, (Under-review).*